ANISOTROPY EFFECTS DURING UNSTABLE STEP FLOW GROWTH

Dissertation

zur Erlangung des akademischen Grades

doctor rerum naturalium
(Dr. rer. nat.),

genehmigt durch die
Fakultät für Naturwissenschaften
der Otto-von-Guericke-Universität Magdeburg

von Dipl.-Phys. Gerrit Danker
geb. am 23. Oktober 1975 in Magdeburg

Gutachter:	Prof. Dr. Klaus Kassner Dr. Chaouqi Misbah Privatdozent Dr. Axel Voigt
Eingereicht am:	29. Juni 2005
Verteidigung am:	10. November 2005

Acknowledgements

First of all I would like to thank my supervisor Klaus Kassner for his overall support during the various stages of my Ph.D. studies. I am grateful for the pleasant working environment and many important learning opportunities.

This work is the result of a fruitful collaboration with Laboratoire de Spectrométrie Physique in Grenoble, where I spent numerous enjoyable research visits. I am indebted to Chaouqi Misbah for this opportunity and I would like to thank him for his great hospitality and many inspiring discussions.

I am very grateful to Olivier Pierre-Louis for patiently explaining theoretical techniques and for many important discussions that helped to shape my understanding of step flow growth. I would also like to thank him for valuable comments on the manuscript of this thesis and for his great hospitality.

I would like to thank Heike Emmerich for introducing me to the interesting field of crystal steps and for guiding me at the beginning of my Ph.D. work.

My thanks go to Dorothea Erndt for invaluable help with administrative tasks and to countless former and current members of the physics department, especially Evgueni Zemskov, Peter Kohlert, and Thomas Fischaleck. I learnt quite a bit from them.

I am grateful to Walfred Grambow from Interdisziplinäres Zentrum für paralleles Rechnen for managing a reliable and powerful computing environment which was indispensable for carrying out the numerical part of this work.

Finally, and most importantly, I would like to thank my family for their unending support and love.

I gratefully acknowledge financial help from the Deutsche Forschungsgemeinschaft and from the French-German cooperation programme PROCOPE.

Contents

1. Introduction

1.1. Challenges of modern crystal growth

The manufacture of crystalline materials is an ancient craft. But only in the past decades has it been possible to gain a deeper understanding of crystal growth processes and the relationship between the microscopic structure of materials and their macroscopic properties. Today, at a time when we are faced with an ever growing need for new materials with any desired characteristic, the science of crystallization is an active field of research, both in experiments and in theory.

With the advent of microelectronics and the challenge to create smaller circuits and gadgets with novel electronic and optical properties, it has become necessary to control the structure and chemical composition of crystals even on the atomic scale. Modern crystal growth techniques like molecular beam epitaxy (MBE) or organometallic vapour phase epitaxy (OMVPE) allow to fine-tune the deposition flux so that even fractions of a monolayer can be deposited onto a crystal sample. Thus it becomes possible to construct complex epitaxial architectures. MBE, for example, has been successfully applied to create nanostructures, such as quantum wires and quantum dots [57].

1.2. Molecular beam epitaxy and step flow

The basic principle of MBE is easy to grasp. A sample is placed inside a vacuum chamber, where it is subjected to a beam of particles (molecules or atoms). This beam can be produced by thermal heating of a bulk material, which may or may not have the same chemical composition as the sample. If the bulk has the same chemical composition, one speaks of *homoepitaxy*, otherwise of *heteroepitaxy*.

The samples used in MBE are usually single crystals with high-quality surfaces and well-defined crystallographic orientation. Often these surfaces are *vicinal surfaces*, which are obtained by cutting a crystal under a small angle θ with respect to a high-symmetry plane. The resulting surface geometry on the atomic scale is a sequence of terraces, which are separated by steps of monoatomic height (see Fig. 1.1).

Step flow is one of the growth modes in MBE. It allows for a controlled layer-by-layer growth. The growth conditions are adjusted such that the atoms which land on the surface do not nucleate on the terraces (to produce islands), but rather

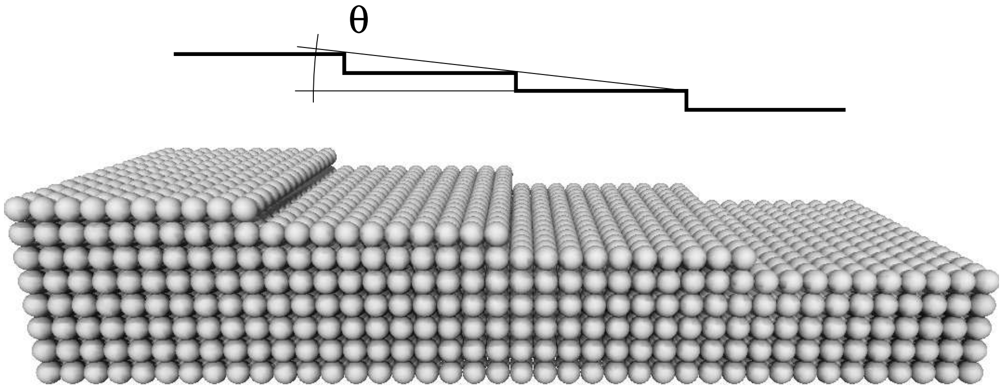

Figure 1.1.: Schematic of a crystal with an ideal vicinal surface. The surface geometry, consisting of wide terraces and monoatomic steps, results from a small miscut (at angle θ) with respect to a high-symmetry crystal plane.

diffuse until they attach to a step. The crystal thus grows thanks to the movement of the steps.

In an ideal situation, all terraces collect the same amount of matter and each point of the steps moves at the same velocity so that the geometry of the surface does not change. In practice, however, there are a number of factors that interfere with this scenario. The surface suffers morphological instabilities, which are expressed through a roughening of the surface. This roughening, which depends on certain growth parameters like temperature or the intensity of the deposition flux, can be observed *in situ* with the help of RHEED spectroscopy or even with the help of advanced imaging techniques like STM. Several types of morphological instabilities can be distinguished. They are briefly presented in the next section.

1.3. Morphological instabilities

The roughening of the surface that is observed in MBE during growth can occur due to a variety of physical mechanisms and the precise ingredients are often not well understood. In the past decades, many models have been suggested with the aim of describing surface roughening in MBE [4].

One source of roughening can be sought in stochastic processes. Even if a vicinal surface is left to itself, at finite temperature, the steps will roughen due to thermodynamic fluctuations. A crystal step is a one-dimensional object, which can be deformed at minimal energy cost. In fact, $T_{\mathrm{R}} = 0$ is the roughening temperature of an isolated step [3].

During growth, there are additional stochastic influences. The atomic beam is not fully homogeneous (*shot noise*), which leads to an unequal distribution of matter on the terraces. There is also noise in the diffusion process. These effects can contribute to the roughening of the surface [4].

Another source of roughening is found in deterministic growth instabilities. They are linked to inherent nonlinearities and only need an initial perturbation of ideal step flow in order to develop. Step flow may suffer three basic deterministic instabilities: meandering, bunching, and island formation.

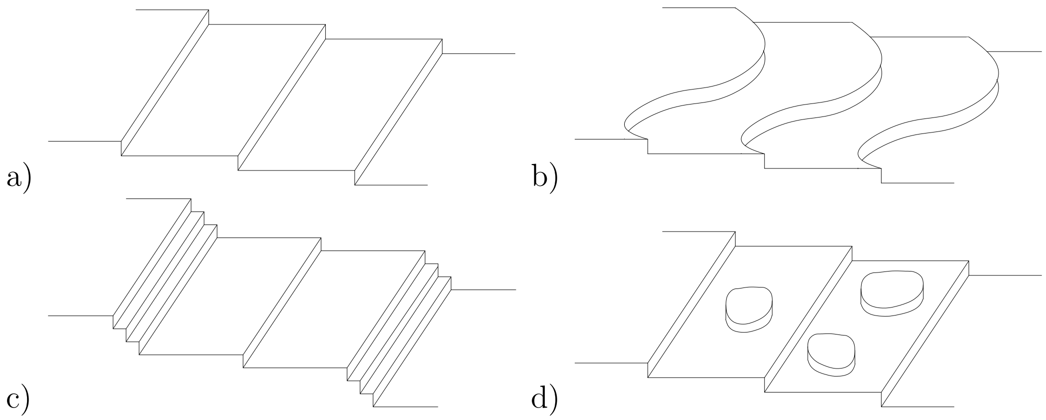

Figure 1.2.: Three morphological instabilities that can occur during step flow growth. A perfect vicinal surface (a) may be unstable with respect to step meandering (b), step bunching (c), and island formation (d).

In *step meandering* [Fig. 1.2 b)], initially straight steps develop a large meander. One of the physical reasons for this instability is an energy barrier, the so-called Ehrlich-Schwoebel barrier, at the step edges, which can prevent adatoms from descending the steps. In the presence of an Ehrlich-Schwoebel barrier, the protruding parts of the steps receive more amount of matter per unit length than the receding parts: The amplitude of the step meander grows in time. The meandering instability leads to the formation of ripples in the direction of the step train.

In *step bunching* [Fig. 1.2 c)], initially equidistant steps form step bunches (or macrosteps), which are separated by terraces that are much wider than the original interstep distance ℓ. This instability leads to the emergence of ripples perpendicular to the step train direction. Step bunching is often observed when a DC heating current is applied to the sample.

Island formation [Fig. 1.2 d)] occurs if the typical distance between nucleation centres is smaller than the interstep distance: Adatoms meet on the terraces before they attach to a step, forming a dimer and thus a seed for a new layer on top of the terrace. If nucleation also occurs on top of newly formed islands, mound formation sets in and a rapid transition to three-dimensional growth takes place.

It is a great goal of theoretical crystal physics to understand the precise mechanisms that lead to a roughening of the surface, so that one can either avoid them or use their features to grow surfaces with a desired surface pattern. An idea of such an application is illustrated in Fig. 1.3: The meandering steps give rise to a ripple structure, whose troughs might be a preferred place for the creation of pyramidal structures of foreign atoms.

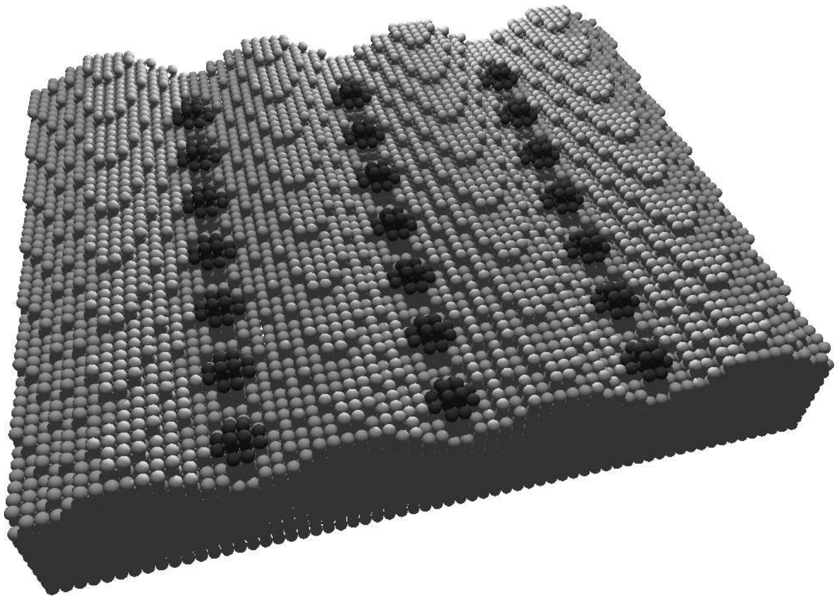

Figure 1.3.: Schematic of a vicinal surface with a meandering pattern. A ripple structure is formed, which may stimulate the ordered growth of foreign atoms into pyramidal structures (dark spheres).

This dissertation contributes to the understanding of the meandering instability. With the help of a continuum model of step flow growth, we study the effects of crystalline anisotropy on the meandering dynamics.

It is shown that under certain conditions the lateral size of the meandering ripples is the outcome of a compromise between the diffusive instability and surface anisotropy, which tends to pin the crystal steps along preferred orientations. The resulting scenario is called *interrupted coarsening*: The wavelength of the meander, which is first close to the wavelength favoured by the instability, increases up to a critical wavelength, whose magnitude depends on surface anisotropy. At this point the coarsening process is interrupted.

We show that the scenario of interrupted coarsening originates from the anisotropies of various surface properties and provide formulas to calculate the expected wavelength.

2. Fundamental concepts

In this chapter we provide the physical and mathematical background that we need for our study of anisotropic meandering steps. We first explain the Ehrlich-Schwoebel effect, which is the physical reason for the meandering instability. Then we provide a brief introduction to the Burton-Cabrera-Frank (BCF) theory, a well-established continuum theory of step flow growth.

2.1. Ehrlich-Schwoebel effect

A single adatom may diffuse freely on a vicinal surface until it reaches a step.[1] There it has a finite probability to actually cross the step. This is referred to as *step transparency* [41]. But we want to consider cases where it is more likely that the adatom is "reflected" or becomes incorporated into the step.

Usually an adatom has a smaller probability to get incorporated if it approaches the step from the upper terrace. This is due to the so-called *Ehrlich-Schwoebel effect*, which can be explained by an energy barrier at the step edge (see Fig. 2.1): If an adatom that comes from the upper terrace is to be incorporated into a step, additional energy is required to break bonds. Two basic mechanisms are conceivable. The adatom can either hop across the step edge, whereby it breaks some next-nearest-neighbour bonds, or it can fill the gap that is created by a step atom that moves one lattice site towards the terrace in front of the step.

An adatom on the lower terrace need not cross an additional energy barrier before it can be incorporated into the step, which explains the higher probability of this process.

It should be mentioned that the precise attachment mechanisms can be far more complex. In particular, the attachment probabilities depend on the local kink configuration, which is a function of the step orientation and the curvature. Thus, attachment kinetics are often highly anisotropic. There are even materials, in which the Ehrlich-Schwoebel barrier is inverted for some step orientations. In Chapter 4 we shall analyse the effects of anisotropic attachment on the step dynamics.

---

[1] We assume that there is no desorption of adatoms into the vacuum and that the probability of nucleation on the terraces is negligible.

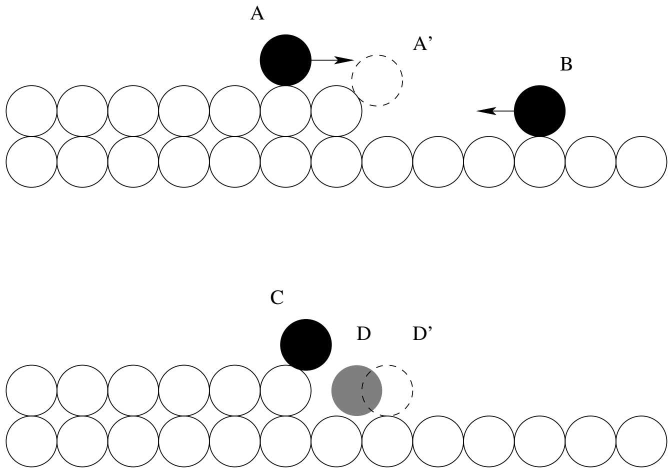

Figure 2.1.: The Ehrlich-Schwoebel effect. Atom A attaches to the step with a lower probability than atom B, because atom A has to pass through poorly coordinated site A’. Attachment from above can also take place by an exchange mechanism: Step atom D moves to position D’ so that atom C can be incorporated into the top layer. This process also has a smaller probability than the attachment of atom B.

2.2. Burton-Cabrera-Frank model

A vicinal surface is characterized by a sequence of terraces, which are separated by monoatomic steps (see Fig. 2.2). In step flow growth, the crystal grows due to the movement of these steps. This process is conveniently described within the BCF theory [8], which has recently been extended to include additional effects like attachment asymmetry [3], line diffusion along the step edge [20, 25], and elastic step-step interactions [39].

The fundamental objects of the BCF theory are terraces, steps, and adatoms. Steps are represented by continuous lines. Adatoms are atoms that are adsorbed on the terraces and are free to diffuse until they attach to a step. Instead of tracking individual adatoms, the BCF theory describes their motion using a diffusion field $c(\mathbf{r}, t)$, which is continuous on the terraces and usually discontinuous at the steps.[2] The vector $\mathbf{r} = (x, y)$ specifies a point on the surface.

During growth, and this is the situation of interest in the present context, atoms arrive on the surface with a given rate F and diffuse on the terraces [diffusion current $\mathbf{j}(\mathbf{r}, t)$], until they reach a step [attachment currents $j_{\pm}(s)$, where s is the arc length along the step]. Once these atoms are incorporated into the step, they

---

[2] In the original BCF theory, where steps are assumed to act as perfect sinks for diffusing adatoms, the diffusion field is continuous at the steps. The discontinuity is due to the attachment asymmetry at the steps, which results from the Ehrlich-Schwoebel barrier.

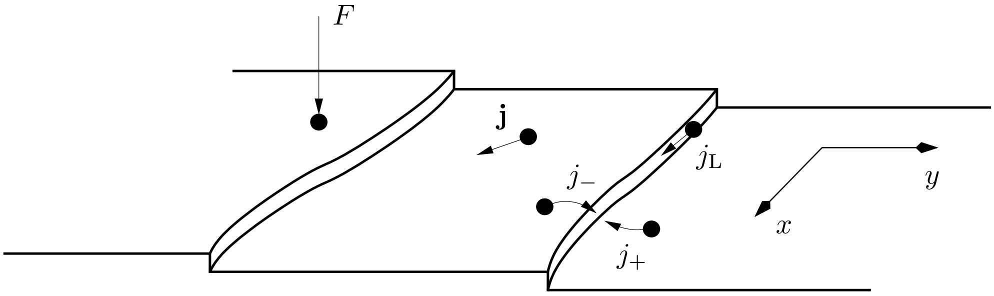

Figure 2.2.: Sketch of a vicinal surface. The fundamental processes that occur during growth are shown: attachment to the surface (F), diffusion on the terraces ($\mathbf{j}$), attachment to the steps from the lower terrace (j_+) as well as from the upper terrace (j_-), and diffusion along the step (j_{L}).

can still move along the step [relaxational current $j_{\mathrm{L}}(s)$], following a gradient of the step chemical potential μ.

Now that we have presented the basic ingredients of the model, we are ready to give the equations that govern the dynamics of the diffusion field and the motion of the steps.

On the terraces, the concentration of adatoms obeys the diffusion equation

$$\partial_t c = F - \nabla \cdot \mathbf{j}, \tag{2.1}$$

where the current $\mathbf{j}(\mathbf{r}, t)$ is driven by the concentration gradient according to Fick's law:

$$\mathbf{j} = -D\,\nabla c. \tag{2.2}$$

D is the diffusion constant. It is a scalar if terrace diffusion is isotropic, otherwise it is a matrix of the form

$$D = \begin{pmatrix} D_{11} & D_{12} \\ D_{12} & D_{22} \end{pmatrix}. \tag{2.3}$$

It is common practice [3, 5] to take the quasistatic limit of the diffusion equation (2.1) by setting the left-hand side zero, since the relaxation of the diffusion field is usually much faster than the motion of the steps. Moreover, we have assumed vanishing desorption (detachment of adatoms from the terraces into the vacuum), which is often the case in step flow growth [20]. Also, we have not included stochastic contributions, since we are interested in an instability that is deterministic in origin and only needs an initial perturbation of ideal step flow in order to develop.

At equilibrium there is a certain concentration c_{eq} of adatoms directly in front of a step. It is related to the equilibrium concentration c^0_{eq} for a straight step and to the local chemical potential μ via

$$c_{\mathrm{eq}} = c^0_{\mathrm{eq}}\, e^{\mu/k_{\mathrm{B}}T}, \tag{2.4}$$

where k_{B} is the Boltzmann constant and T the temperature. For small departure from equilibrium, this equation can be linearized:

$$c_{\mathrm{eq}} = c^0_{\mathrm{eq}}\, (1 + \mu/k_{\mathrm{B}}T). \tag{2.5}$$

The step chemical potential is given by

$$\mu = \left(\frac{\delta N}{\delta \zeta}\right)^{-1} \frac{\delta \mathcal{F}}{\delta \zeta}. \tag{2.6}$$

$\mathcal{F}[\{\zeta_m\}]$ is the step free energy, which, in the general case, is a functional of the configuration of all steps, and N is the number of particles that are incorporated into the step (as compared to an arbitrary reference state).

Without elastic interactions between the steps, the chemical potential is only determined by curvature effects, as described by the Gibbs-Thomson relation:

$$\mu = \Omega \tilde{\gamma} \kappa. \tag{2.7}$$

Here $\tilde{\gamma}(\theta)$ is the step stiffness, which is related to the free energy density $\gamma(\theta)$ of the step via $\tilde{\gamma}(\theta) = \gamma(\theta) + \gamma''(\theta)$. Both quantities depend on the local orientation of the step (angle θ between the step normal and a fixed direction). Ω is the atomic area and κ the local curvature of the step.

It is useful to introduce $\Gamma(\theta) = \Omega\tilde{\gamma}(\theta)/k_{\mathrm{B}}T$, so that the equilibrium concentration can be written in a compact form:

$$c_{\mathrm{eq}} = c^0_{\mathrm{eq}}[1 + \Gamma(\theta)\, \kappa]. \tag{2.8}$$

At thermodynamic equilibrium, there is no net attachment to the steps. The attachment currents $j_\pm$ are thus related to the local departure from equilibrium. Following previous studies [3, 20], we assume a linear relationship with kinetic coefficients $\nu_\pm(\theta)$:

$$j_+ = \nu_+(\theta)\, [c - c_{\mathrm{eq}}]|_+, \tag{2.9}$$

$$j_- = \nu_-(\theta)\, [c - c_{\mathrm{eq}}]|_-. \tag{2.10}$$

As indicated in Fig. 2.2, the “+” refers to the ascending side of the step and the “−” to the descending side of the step.

Furthermore, the attachment currents can be evaluated from the local concentration gradient perpendicular to the steps. With the step normal **n** (pointing to the lower terrace) the attachment currents can be written as

$$j_+ = \mathbf{n} \cdot D\,\nabla c|_+, \tag{2.11}$$

$$j_- = -\mathbf{n} \cdot D\,\nabla c|_-. \tag{2.12}$$

Equating the relations (2.9, 2.10) with (2.11, 2.12), we obtain the desired boundary conditions for the diffusion equation:

$$\mathbf{n} \cdot D\,\nabla c|_+ = \nu_+(\theta)\,[c - c_{\mathrm{eq}}]|_+, \tag{2.13}$$

$$-\mathbf{n} \cdot D\,\nabla c|_- = \nu_-(\theta)\,[c - c_{\mathrm{eq}}]|_-. \tag{2.14}$$

If there is an Ehrlich-Schwoebel effect, attachment to the step from the upper terrace is slower and we have $\nu_- < \nu_+$.

The evolution of the step curve is determined by the normal velocity v_n, which is obtained from mass conservation at the step:

$$v_n = \Omega\,(j_+ + j_-) + a\,\partial_s j_{\mathrm{L}}, \tag{2.15}$$

where a is the lattice constant. This equation contains the attachment currents j_+ and j_- and the divergence of a relaxational current j_{L} along the step. The current j_{L} is driven by differences of the chemical potential:

$$j_{\mathrm{L}} = D_{\mathrm{L}}(\theta)\,\partial_s\left(\frac{\mu}{k_B T}\right) = D_{\mathrm{L}}(\theta)\,\partial_s[\Gamma(\theta)\,\kappa], \tag{2.16}$$

where $D_{\mathrm{L}}(\theta)$ is the anisotropic line diffusion coefficient [20].

At this point the mathematical formulation of the model is complete. We can now use these equations to study the meandering dynamics of crystal steps during growth. In the next chapter we shall first perform a linear stability analysis of straight steps with respect to meandering and then derive an evolution equation for the step meander by means of a multiscale expansion.

3. Evolution equation

In this chapter we shall use asymptotic expansion techniques to derive an evolution equation for the step meander. Following previous works on this topic [20, 45], we shall first review the linear stability problem, then identify the scaling of characteristic quantities with the deposition flux, and finally perform an asymptotic expansion of the model equations in the small-flux (long-wave) limit to derive an evolution equation. At the end of this chapter we shall make an explicit comparison with a numerical integration of the full BCF equations.

3.1. Linear stability analysis

An ideal vicinal surface is characterized by straight steps and a constant interstep distance ℓ. In ideal step flow, all steps receive the same amount of matter, and from mass conservation it follows that all steps move at the same velocity $V_0 = \Omega F \ell$. Except for the translation of the steps, the surface geometry does not change in time.

It is a well-known fact, however, that for a positive Ehrlich-Schwoebel effect ($\nu_+ > \nu_-$), the surface is subject to the meandering instability [3]: A small perturbation of the steps is amplified so that the steps do not remain straight but instead display a large meander. In order to assess the stability of the moving steps with respect to meandering, we perturb the steps with *small* sinusoidal modulations and determine from the BCF equations whether the amplitude of these modulations grows or decays in time. As these perturbations are to be small, we can linearize the problem and treat every mode separately.

Let the meander of the mth step around its average position be $\zeta_m(x,t)$. We can now perform a Fourier transformation of the whole surface with respect to step number (m), space (x), and time (t):

$$\hat{\zeta}(\phi, q, \omega) = \sum_{m=-\infty}^{\infty} \int_{-\infty}^{\infty} \int_{-\infty}^{\infty} \zeta_m(x,t)\, \mathrm{e}^{-i(\phi m + qx + \omega t)}\, \mathrm{d}x\, \mathrm{d}t. \tag{3.1}$$

Here ϕ is the phase shift between neighbouring steps, q the wave number of the step modulation and $i\omega$ the complex growth rate of the perturbation.

As the various Fourier modes decouple in the linearized problem, we can plug a single mode,

$$\zeta_m(x,t) = \varepsilon\, \mathrm{e}^{i(\phi m + qx + \omega t)}, \tag{3.2}$$

into the model equations and linearize in ε. For simplicity we shall first assume isotropic terrace diffusion (i. e. D is scalar) and a strong attachment asymmetry: Adatoms do not descend the steps due to an infinite Ehrlich-Schwoebel effect ($\nu_- = 0$), whereas the steps act as perfect sinks for adatoms that come from the lower terrace ($\nu_+ \to \infty$). We then obtain from the condition that mass be conserved at the steps, a relationship $i\omega = i\omega(q, \phi)$, the so-called dispersion relation, whose complex components are given by

$$\begin{aligned}\mathrm{Re}(i\omega) &= \frac{\Omega F}{\cosh q\ell}\left[q\ell \sinh q\ell - \cosh q\ell + \cos\phi\right] \\ &\quad - \frac{\Gamma(0)\, q^2}{\cosh q\ell}\left[q D_{\mathrm{S}} \sinh q\ell + q^2 a D_{\mathrm{L}}(0) \cosh q\ell\right], \qquad (3.3)\\ \mathrm{Im}(i\omega) &= \frac{\Omega F}{\cosh q\ell} \sin\phi. \qquad (3.4)\end{aligned}$$

Here we have introduced the macroscopic terrace diffusion constant $D_{\mathrm{S}} = c_{\mathrm{eq}}^0 \Omega D$ [20].

The real part $\mathrm{Re}(i\omega)$ is the growth rate, whose sign determines whether the perturbation grows (+) or decays (−) in time. The imaginary part $\mathrm{Im}(i\omega)$ describes propagative effects [20].

From the real part $\mathrm{Re}(i\omega)$ we readily conclude that the most unstable mode is the in-phase mode ($\phi = 0$). As it is known that the synchronization of the steps happens at an early stage of the instability [20], we shall from now on concentrate on in-phase meandering, where all steps display the same meander $\zeta(x, t)$.

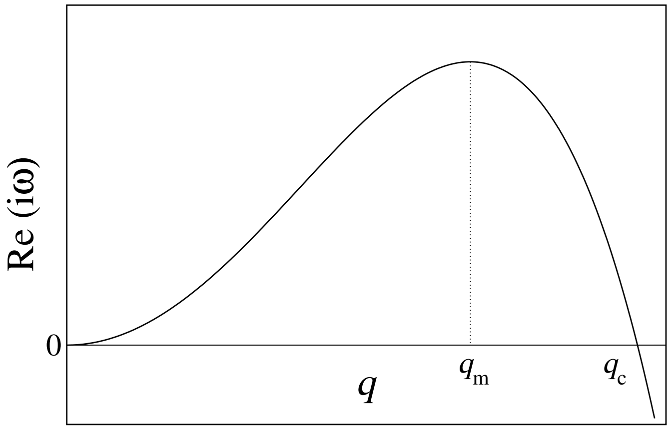

Figure 3.1.: The dispersion relation of the meandering instability. The wave number q_m of the most unstable mode and the critical wave number q_c are shown. A positive $\mathrm{Re}(i\omega)$ signals that the corresponding mode is linearly unstable, a negative $\mathrm{Re}(i\omega)$ that it is linearly stable.

Expanding Eq. (3.3) in powers of $q\ell$, we obtain for $\phi = 0$:

$$\mathrm{Re}(i\omega) = \frac{\Omega F \ell^2}{2} q^2 - \left[D_\mathrm{S}\ell + D_\mathrm{L}(0)\, a\right] \Gamma(0)\, q^4, \tag{3.5}$$

$$\mathrm{Im}(i\omega) = 0. \tag{3.6}$$

Here we have neglected terms in Fq^4, which is permissible if the flux is sufficiently small so that the condition $F \ll (D_\mathrm{S}\ell + D_\mathrm{L}a)\, \Gamma/\Omega\ell^4$ is satisfied.

From the structure of the dispersion relation we conclude that we have a $\mathrm{II_S}$-type instability in the terminology of Cross and Hohenberg [11], where the real part of the dispersion relation has the typical shape shown in Fig. 3.1. During growth ($F > 0$), all modes with a wave number $q < q_\mathrm{c}$ are unstable and all modes with a wave number $q > q_\mathrm{c}$ are stable. For $F = 0$, we have $q_\mathrm{c} = 0$ and no unstable modes exist.

From the simplified growth rate (3.5) we can evaluate the critical wave number:

$$q_\mathrm{c} = \left(\frac{\Omega F \ell^2}{2\Gamma(0)\left[D_\mathrm{S}\ell + D_\mathrm{L}(0)\, a\right]} \right)^{1/2}. \tag{3.7}$$

The wave number of the most unstable mode is given by $q_\mathrm{m} = q_\mathrm{c}/\sqrt{2}$. One usually assumes that the fastest growing mode quickly dominates all other unstable modes so that the wavelength of the pattern is finally given by

$$\lambda_\mathrm{m} = \frac{2\pi}{q_\mathrm{m}} = 4\pi \left(\frac{\Gamma(0)\left[D_\mathrm{S}\ell + D_\mathrm{L}(0)\, a\right]}{\Omega F \ell^2} \right)^{1/2}. \tag{3.8}$$

In the following we shall concentrate on situations, where the meander wavelength λ_m is large in comparison to the interstep distance ℓ. For example, growth on a Cu(1, 1, 17) surface under typical MBE conditions gives rise to a meander wavelength of about 400 Å [20], but the interstep distance on this surface is only 21.7 Å.

In this section we presented an outline of the linear stability analysis and only gave results for the one-sided model. A detailed derivation of the dispersion relation, which also covers the two-sided model, is performed in App. A.

3.2. Multiscale analysis

The solution of the linear stability problem provided us with an expression for the wavelength of the fastest growing mode, and it turned out that this wavelength can be much larger than the interstep distance. We now use these two length scales to define a dimensionless parameter

$$\epsilon \equiv 2\,(q_\mathrm{c}\ell)^2 \sim F, \tag{3.9}$$

which under the conditions of interest is small in comparison to one. This parameter ϵ is directly proportional to the deposition flux F and thus describes the strength of the instability. The idea is to use ϵ to perform a series expansion of the model equations with the aim of a simpler analytical treatment.

To do this in a consistent way, we introduce new space and time coordinates that remain of order one. From the wavelength of the most unstable mode we conclude that the relevant length scale behaves like

$$x \sim \epsilon^{-1/2} \tag{3.10}$$

and from the real part of the dispersion relation we find that the time scale for the development of the instability behaves like

$$t \sim \epsilon^{-2} \tag{3.11}$$

with the deposition flux (Fig. 3.2). We thus introduce new space and time coordinates, $X = \epsilon^{1/2}\, x$ and $T = \epsilon^2\, t$, which are of order 1.

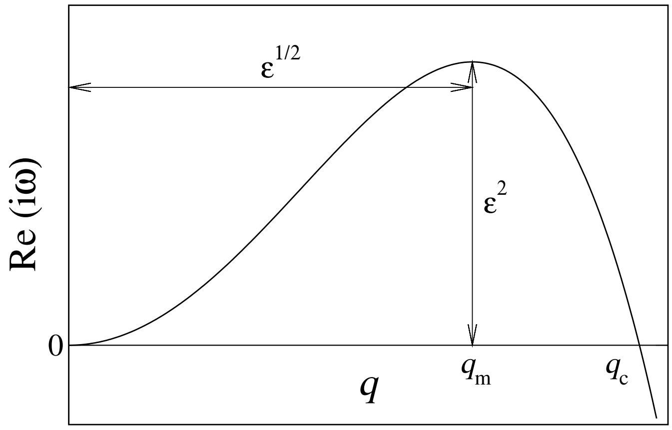

Figure 3.2.: The dispersion relation of the meandering instability. The wave number q_m of the most unstable mode is of the order $\epsilon^{1/2}$ and its growth rate is of the order ϵ^2.

In the previous section we mentioned that after a brief period of synchronization, all steps display the same meander $\zeta(x,t)$. It immediately follows that the diffusion field is the same on all terraces. The problem becomes one-dimensional.

We now seek solutions for the unknown step meander $\zeta(x,t)$ and the unknown reduced concentration field $u(x,y,t) = (c - c^0_\mathrm{eq})\,\Omega$ in the form

$$\zeta = \epsilon^{-1/2}\, H, \tag{3.12}$$

$$u = \epsilon^{1/2}\, U, \tag{3.13}$$

where the functions H and U are expanded in Taylor series in $\epsilon^{1/2}$ [20]:

$$H = H^{(0)} + \epsilon^{1/2} H^{(1/2)} + \epsilon H^{(1)} + \epsilon^{3/2} H^{(3/2)} + \dots, \tag{3.14}$$

$$U = U^{(0)} + \epsilon^{1/2} U^{(1/2)} + \epsilon U^{(1)} + \epsilon^{3/2} U^{(3/2)} + \dots. \tag{3.15}$$

The model equations can now be solved in successive orders of $\epsilon^{1/2}$, and to leading order one obtains the following highly nonlinear evolution equation for the step meander:

$$\partial_t \zeta = -\partial_x \Bigg[\frac{\Omega F \ell^2}{2} \frac{\partial_x \zeta}{1 + (\partial_x \zeta)^2} - \left(\frac{D_\mathrm{S} \ell}{1 + (\partial_x \zeta)^2} + \frac{D_\mathrm{L}(\theta)\, a}{[1 + (\partial_x \zeta)^2]^{1/2}} \right) \partial_x [\Gamma(\theta)\, \kappa] \Bigg]. \tag{3.16}$$

This equation is formally equivalent to the evolution equation for isotropic systems [20], but in our case the step stiffness Γ and the line diffusion coefficient D_L depend on the local step orientation θ.

It should be noted that the evolution equation (3.16) can be interpreted as a conservation law,

$$\partial_t \zeta + \partial_x j = 0, \tag{3.17}$$

where

$$j = \frac{\Omega F \ell^2}{2} \frac{\partial_x \zeta}{1 + (\partial_x \zeta)^2} - \left(\frac{D_\mathrm{S} \ell}{1 + (\partial_x \zeta)^2} + \frac{D_\mathrm{L} a}{[1 + (\partial_x \zeta)^2]^{1/2}} \right) \partial_x (\Gamma \kappa) \tag{3.18}$$

is a mass current along the step. Integrating Eq. (3.17) over one wavelength λ of a periodic meander, we obtain

$$\partial_t \int_{x_0}^{x_0+\lambda} \zeta(x,t)\, \mathrm{d}x + j(x_0 + \lambda, t) - j(x_0, t) = 0. \tag{3.19}$$

As j is a periodic function in x, the contributions of j vanish and we arrive at

$$\partial_t \int_{x_0}^{x_0+\lambda} \zeta(x,t)\, \mathrm{d}x = 0. \tag{3.20}$$

The total area under the step curve is conserved. This result is not surprising since the evolution equation describes the meander in a frame that moves at the average step velocity V_0. The important point here is that the step normal velocity $v_n = \partial_t \zeta / [1 + (\partial_x \zeta)^2]^{1/2}$ can be derived from the divergence of a mass current along the step. This is illustrated in Fig. 3.3.

In this section we have only provided a brief review of the derivation of the evolution equation. The full calculation can be found in App. B.

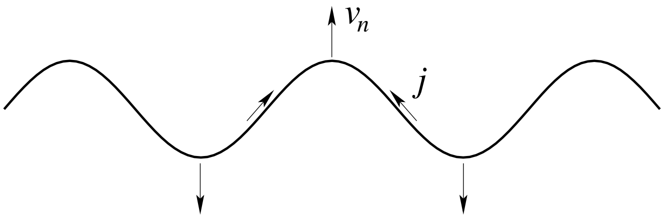

Figure 3.3.: Mass current along the step. The step normal velocity v_n can be derived from a mass current j along the step. Now the instability can be explained by a mass transport from the lower parts to the higher parts of the meander.

3.3. Numerical integration

A first idea of the meandering dynamics is gained by a numerical integration of the evolution equation (3.16). To this end we closely follow a previous work [19, 20] and express the step curve in intrinsic coordinates: The step curve is now represented by $\theta(s)$, where $\theta = \arctan \zeta(x)$ is the local angle with respect to the x axis and s is the arc length along the step. $L(t) = \int \mathrm{d}s$ is the total length of the step curve.

The temporal evolution of the angle θ depends on the normal velocity v_n and on an arbitrary tangential velocity v_t [20]:

$$\frac{\partial \theta}{\partial t} = v_t \, \kappa - \frac{\partial v_n}{\partial s}. \tag{3.21}$$

We choose v_t such that the relative arc length s/L is constant in time [20]:

$$v_t = \frac{s}{L} \int_0^L \mathrm{d}s' \, \kappa(s') \, v_n(s') - \int_0^s \mathrm{d}s' \, \kappa(s') \, v_n(s'). \tag{3.22}$$

This choice is well-suited for the subsequent discretization of the problem. It guarantees that equidistant points on the curve remain equidistant.

The normal velocity is determined by the evolution equation and takes the following form in intrinsic coordinates (assuming isotropic steps):

$$v_n = -\partial_s \left[\cos\theta \, \sin\theta - \frac{\beta + \cos\theta}{\beta + 1} \partial_s \kappa \right]. \tag{3.23}$$

Here time t has been rescaled by $4\ell^4/\epsilon^2 \Gamma(D_\mathrm{S}\ell + D_\mathrm{L} a)$ and the spatial variables x and ζ by $\sqrt{2}\ell/\sqrt{\epsilon}$. Furthermore we have introduced the parameter $\beta = D_\mathrm{L} a / D_\mathrm{S} \ell$, which describes the dominant stabilization mechanism: For $\beta = 0$ there is no line diffusion along the step ($D_\mathrm{L} = 0$) and stabilization is due to terrace diffusion. For $\beta \to \infty$ stabilization is only due to line diffusion.

We also need to keep track of the total length $L(t)$ of the step curve, which evolves according to [20]:

$$\frac{\partial L}{\partial t} = \int_0^L \mathrm{d}s'\, \kappa(s')\, v_n(s'). \tag{3.24}$$

In order to implement a numerical scheme we first discretize the step curve $\theta(s)$ along s by introducing a mesh of n points $s_i = i/n \cdot L$ and the corresponding angles $\theta_i \equiv \theta(s_i)$. Derivatives with respect to s are approximated by finite differences. The resulting system of ordinary differential equations for $\theta_i(t)$ and $L(t)$ can now be solved with a standard ODE solver [50].

3.4. Step dynamics in the isotropic model

In this section we want to recapitulate the features of the isotropic evolution equation that are relevant to our study of anisotropic step meandering. A full description of the isotropic problem and its solution can be found in the literature [19, 20, 45].

Fig. 3.4 shows results of a numerical integration of the evolution equation in a box with periodic boundary conditions and a horizontal extent of $8\lambda_\mathrm{m}$. Initially straight steps (with small-amplitude random perturbation) develop a cellular pattern, whose wavelength is close to the wavelength $\lambda_\mathrm{m} = 2\pi\sqrt{2}$ of the most unstable mode. The amplitude of the meander first increases exponentially with time, which is in agreement with the prediction of the linear stability analysis. Later the growth of the amplitude slows down but there is no saturation. Instead, the amplitude grows asymptotically like $t^{1/2}$.

In stark contrast to the behaviour of the amplitude, which develops indefinitely, the wavelength of the emerging pattern is frozen at the wavelength λ_m of the most unstable mode. The pattern does not exhibit coarsening.

At late time the meander is characterized by the formation of plateaus, which are separated by steep slopes. In fact, the maximum slope diverges in time, so that locally the distance between neighbouring steps approaches zero [20].

Furthermore, the meander enjoys the up-down (or front-back) symmetry. This symmetry is broken for large enough flux if higher-order terms in the ϵ expansion are taken into account [20]. This symmetry breaking is confirmed by lattice gas simulations of the BCF model [45].

In the presence of elastic step-step interactions, this simple scenario changes. The amplitude still behaves asymptotically like $t^{1/2}$, but now the wavelength also develops. Instead of a fixed meandering wavelength, persistent coarsening is observed. In the asymptotic regime, the average wavelength $\langle\lambda\rangle$ increases like $t^{1/4}$ if line diffusion is present, without line diffusion it increases like $t^{1/6}$. Also, the meander does not exhibit plateaus, but instead assumes a triangular shape [39].

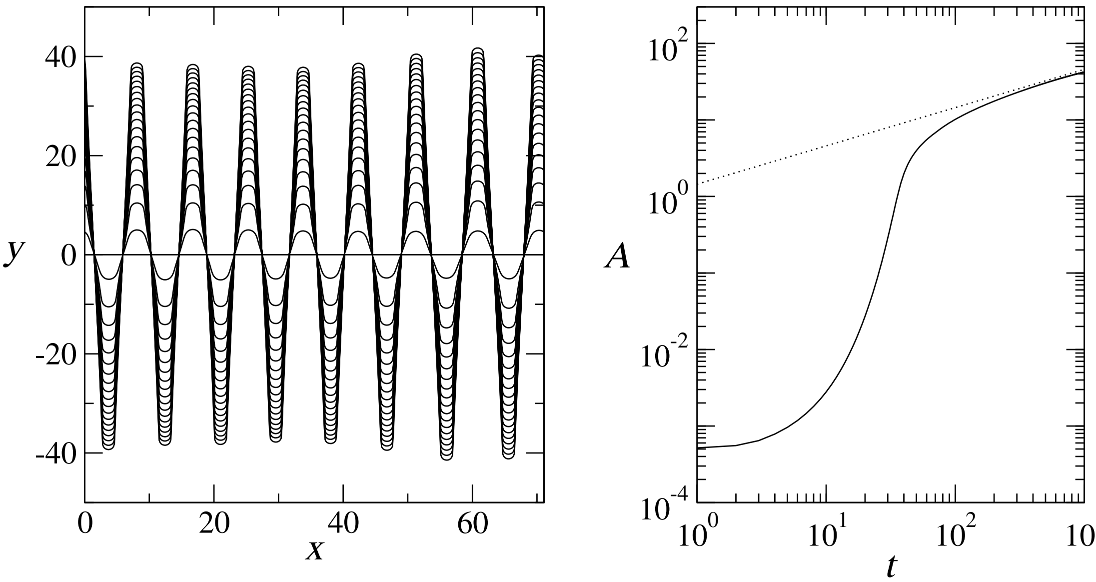

Figure 3.4.: Simulation of the evolution equation in a periodic box with horizontal size $8\lambda_{\mathrm{m}}$. The left panel shows the meander at different times (the time between subsequent snapshots is 50), the right panel shows the development of the amplitude A (solid line). The dotted line indicates the predicted asymptotic behaviour $A \sim t^{1/2}$.

In the following chapter we shall contrast these two basic scenarios (no coarsening *vs* endless coarsening) with a very different scenario that arises from crystal anisotropy. But before we proceed in this direction, we want to compare the prediction of the isotropic evolution equation with a numerical integration of the full BCF model.

3.5. Solving the full isotropic model

The numerical integration of the full BCF model is difficult due to the free-boundary character of the problem. For this reason, lattice gas simulations were employed to check the predictions of the evolution equation [45]. The predicted asymptotic behaviour of the amplitude, the absence of coarsening, and the front-back symmetry breaking of the meander were indeed confirmed by lattice gas simulations of the BCF model [45].

However, in order to perform a quantitative comparison of the evolution equation with the full model, a non-stochastic numerical integration with standard PDE solvers is useful. Here we try to take this approach, but we have to make strong restrictions in order to arrive at a problem whose numerical solution is feasible. We assume in-phase meandering and restrict the lateral size of the simulated system to the wavelength of the most unstable mode. Our main aim is to check the asymptotic behaviour of the amplitude.

To this end, we first write the quasistatic BCF equations in dimensionless form:

$$0 = \nabla^2 u + \epsilon, \tag{3.25}$$

$$u|_+ = \kappa, \tag{3.26}$$

$$\partial_n u|_- = 0, \tag{3.27}$$

$$v_n = \partial_n u|_+. \tag{3.28}$$

Here u is the reduced concentration of adatoms, κ is the dimensionless curvature, and $\epsilon \equiv \Omega F \ell^3 / \Gamma D_\mathrm{S}$ is consistent with our previous definition of the small parameter. The distance between neighbouring steps is 1. Space is measured in terms of ℓ, time in terms of $\ell^3/\Gamma D_\mathrm{S}$, and concentration in terms of $c_\mathrm{eq}^0 \Gamma/\ell$. We have assumed that stabilization is due to terrace diffusion only ($D_\mathrm{L} = 0$).

In order to avoid the need of tracking a free boundary, we employ a time-dependent coordinate transformation that maps the terrace onto a rectangular (and time-independent) domain. At the same time we can employ the known scaling of the wavelength and of the amplitude to obtain a meander that is compatible with the one from the evolution equation. Thus, our coordinate transformation takes the form

$$x \;\longrightarrow\; \xi = \epsilon^{1/2}\, x, \tag{3.29}$$

$$y \;\longrightarrow\; \eta = y - \zeta(x,t) - V_0\, t, \tag{3.30}$$

$$t \;\longrightarrow\; \tau = \frac{1}{2}\epsilon^2\, t, \tag{3.31}$$

and the step curve is now written as

$$Z(\xi,\tau) = \epsilon^{1/2}\, \zeta(x,t). \tag{3.32}$$

As the adatom concentration u also scales with the deposition flux, we have to introduce

$$U(\xi,\eta,\tau) = \frac{1}{2}\epsilon^{-1/2}\, u(x,y,t). \tag{3.33}$$

Under the above transformation the diffusion equation becomes

$$0 = \Big[\epsilon\, \partial_{\xi\xi} + (1+Z'^2)\, \partial_{\eta\eta} - 2\epsilon^{1/2}\, Z'\, \partial_{\xi\eta} - \epsilon^{1/2}\, Z''\, \partial_\eta\Big]\, U + 2\epsilon^{1/2} \tag{3.34}$$

and the boundary conditions take the form

$$U|_{\eta=0} = -\frac{Z''}{(1+Z'^2)^{3/2}}, \tag{3.35}$$

$$\Big[(1+Z'^2)\, \partial_\eta - \epsilon^{1/2}\, Z'\, \partial_\xi\Big]\, U\Big|_{\eta=1} = 0. \tag{3.36}$$

Finally, the equation for the meander $Z(\xi,\tau)$ reads

$$\partial_\tau Z = \Big[(1+Z'^2)\,\partial_\eta - \epsilon^{1/2}\,Z'\,\partial_\xi\Big]\,U\Big|_{\eta=0}\,. \tag{3.37}$$

Up to this point we have merely followed the steps that are taken in the derivation of the evolution equation. But here we do not perform an ϵ expansion that we truncate at some order, instead we seek a full numerical solution of Eqs. (3.34–3.37).

In order to set up a numerical scheme, we first discretize the step curve $Z(\xi,\tau)$ and the concentration field $U(\xi,\eta,\tau)$ in the ξ direction. Hence we introduce a mesh of n lines with coordinates $\xi_i = i/n\cdot\lambda_\mathrm{m}$, where $\lambda_\mathrm{m} = 2\pi\sqrt{2}$ is the wavelength of the most unstable mode. Partial derivatives with respect to ξ are replaced by finite differences. This procedure reduces the $(2+1)$-dimensional[1] partial differential equation (3.34) for the diffusion field $U(\xi,\eta,\tau)$ to a system of n coupled $(1+1)$-dimensional partial differential equations for the functions $U_i(\eta,\tau) \equiv U(\xi_i,\eta,\tau)$.

The dynamics of the step curve is now described by the evolution of the functions $Z_i(\tau) \equiv Z(\xi_i,\tau)$, which are governed by n ordinary differential equations that stem from the discretization of Eq. (3.37).

We now have to integrate a system of n partial differential equations which are coupled to a system of n ordinary differential equations. Problems of this sort are common: General solvers, which perform the time integration for given initial conditions can be found in numerical libraries. For our simulations we chose routine `D03PHF` from the NAG library [36].

Fig. 3.5 shows results of a simulation with $\epsilon = 0.01$. The characteristic shape of the meander with steep slopes and plateaus is confirmed. Also, the meander displays the up-down symmetry, which is due to the small value of ϵ. At late time the formation of plateaus is observed and the meander amplitude approaches the predicted $t^{1/2}$ behaviour.

Our numerical method was able to integrate the dynamical equations up to $t \approx 300$, where the meander amplitude A is about 25. At this point, further integration became difficult due to numerical inaccuracy and high demand of computing time. Later we shall see that important anisotropy effects are observed long before a meander amplitude of 25 is reached. It thus seems safe to use the amplitude equation to study the meandering of anisotropic crystal steps.

---

[1] Two space dimensions and the time dimension.

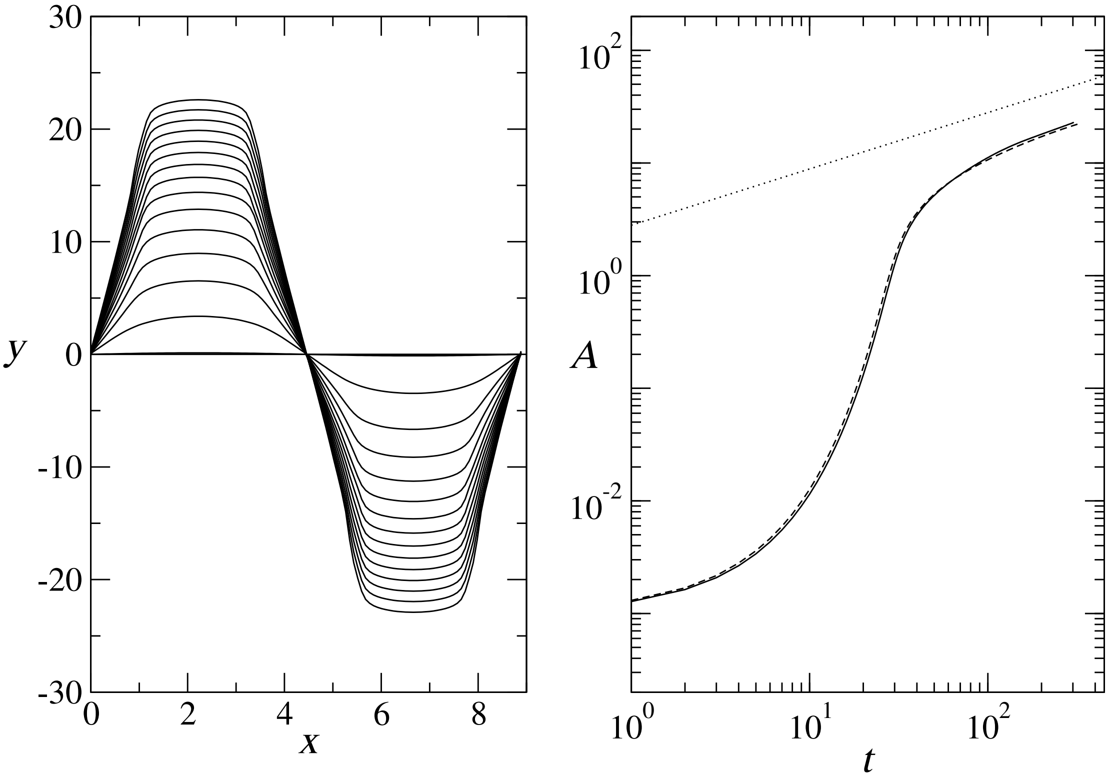

Figure 3.5.: Simulation of the quasistatic BCF model with an infinite Ehrlich-Schwoebel barrier. The left panel shows the meander at different times (the time between subsequent snapshots is 20), the right panel shows the development of the amplitude. Here the solid line corresponds to the full simulation and the dashed line to the numerical integration of the evolution equation. The dotted line indicates the predicted asymptotic behaviour. The expansion parameter is given by $\epsilon = 0.01$

4. Anisotropic step meandering

The high structural order of crystals gives rise to anisotropic physical properties. Here we are concerned with crystal growth, which is a surface process, and the relevant anisotropies stem from the structure of the surface. There is much evidence from experiments and from theoretical studies that all material parameters which enter into the BCF equations are anisotropic: the line stiffness, the line diffusion coefficient, the kinetic coefficients, and the terrace diffusion coefficient.

In many previous theoretical studies on step meandering, crystalline anisotropy has been neglected. Bales and Zangwill, who did the first analysis, pointed out that anisotropy does not lead to qualitative changes of the results that are obtained for the isotropic model [3]. While this is true within the scope of linear analysis, we shall here show that anisotropy leads to nontrivial nonlinear effects that influence the observed meandering pattern. In particular, the ripple wavelength can be drastically affected by anisotropy, which must be taken into account when comparing the step-flow model with experimental data.

As the precise form of anisotropies is seldom known, we must rely on model anisotropies but we shall show that our results do not depend on the precise anisotropy form. Also, the analysis is easily adapted to any kind of anisotropy.

4.1. Step stiffness and line diffusion

For simplicity and in order to make clear the basic strategy, we start our analysis of anisotropic meandering steps within the one-sided model. Furthermore we assume isotropic terrace diffusion. This simplified model still allows us to study the influence of Γ and D_{L} anisotropy on the meandering instability. Later we shall generalize our results and show that the basic features remain valid within the two-sided model.

4.1.1. Modelling anisotropy

As we pointed out at the beginning of this chapter, the precise anisotropies of surface quantities are seldom known. The results that we present in this chapter are generic in the sense that their qualitative features do not depend on the precise form of the anisotropies but mainly on their strength and orientation.

Nevertheless, in order to give some definite results we have to introduce model anisotropies. To this end we write the stiffness Γ and the line diffusion coefficient D_{L} as

$$\Gamma(\theta) = \Gamma_0\, A_\Gamma(\theta), \tag{4.1}$$

$$D_{\mathrm{L}}(\theta) = D_{\mathrm{L}0}\, A_{\mathrm{L}}(\theta), \tag{4.2}$$

with the anisotropy functions

$$A_\Gamma(\theta) = 1 + \epsilon_\Gamma \cos\left[4(\theta - \theta_\Gamma)\right], \tag{4.3}$$

$$A_{\mathrm{L}}(\theta) = 1 + \epsilon_{\mathrm{L}} \cos\left[4(\theta - \theta_{\mathrm{L}})\right]. \tag{4.4}$$

Each anisotropy function is characterized by two parameters, the strengths ϵ_Γ and ϵ_{L} (which lie in $[0, 1]$) and the reference angles θ_Γ and θ_{L}, which are determined by the average orientation of the steps on the surface. In Fig. 4.1 we show the form of the anisotropy for various values of $\epsilon_{\Gamma,\mathrm{L}}$ and $\theta_{\Gamma,\mathrm{L}}$.

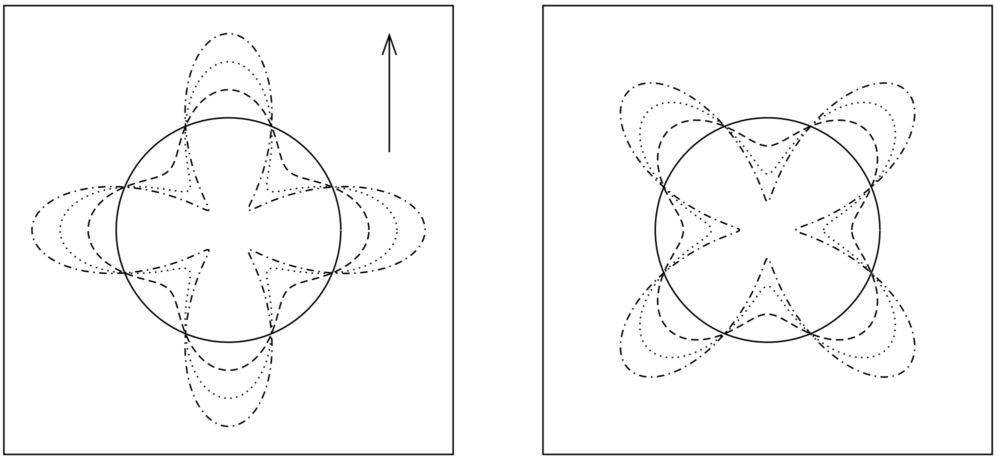

Figure 4.1.: Polar plot of the anisotropy function $A_{\Gamma,\mathrm{L}}$ for different strengths and orientations. In the left panel, $\theta_{\Gamma,\mathrm{L}} = 0$ and in the right panel, $\theta_{\Gamma,\mathrm{L}} = \pi/4$. In both plots the anisotropy strengths $\epsilon_{\Gamma,\mathrm{L}}$ are as follows: 0 (solid line), 0.25 (dashed line), 0.5 (dotted line), 0.75 (dot and dash line). The arrow points in the direction of the step train.

These model anisotropies have a fourfold symmetry. We shall give quantitative results only for this type of symmetry but we shall briefly discuss the case of other symmetries.

4.1.2. Steady-state analysis

A systematic analysis of the effect of anisotropy on the meandering dynamics can start with an analysis of steady-state solutions of the evolution equation, i. e., solutions that satisfy $\partial_t\zeta = 0$. From the evolution equation (3.16) it is obvious that there is always a trivial (unstable) steady state ($\zeta \equiv 0$), regardless of anisotropy. In the following we are interested in non-trivial *periodic* steady states.

In order to find periodic steady-state solutions of the evolution equation (3.16) we take advantage of the fact that this equation assumes the form of a conservation law,

$$\partial_t\zeta + \partial_x j = 0, \tag{4.5}$$

where

$$j = \frac{\Omega F \ell^2}{2} \frac{\partial_x\zeta}{1+(\partial_x\zeta)^2} - \left(\frac{D_{\mathrm{S}}\ell}{1+(\partial_x\zeta)^2} + \frac{D_{\mathrm{L}}a}{[1+(\partial_x\zeta)^2]^{1/2}} \right) \partial_x(\Gamma\kappa) \tag{4.6}$$

is a mass current along the step.

For the moment we shall assume that $\theta_{\Gamma,\mathrm{L}}$ is 0 or $\pi/4$, so that the evolution equation enjoys the $x \to (-x)$ symmetry, and seek steady-state solutions that satisfy $j = 0$. Due to translational invariance, the flux j does not depend on ζ but only on derivatives of ζ with respect to x. It is thus useful to introduce the "slope"

$$m = \sin\theta = \frac{\partial_x\zeta}{[1+(\partial_x\zeta)^2]^{1/2}} \tag{4.7}$$

and to express $\partial_x\zeta$ and higher derivatives in terms of m. After performing a change of the spatial variable x,

$$x \quad \longrightarrow \quad y = \frac{x}{\alpha_\Gamma A_\Gamma} \tag{4.8}$$

with $\alpha_\Gamma = \Gamma_0/\Gamma(0)$, we can write the condition $j = 0$ in the form

$$2\left(\frac{\lambda_{\mathrm{m}}}{4\pi}\right)^2 \partial_{yy} m = -\frac{\partial V}{\partial m}, \tag{4.9}$$

which is analogous to Newton's equation of motion for a particle of mass $2(\lambda_{\mathrm{m}}/4\pi)^2$ in the one-dimensional potential

$$V(m) = \int_{m_0}^{m} \frac{\alpha_\Gamma A_\Gamma(m')\, m'\, \mathrm{d}m'}{\tilde\beta\sqrt{1-m'^2} + (1-\tilde\beta)\, \alpha_{\mathrm{L}} A_{\mathrm{L}}(m')}. \tag{4.10}$$

For brevity we have set $\tilde\beta = D_{\mathrm{S}}\ell/[D_{\mathrm{S}}\ell + D_{\mathrm{L}}(0)\, a]$ and $\alpha_{\mathrm{L}} = D_{\mathrm{L}0}/D_{\mathrm{L}}(0)$.

In the same way as one can obtain the period of an oscillator in an anharmonic potential [33], we can here obtain the wavelength λ_0 of the steady-state solution by evaluating

$$\lambda_0 = 2\int_{-\lambda_0/4}^{\lambda_0/4} \mathrm{d}x = 2\int_{-m_0}^{m_0} \frac{\alpha_\Gamma A_\Gamma(m)}{\partial_y m}\,\mathrm{d}m$$
$$= \frac{\lambda_\mathrm{m}}{2\pi}\int_{-m_0}^{m_0} \frac{\alpha_\Gamma A_\Gamma(m)}{\left[V(m_0) - V(m)\right]^{1/2}}\,\mathrm{d}m. \tag{4.11}$$

The family of steady-state wavelengths λ_0 is parameterized by m_0, which is the value of m that corresponds to the highest slope in the step meander (and the analogue to the amplitude in the oscillator picture).

Now it is an easy task to compute the branches of steady-state solutions for specific anisotropies. In Fig. 4.2 we show $\lambda_0(m_0)$ for a system that has only Γ anisotropy and for another system that has only D_L anisotropy. It can be seen that for $\theta_{\Gamma,\mathrm{L}} = 0$ the wavelength λ_0 of steady-state solutions is below (or equal to) λ_c, the critical wavelength of linear instability. The same qualitative behaviour is observed for isotropic systems.

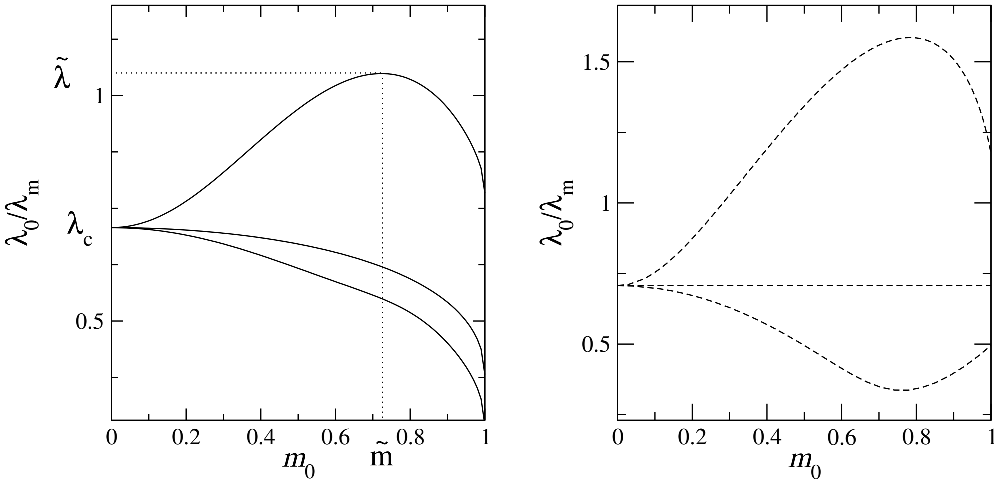

Figure 4.2.: Wavelength λ_0 of steady-state solutions as a function of parameter m_0. Solid lines are for Γ, dashed lines for D_L anisotropy. In both cases from lower to upper curve: $\epsilon_{\Gamma,\mathrm{L}} = 0.7$ with $\theta_{\Gamma,\mathrm{L}} = 0$, $\epsilon_{\Gamma,\mathrm{L}} = 0$, and $\epsilon_{\Gamma,\mathrm{L}} = 0.7$ with $\theta_{\Gamma,\mathrm{L}} = \pi/4$.

However, for $\theta_{\Gamma,\mathrm{L}} = \pi/4$, steady-state solutions exist whose wavelength is larger than λ_c. The wavelength reaches a local maximum $\tilde{\lambda}$, which increases with increasing strength of the anisotropy. From Eq. (4.11) one can conclude that the maximum behaves with the anisotropy strength like

$$\frac{\tilde{\lambda}_{\Gamma,\mathrm{L}}}{\lambda_\mathrm{c}} \sim \frac{1}{(1-\epsilon_{\Gamma,\mathrm{L}})^{1/2}} \quad \text{for} \quad \epsilon_{\Gamma,\mathrm{L}} \to 1. \tag{4.12}$$

4.1.3. Interrupted coarsening

For $\theta_{\Gamma,\mathrm{L}} = 0$ (left panel in Fig. 4.1) the structure of the steady-state branch is similar to the one for an isotropic system: All available wavelengths $\lambda_0(m_0)$ are smaller than the critical wavelength λ_c (lower curves in Fig. 4.2). This observation suggests that the meandering dynamics of anisotropic steps with $\theta_{\Gamma,\mathrm{L}} = 0$ does not differ qualitatively from isotropic systems. Indeed, this is what we find from numerical integrations of the evolution equation (3.16). The meandering pattern is similar to the one in Fig. 3.4, which was obtained for the isotropic model; due to anisotropy there is only a slight modification of the step shape. But most importantly, there is no coarsening and the amplitude of the steps grows asymptotically like $t^{1/2}$.

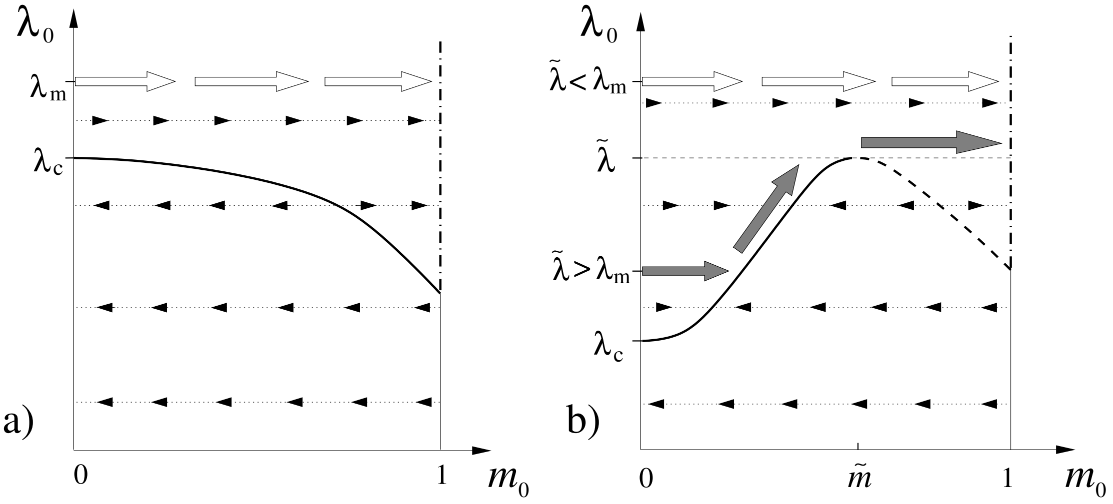

Figure 4.3.: Schematic of the meandering dynamics in the λ_0-m_0 plane for anisotropy orientation $\theta_{\Gamma,\mathrm{L}} = 0$ (a) and for orientation $\theta_{\Gamma,\mathrm{L}} = \pi/4$ (b). Thick white and grey arrows indicate the meandering dynamics, small black arrows the stability of steady-state solutions (see text).

It is instructive to visualize the meandering dynamics in the λ_0-m_0 plane [13], as shown in Fig. 4.3 a). Small m_0 corresponds to small amplitude (initial conditions: $m_0 \approx 0$), large m_0 corresponds to large amplitude. As the maximum amplitude always increases, the direction of time is from left to right.

At an early stage of the instability ($m_0 \approx 0$), the wavelength λ_m of the most unstable mode is selected. The instability drives the meander towards larger and larger amplitudes (white arrows). As there are no periodic steady-state solutions whose wavelength is close to λ_m, the meandering wavelength does not change in time.

This scenario is changed completely if $\theta_{\Gamma,\mathrm{L}} = \pi/4$ and the anisotropy is strong enough so that $\tilde\lambda$ exceeds λ_m. In Fig. 4.4 we show the simulation of a system with a lateral extent of $15\,\lambda_\mathrm{m}$, starting from random step fluctuations of small amplitude. The snapshots of the meander clearly show that the system undergoes a coarsening process. The interesting point is that this coarsening process does not continue forever but is interrupted when the number of cells is reduced from the initial number of 16 to the final number of four. In this example, $\tilde{\lambda} \approx 3.1\,\lambda_\mathrm{m}$ and the final width of all cells is larger than $\tilde{\lambda}$.

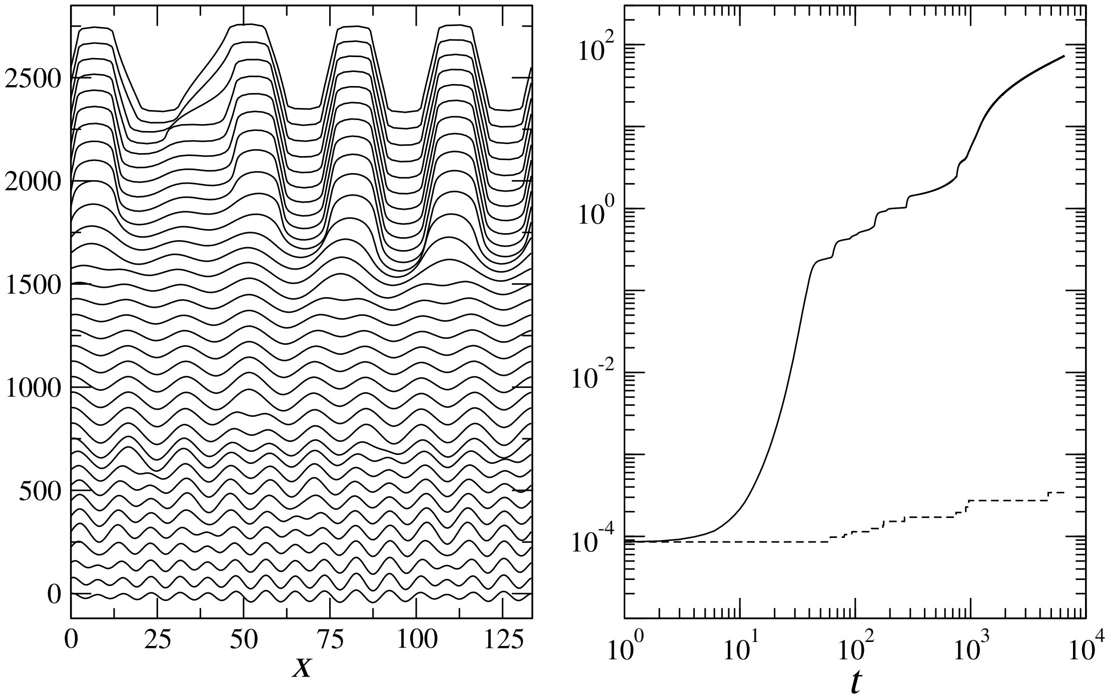

Figure 4.4.: Interrupted coarsening. In this example, steps are stabilized by anisotropic line diffusion ($D_\mathrm{S} = 0$) with $\epsilon_\mathrm{L} = 0.92$ and $\theta_\mathrm{L} = \pi/4$. The left panel shows the meander at different time steps, the right panel shows the amplitude (solid line) and the average wavelength (dashed line) as a function of time. The meander snapshots have been arbitrarily rescaled for better visibility of the small undulations.

In the λ_0-m_0 picture, this observation is explained as follows [Fig. 4.3 b)]. At first, linear instability selects the pattern wavelength λ_m of the most unstable mode. As the meander amplitude (m_0) increases, the system approaches the steady-state branch (first grey arrow). These steady states are stable with respect to amplitude perturbation, so that the meander amplitude should saturate. However, the instability still drives the meander towards larger amplitude. In order to increase the amplitude further, the meandering step also increases its wavelength. Coarsening takes place (second grey arrow). After the maximum $\tilde{\lambda}$ of the steady-state branch is reached, there is no further need to change the wavelength.

Coarsening is interrupted at $\tilde{\lambda}$ and the amplitude increases without bound (third grey arrow).

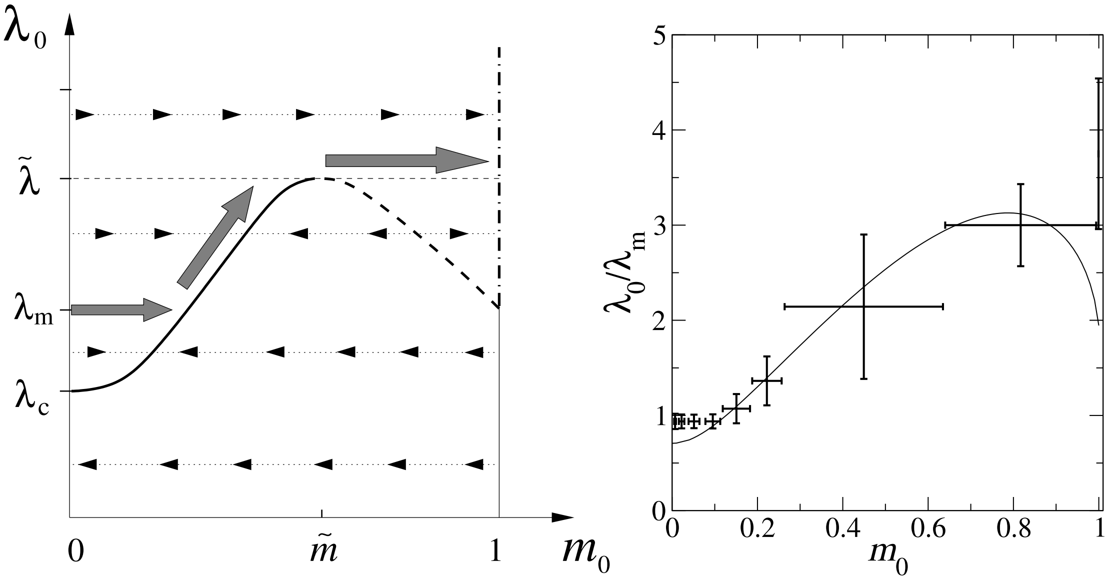

Figure 4.5.: The dynamics of interrupted coarsening. First the wavelength λ_m of the most unstable mode is selected. The amplitude of the cells grows until it comes close to the steady-state solution (thick black line in the left panel), where coarsening sets in. The wavelength increases until the average wavelength is larger than $\tilde{\lambda}$. Thereafter the average wavelength remains unchanged and the amplitude grows without bound. The right panel shows a calculated steady-state branch (full line, parameters $c^0_\mathrm{eq} = 0, \epsilon_\mathrm{L} = 0.92, \theta_\mathrm{L} = \pi/4$), the crosses are from a numerical simulation. The size of the error bars corresponds to the standard deviation of m_0 and λ_0 in the finite simulation box.

We can relate this discussion to the numerical simulation from Fig. 4.4. For this purpose we identify λ_0 with the average wavelength $\langle\lambda\rangle$ of the simulated meander and m_0 with the mean value $\langle m_0\rangle$ of the maximum slopes in the cells. At selected points we add the numerical values to the plot of the steady-state branch (see Fig. 4.5). The size of the error bars results from the standard deviation of λ_0 and m_0. They are comparatively large due to finite-size effects. Nevertheless, the plot clearly shows that, during the critical period, the dynamics is guided by the steady-state branch.

It should be stressed that the scenario of interrupted coarsening only takes place if anisotropy is strong enough. If $\tilde{\lambda} < \lambda_\mathrm{m}$, the dynamics is not affected by the presence of steady-state solutions above λ_c. The wavelength is then fixed (white arrows in Fig. 4.3 b).

In summary, we have found the following two scenarios for anisotropic meandering steps:

1. If $\theta_{\Gamma,\mathrm{L}} = 0$, or $\theta_{\Gamma,\mathrm{L}} = \pi/4$ *and* $\tilde{\lambda} < \lambda_{\mathrm{m}}$, the average pattern wavelength is λ_{m} according to linear instability and there is no coarsening.

2. If $\theta_{\Gamma,\mathrm{L}} = \pi/4$ *and* $\tilde{\lambda} > \lambda_{\mathrm{m}}$, the pattern undergoes a coarsening process that is interrupted when the width of all cells has reached $\tilde{\lambda}$.

Our explanation of interrupted coarsening with the help of the steady-state branch of the step evolution equation rests on plausibility arguments and numerical evidence. Recently the supposed link between steady states and the coarsening dynamics has been proven analytically for two special classes of one-dimensional evolution equations: the generalized Ginzburg-Landau equation and the generalized Cahn-Hilliard equation [49]. A rigorous proof for the step evolution equation (3.16) is still missing but there is now little doubt that the scenario of interrupted coarsening is correct.

We have seen that there are two very different scenarios for the meandering dynamics and that it depends mainly on the orientation of the anisotropy, which scenario becomes relevant. An intuitive understanding of the fact that coarsening occurs for the orientation $\theta_{\Gamma,\mathrm{L}} = \pi/4$ and not for the orientation $\theta_{\Gamma,\mathrm{L}} = 0$ can be gained from Fig. 4.6. Steps tend to develop “facets” along the directions of maximum line stiffness or line diffusion. In the case of $\theta_{\Gamma,\mathrm{L}} = \pi/4$, the direction of the facets promotes a horizontal displacement of the curved regions and thus cell coalescence. For $\theta_{\Gamma,\mathrm{L}} = 0$ the directions of the facets coincide with the directions of the plateaus and of the high slopes, and coarsening is suppressed.

At the end of this section on interrupted coarsening we want to discuss the case where the $x \to (-x)$ symmetry of the evolution equation is lost, i. e., where the orientation of the anisotropy is not 0 or $\pi/4$.

As there is interrupted coarsening for $\theta_{\Gamma,\mathrm{L}} = \pi/4$ but not for $\theta_{\Gamma,\mathrm{L}} = 0$, there must be a critical angle θ^* below which interrupted coarsening does not occur. This angle depends on the strength of the anisotropy.

In order to find the critical angle θ^* as a function of the anisotropy strength, we have integrated the evolution equation for a given $\epsilon_{\Gamma,\mathrm{L}}$ in a periodic box of width λ_{m}. If the step meander approaches a steady-state solution, interrupted coarsening is to be expected in an extended system, otherwise there will be no coarsening. Varying $\theta_{\Gamma,\mathrm{L}}$, we found an approximation of θ^* by means of nested intervals. The resulting critical angles are plotted in Fig. 4.7. It can be seen that there is both a minimum anisotropy strength and a minimum angle below which interrupted coarsening does not occur.

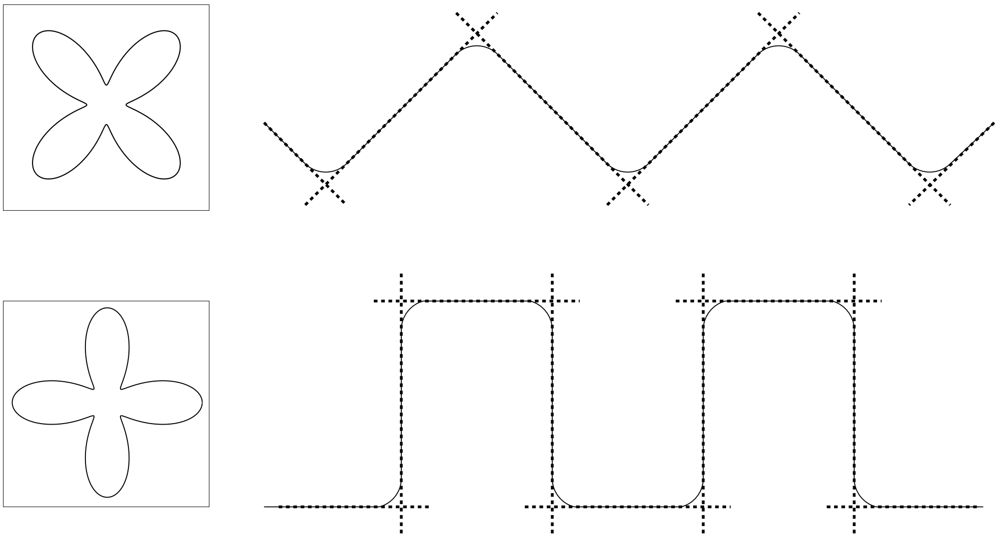

Figure 4.6.: An intuitive explanation why there is coarsening for $\theta_{\Gamma,\mathrm{L}} = \pi/4$ (upper figure) and not for $\theta_{\Gamma,\mathrm{L}} = 0$ (lower figure). The step develops facets along the directions of maximum line stiffness or line diffusion. In the first case, the horizontal displacement of the curved regions is enhanced and cell coalescence takes place; in the second case it is suppressed.

4.1.4. Drifting patterns

In the previous section on interrupted coarsening we were mainly concerned with anisotropies whose orientation is 0 or $\pi/4$. Only at the end we addressed the case of different orientations where the evolution equation loses its $x \to (-x)$ symmetry. We now continue at this point and raise the question whether the breaking of this symmetry leads to drifting meandering patterns.

Surprisingly, numerical solutions of the evolution equation (3.16) for $\theta_{\Gamma,\mathrm{L}} \neq 0, \pi/4$ do not reveal a drift of the step meander. This observation is explained by the fact that the evolution equation for the slope $\partial_x \zeta$ always possesses the $x \to (-x)$ symmetry, regardless of (fourfold) anisotropy. It is a consequence of the fact that the evolution equation for the meander ζ always enjoys the $(x, \zeta) \to (-x, -\zeta)$ symmetry.

If the expansion with respect to ϵ is carried out to subdominant order, the evolution equation takes a more complicated form:

$$\begin{aligned}\partial_t \zeta = -\partial_x \Bigg\{ & \frac{\Omega F \ell^2}{2} \frac{\partial_x \zeta}{1 + (\partial_x \zeta)^2} \left[1 - \frac{\kappa \ell}{3} \frac{3 + (\partial_x \zeta)^2}{[1 + (\partial_x \zeta)^2]^{1/2}} \right] \\ & - \left[\left(\frac{D_\mathrm{S} \ell}{[1 + (\partial_x \zeta)^2]^{1/2}} + D_\mathrm{L}(\theta)\, a \right) - \frac{D_\mathrm{S} \ell^2 \kappa}{2} \right] \frac{\partial_x [\Gamma(\theta)\, \kappa]}{[1 + (\partial_x \zeta)^2]^{1/2}} \Bigg\}. \end{aligned} \tag{4.13}$$

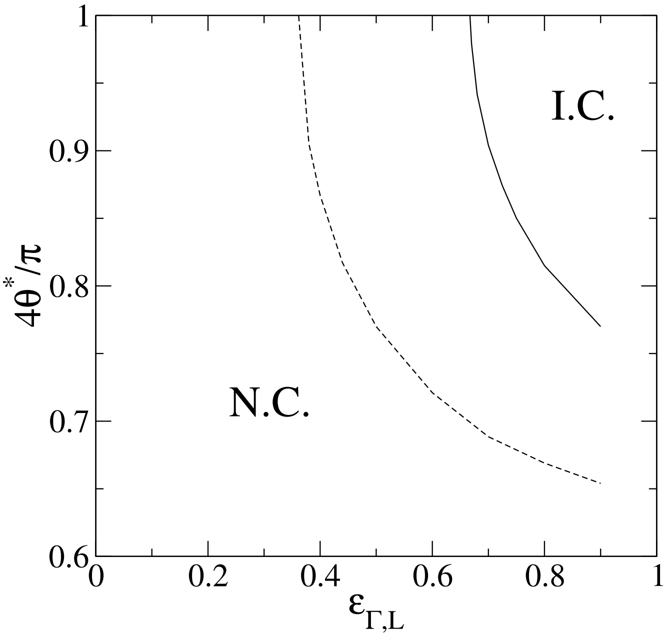

Figure 4.7.: The critical angle θ^* as a function of the anisotropy strength. The solid line is for Γ, the dashed line for D_L anisotropy. The region of interrupted coarsening is indicated by I.C, the region without coarsening by N.C.

In particular, the $(x, \zeta) \to (-x, -\zeta)$ symmetry of the leading-order equation (3.16) is now lost. Simulations of Eq. (4.13) indeed reveal a drift if $\theta_{\Gamma,\mathrm{L}} \neq 0, \pi/4$.

A simple scaling law that describes the drift velocity v_d as a function of the incoming flux F can be derived (see App. C). In dimensionless units it takes the form

$$v_\mathrm{d} = \epsilon^{1/2} f(\tilde{\beta}, A_\Gamma, A_\mathrm{L}, \lambda_0). \tag{4.14}$$

Here f is a function that depends on the precise form of the anisotropies and on the wavelength λ_0 of the steady-state solution.

We have checked the $\epsilon^{1/2}$ dependence numerically by solving the evolution equation in a periodic box of size λ_0. The results are shown in Fig. 4.8. In the same figure we also give the dependence of the drift velocity on λ_0.

Expressed in physical units, the drift velocity reads:

$$v_\mathrm{d} = \frac{\Omega^2 F^2 \ell^4}{4 D_\mathrm{S} \Gamma(0)}\, g(\tilde{\beta}, A_\Gamma, A_\mathrm{L}, \lambda_0). \tag{4.15}$$

Here we see that the drift velocity scales like F^2, whereas the average step velocity behaves like F. Thus, it should be possible to control the drift of the structures by choosing the appropriate flux rate.

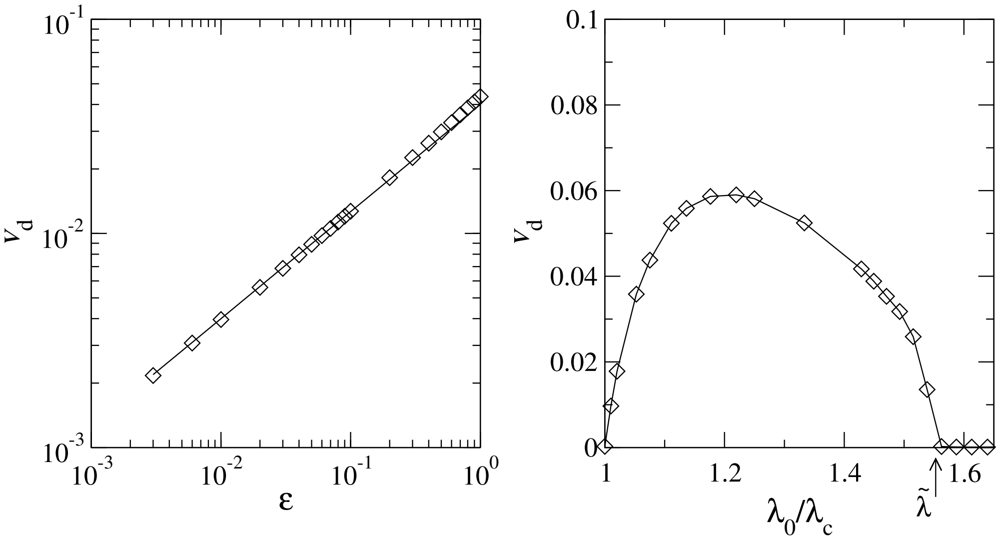

Figure 4.8.: Drift velocity v_d as a function of the expansion parameter ϵ and as a function of the wavelength $\lambda_0/\lambda_\mathrm{c}$ of steady-state solutions. Both graphs are for the case where stabilization is due to line diffusion only ($D_\mathrm{S} = 0$). The anisotropy is given by $\epsilon_\mathrm{L} = 0.5$ and $\theta_\mathrm{L} = 0.8\,\pi/4$. In the right graph: $\epsilon = 1$.

4.1.5. Interplay with elasticity

Coarsening of the meandering pattern is not only due to anisotropy, it can also be due to elastic step-step interactions [39]. In this case the step chemical potential is modified as follows (to first order in our expansion):

$$\mu = \Omega\left(\tilde{\gamma}(\theta)\,\kappa + 3A\frac{\kappa}{\ell_\perp^2}\left[1 + 2\,(\partial_x\zeta)^2\right]\right), \tag{4.16}$$

where $\ell_\perp = \ell/[1 + (\partial_x\zeta)^2]^{1/2}$ is the effective local step distance. In Eq. (4.16) the first term (with $\tilde{\gamma}$) stems from the Gibbs-Thomson effect and the second term from elasticity. A measures the strength of the elastic interaction.

Without anisotropy the following is observed [39]: The system exhibits perpetual coarsening and the average wavelength behaves asymptotically like t^α, where $\alpha = 1/4$ if line diffusion is present and $\alpha = 1/6$ if it is not. The typical behaviour of the amplitude is not affected by elasticity, asymptotically it still grows like $t^{1/2}$.

In the $\lambda_0(m_0)$ picture, the emergence of perpetual coarsening with diverging maximum slope is related to the divergence of the branch of steady states at $m_0 = 1$. Doing a steady-state analysis similar to the one without elasticity, we can write the wavelength λ_0 of steady-state solutions as

$$\lambda_0 = \frac{\lambda_\mathrm{m}}{2\pi}\int_{-m_0}^{m_0}\frac{F(m)}{(1-m^2)^2}\,\mathrm{d}m,$$

$$F(m) = \frac{(1-m^2)^2\,\alpha_\Gamma A_\Gamma(m) + C_1\,(1+m^2)}{(1+C_1)\,\left[V(m_0)-V(m)\right]^{1/2}}, \tag{4.17}$$

where the potential $V(m)$ is now defined by

$$\begin{aligned} V(m) &= \frac{1}{1+C_1}\int_{m_0}^{m} \frac{G(m')}{(1-m'^2)^2}\,\mathrm{d}m', \\ G(m) &= \frac{(1-m^2)^2\,\alpha_\Gamma A_\Gamma(m) + C_1\,(1+m^2)}{\left[(1-m^2)^{1/2}\tilde\beta + (1-\tilde\beta)\,\alpha_\mathrm{L} A_\mathrm{L}(m)\right]}\,m, \end{aligned} \tag{4.18}$$

and $C_1 = 3A/[\tilde\gamma(0)\,\ell^2]$ is a constant that determines the strength of the elastic interaction.

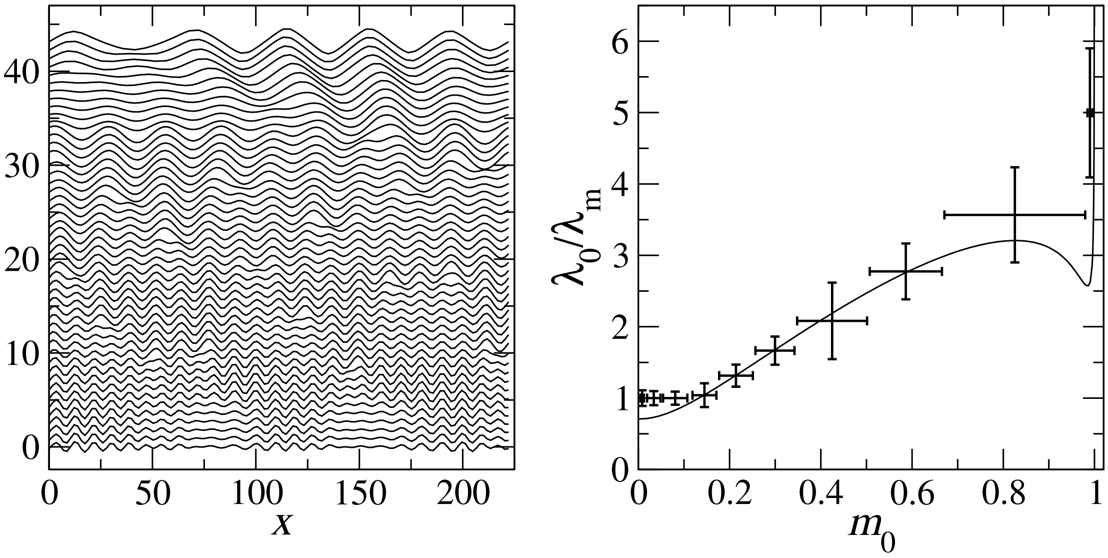

Figure 4.9.: Step meander with elastic step-step interactions and anisotropic D_L. The parameters are as follows: $c^0_\mathrm{eq} = 0$, $\epsilon_\mathrm{L} = 0.5$, $\theta_\mathrm{L} = \pi/4$, and $A = \tilde\gamma(0)\,\ell^2/30$. The left panel shows snapshots of the meander (with rescaled amplitude) and the right panel the corresponding steady-state branch and the dynamics of the simulated system. The divergence of the steady-state branch at $m_0 = 1$ shows that endless coarsening is restored.

Again, the shape of the steady-state branch gives a first idea about the coarsening dynamics. The right panel of Fig. 4.9 shows the steady-state branch of a system, for which one would expect interrupted coarsening due to anisotropy and perpetual coarsening due to elasticity. For small slope (m_0 not too close to 1) the curve is reminiscent of the case without elasticity and exhibits a local maximum $\tilde\lambda$. But for high slope elasticity restores steady states for arbitrary wavelength $\lambda_0 > \lambda_\mathrm{c}$.

The dominance of elasticity for $m_0 \approx 1$ can be understood from the form of the chemical potential, which for high slope ($\partial_x \zeta \to \infty$) is dominated by the elastic contribution.

The shape of the steady-state branch suggests that at an early stage of the instability the dynamics is dominated by anisotropy effects and that later, when the lateral cell size has reached $\tilde{\lambda}$, elasticity becomes more important and the known scenario of perpetual coarsening is reestablished.

We have checked the correctness of this scenario by a numerical integration of the corresponding evolution equation. Fig. 4.9 gives the results of a simulation with the following parameters: $c_{\mathrm{eq}}^0 = 0$, $\epsilon_{\mathrm{L}} = 0.5$, $\theta_{\mathrm{L}} = \pi/4$, and $A = \tilde{\gamma}(0)\,\ell^2/30$. The right panel of Fig. 4.9 shows that the results of this simulation are in good agreement with the predictions that were derived from the shape of the steady-state branch: As in the case without elastic interactions, the meandering dynamics is governed by the steady-state branch.

4.1.6. Discussion

We now want to discuss possible consequences of these findings for MBE experiments. For a qualitative statement it is sufficient to know the ratio of the largest value of Γ or D_{L} to the smallest value; the precise form of the anisotropy does not matter here.

For example, the Cu(100) surface can be modelled by a square lattice with nearest-neighbour interactions. The anisotropy of the step stiffness thus has a four-fold symmetry. At room temperature we find [18]

$$\eta_\Gamma = \frac{\Gamma_{[110]}}{\Gamma_{[100]}} \approx 86 \tag{4.19}$$

for the ratio of the largest stiffness (attained for [110] steps) to the smallest stiffness (for [100] steps).

Using our model anisotropy as a first approximation to the real anisotropy, we can infer from the structure of the steady-state branch the minimum ratio η_Γ, at which interrupted coarsening becomes relevant ($\tilde{\lambda}$ reaches λ_{m}):

$$\eta_\Gamma^{\mathrm{c}} = \frac{1 + \epsilon_\Gamma^{\mathrm{c}}}{1 - \epsilon_\Gamma^{\mathrm{c}}} \approx 5. \tag{4.20}$$

As η_Γ from the above example is much larger than the critical value η_Γ^{c}, it is likely that interrupted coarsening plays a role in the wavelength selection of meandering ripples on Cu(100) surfaces.

We can do a similar comparison for D_{L} anisotropy. Here it is known from kinetic Monte-Carlo simulations that, in the presence of a kink-rounding barrier, the ratio of the line diffusion coefficients for [110] and [100] steps is [34]

$$\eta_{\mathrm{L}} = \frac{D_{[110]}}{D_{[100]}} \approx 10. \tag{4.21}$$

The critical value obtained from our analysis (assuming isotropic stiffness) is

$$\eta_{\mathrm{L}}^{\mathrm{c}} = \frac{1+\epsilon_{\mathrm{L}}^{\mathrm{c}}}{1-\epsilon_{\mathrm{L}}^{\mathrm{c}}} \approx 2.13. \tag{4.22}$$

Here also, the critical ratio is much smaller than the ratio from our example, so that interrupted coarsening might be observed.

In our discussion of Γ and D_{L} anisotropy, we have concentrated on 4-fold anisotropies. On many crystal surfaces, however, anisotropies are 3-fold or 6-fold.

A repetition of the analysis for 3-fold and 6-fold anisotropies reveals no qualitative differences. If Γ or D_{L} attains its minimum value in the direction of the step train, then the steady-state branch has a maximum $\tilde{\lambda} > \lambda_{\mathrm{c}}$. If the anisotropy is strong enough, $\tilde{\lambda}$ is larger than λ_{m} and there is interrupted coarsening. But if Γ or D_{L} attains its maximum value in the step train direction, we find that $\lambda_0 < \lambda_{\mathrm{c}}$ for every steady-state solution, regardless of the strengths of the anisotropies. It follows that there is no interrupted coarsening in this case.

4.2. Attachment kinetics

4.2.1. Two-sided model

So far, we have only been concerned with the one-sided model, where, due to an infinite Ehrlich-Schwoebel barrier, adatoms do not descend the steps. Furthermore, the steps acted as perfect sinks. This amounted to setting

$$\nu_- = 0, \quad \nu_+ \to \infty \tag{4.23}$$

in the boundary conditions (2.13, 2.14) of the diffusion equation.

Now we want to consider surfaces with an arbitrary Ehrlich-Schwoebel effect, which may depend on the local step orientation. There are many examples from experiments and theory alike that suggest a strong anisotropy of the Ehrlich-Schwoebel barrier. On some metal surfaces, the energy barrier may even be inverted for certain step orientations [1].

In the following we shall use the attachment lengths d_+ and d_-, which are related to the kinetic coefficients via

$$d_+ = D/\nu_+, \quad d_- = D/\nu_-, \tag{4.24}$$

as the fundamental quantities to describe the Ehrlich-Schwoebel effect and its anisotropy.

Our programme starts with the linear stability analysis, which is performed along the same lines as the calculation for the one-sided model (see App. A). As the central result we obtain the following dispersion relation:

$$\begin{aligned}\mathrm{Re}(i\omega) = {} & \Omega F \frac{q}{\mathcal{D}} \frac{d_- - d_+}{\ell + d_+ + d_-} \Big[(d_- + d_+)(q\ell \, \sinh q\ell - \cosh q\ell + \cos\phi) \\ & + \frac{\ell}{2} q\ell \, (\sinh q\ell + \mathcal{S}_0 \sin\phi) \Big] \\ & - \Gamma q^2 \Big[D_\mathrm{S} \frac{q}{\mathcal{D}} \{ 2(\cosh q\ell - \cos\phi) \\ & + q\,(d_+ + d_-) \sinh q\ell \} + a D_\mathrm{L}\, q^2 \Big],\end{aligned} \tag{4.25}$$

$$\begin{aligned}\mathrm{Im}(i\omega) = {} & \Omega F \frac{q}{\mathcal{D}} \Big[(\ell + d_+ + d_-) \, \sin\phi \\ & + \frac{1}{2} q\ell \, \{ \mathcal{S}_1 \, (\cos\phi - \cosh q\ell) - \mathcal{S}_2 \, q\ell \, \sinh q\ell \} \Big]\end{aligned} \tag{4.26}$$

with

$$\mathcal{D} = (d_+ + d_-)\, q \, \cosh q\ell + \left(d_+ d_- q^2 + 1 \right) \sinh q\ell. \tag{4.27}$$

For brevity we have dropped the arguments of anisotropic model parameters. They have to be evaluated at the orientation of the unperturbed step (i. e., $\theta = 0$).

If we compare the dispersion relation of the anisotropic model with the corresponding dispersion relation for an isotropic surface [20], we notice the emergence of three additional terms, which are due to the anisotropies of the attachment lengths d_+ and d_-. These terms are recognized by the following prefactors:

$$\mathcal{S}_0 = \frac{(d'_+ - d'_-)\,\ell + 2\,(d'_+ d_- - d'_- d_+)}{(d_- - d_+)\,\ell}, \tag{4.28}$$

$$\mathcal{S}_1 = \frac{d'_+\,(\ell + 2d_-) + d'_-\,(\ell + 2d_+)}{\ell + d_+ + d_-}, \tag{4.29}$$

$$\mathcal{S}_2 = \frac{d'_+ d_-\,(1 + 2d_-/\ell) + d'_- d_+\,(1 + 2d_+/\ell)}{\ell + d_+ + d_-}. \tag{4.30}$$

$\mathcal{S}_0$, $\mathcal{S}_1$, and $\mathcal{S}_2$ depend on the first derivatives of the attachment lengths d_+ and d_- with respect to the angle (denoted by the prime) and vanish if d_+ and d_- enjoy the $\theta \to (-\theta)$ symmetry.

Attachment anisotropy is the first anisotropy that enters at the linear level. The reason for the emergence of new terms is quite transparent: The step perturbation $\varepsilon\zeta$ leads to a correction of the kinetic coefficients, which is of order ε. In the boundary conditions (2.13, 2.14) this first-order correction of the kinetic coefficients couples to the unperturbed concentration field at zeroth order, which leads to a correction of the attachment currents j_+ and j_-. If the kinetic coefficients do not enjoy the $\theta \to (-\theta)$ symmetry, the attachment currents will not be in phase with the step perturbation and the meander will drift sideways. This is indicated by the two new terms in the imaginary part of the growth rate, which do not vanish for the in-phase mode ($\phi = 0$).

The additional term in the real part of the growth rate has a different consequence: The most unstable mode may no longer be the in-phase mode. Attachment anisotropy can induce out-of-phase meandering, which gives rise to tilted meandering ripples.

It is important to point out why Γ and D_L anisotropy do not intervene in the dispersion relation. The reason is that Γ and D_L do not enter at all into the steady-state solution. Hence, at first order there are only contributions of $\Gamma(0)$ and $D_\mathrm{L}(0)$. Contrary to that, the values of $\nu_+(0)$ and $\nu_-(0)$ do enter into the steady-state solution, and $\nu'_+(0)$, $\nu'_-(0)$ appear at first order.

For simplicity, we shall now assume that the attachment lengths enjoy the $\theta \to (-\theta)$ symmetry. In this case the prefactors $\mathcal{S}_0$, $\mathcal{S}_1$, $\mathcal{S}_2$ in the dispersion relation vanish and the steps meander in phase.

We have seen that, in the two-sided case, the dispersion relation assumes a more complicated form, but the qualitative features of the instability are preserved. As the Ehrlich-Schwoebel barrier is the physical reason for the meandering instability, a change of the attachment lengths d_+ and d_- leads to a change of the length and time scales on which the instability takes place. Thus, the parameter

$$f_\mathrm{S} = \frac{d_-(0) - d_+(0)}{\ell + d_+(0) + d_-(0)}, \tag{4.31}$$

which describes the strength of the Ehrlich-Schwoebel effect, now enters into the critical wave number:

$$q_\mathrm{c} = \left(\frac{\Omega F \ell^2 f_\mathrm{S}}{2\Gamma(0)\,[D_\mathrm{S}\ell + D_\mathrm{L}(0)\,a]} \right)^{1/2}. \tag{4.32}$$

The most unstable mode is still the in-phase mode since we assumed that the anisotropies of the attachment lengths enjoy the $\theta \to (-\theta)$ symmetry.

Performing the multiscale analysis for the two-sided model (see App. B), we find the following evolution equation for the step meander:

$$\begin{aligned} \partial_t \zeta = -\partial_x \Bigg[& \frac{\Omega F}{2} \partial_x \zeta \frac{\ell_\perp^2 (d_- - d_+)}{d_+ + d_- + \ell_\perp} \\ & - \left(D_\mathrm{L}\, a + D_\mathrm{S} \frac{\ell^2 + \ell_\perp (d_+ + d_-)}{d_+ + d_- + \ell_\perp} \right) \frac{\partial_x (\Gamma \kappa)}{[1 + (\partial_x \zeta)^2]^{1/2}} \Bigg], \end{aligned} \tag{4.33}$$

where d_+, d_-, Γ, and D_L depend on the step orientation and $\ell_\perp$ is the effective interstep distance, defined by $\ell_\perp = \ell / [1 + (\partial_x \zeta)^2]^{1/2}$.

This evolution equation is formally equivalent to the evolution equation of the isotropic model. That is to say, there are no additional terms due to attachment anisotropy.

4.2.2. Modelling attachment anisotropy

As in the case of Γ and D_L anisotropy, we are interested in qualitative results and do not rely on any actual anisotropy form. Again, we introduce model anisotropies:

$$d_\pm(\theta) = d_{\pm,0}\, A_\pm(\theta) \tag{4.34}$$

with the anisotropy functions

$$A_\pm(\theta) = 1 + \epsilon_\pm \cos\left[4(\theta - \theta_\pm)\right], \tag{4.35}$$

which have the same characteristic shape as our model anisotropies for the stiffness and the line diffusion coefficient (see Fig. 4.1). The desired $\theta \rightarrow (-\theta)$ symmetry is obtained for $\theta_\pm = 0, \pi/4$.

4.2.3. Steady-state analysis

As in the one-sided case, the evolution equation (4.33) takes the form of a conservation law, $\partial_t \zeta = -\partial_x j$, and stationary solutions can be found from the condition $j = 0$.

With the help of the potential

$$V(m) = \frac{1}{f_\mathrm{S}} \int_{m_0}^{m} \frac{(\tilde{d}_- - \tilde{d}_+)\, m'\, \mathrm{d}m'}{(1-\tilde{\beta})\, f(m') + \tilde{\beta}\, g(m')}, \tag{4.36}$$

where $\tilde{d}_\pm = d_\pm/\ell$ are the reduced attachment lengths and

$$f(m') = \tilde{d}_+ + \tilde{d}_- + (1-m'^2)^{1/2}, \tag{4.37}$$
$$g(m') = 1 + (\tilde{d}_+ + \tilde{d}_-)(1-m'^2)^{1/2}, \tag{4.38}$$

we can write the wavelength of stationary solutions in the form:

$$\lambda_0 = \frac{\lambda_\mathrm{m}}{2\pi} \int_{-m_0}^{m_0} \frac{\mathrm{d}m}{\left[V(m_0) - V(m)\right]^{1/2}}. \tag{4.39}$$

Now the steady-state branch can be plotted for any given attachment anisotropy. In the following sections we shall concentrate on two simple special cases, which give rise to different coarsening scenarios.

4.2.4. Interrupted coarsening

Before we start our discussion of attachment anisotropy, it should be mentioned that the scenario of interrupted coarsening which was found for Γ, D_{L} anisotropy in case of an infinite Ehrlich-Schwoebel barrier survives in case of a finite barrier. There are only quantitative changes of the steady-state branch, e. g., the precise value of $\tilde{\lambda}$ and thus the wavelength of the meandering ripples depends on the values of both attachment lengths.

Now we want to concentrate on cases that involve only attachment anisotropy, which is a good starting point for surfaces where this anisotropy is dominant.

The first interesting example that we want to study is a surface, where attachment from the lower terrace is instantaneous ($d_+ = 0$) and where attachment from the upper terrace is governed by an anisotropic finite attachment length $d_-(\theta)$. Now the scenario depends on only two anisotropy parameters, the strength ϵ_- of the d_- anisotropy and its orientation $\theta_- \in \{0, \pi/4\}$.

A study of the steady-state branch gives the following result: If the Ehrlich-Schwoebel barrier is enhanced in the step train direction and reduced for step orientations along the $\pi/4$ direction (i. e., $\theta_- = 0$), stationary solutions above λ_{c} exist, regardless of whether the steps are stabilized by terrace or line diffusion. The steady-state branch is non-monotonic and assumes a local maximum $\tilde{\lambda}$, which behaves like

$$\frac{\tilde{\lambda}}{\lambda_{\mathrm{c}}} \sim \frac{1}{(1-\epsilon_-)^{1/4}} \quad \text{for} \quad \epsilon_- \to 1. \tag{4.40}$$

Numerical simulations of the evolution equation confirm that interrupted coarsening takes place (if $\tilde{\lambda} > \lambda_{\mathrm{m}}$) and that the final wavelength is approximately $\tilde{\lambda}$. These simulations also show that the asymptotic behaviour of the amplitude is not affected by attachment anisotropy; the $t^{1/2}$ law remains valid.

If, however, the Ehrlich-Schwoebel barrier is reduced in the step train direction ($\theta_- = \pi/4$), we do not find steady-state solutions above λ_{c}. From this we conclude that coarsening does not occur, which is supported by numerical integrations of the evolution equation.

4.2.5. Logarithmic coarsening

Now we turn to the second interesting case that we want to study in detail. It is known that on some metal surfaces [e. g., Cu(001)] the Ehrlich-Schwoebel barrier is inverted for certain step orientations [1]. In this case, adatoms attach to the step more easily if they approach it from the upper terrace.

In order to model this situation we assume isotropic but finite d_+ and anisotropic d_-. For definiteness we set $\tilde{d}_+ = 1$, $\epsilon_+ = 0$, $\theta_- = 0$ and just vary ϵ_- and $\tilde{d}_-$.

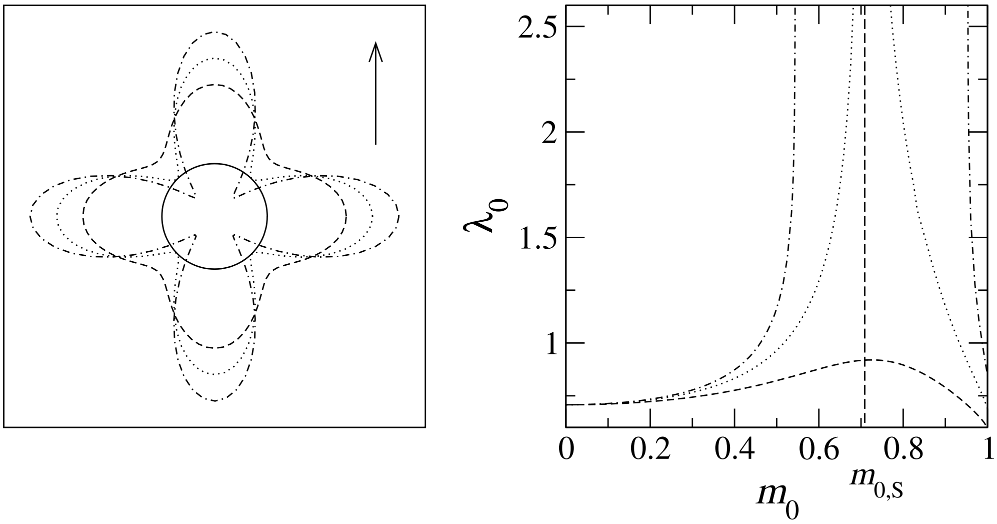

Figure 4.10.: Polar plot of the attachment lengths $\tilde{d}_+$ (solid line in the left panel), $\tilde{d}_-$ (broken lines in the left panel), and a plot of the corresponding steady-state branches (right panel). The arrow indicates the direction of the step train. The strength ϵ_- of the $\tilde{d}_-$ anisotropy is as follows: 0.25 (dashed line), 0.5 (dotted line), 0.75 (dot and dash line).

Fig. 4.10 shows the attachment lengths and the corresponding branches of steady-state solutions for different anisotropy strengths. The average attachment length for the upper side of the step is given by $\tilde{d}_{-,0} = 2$.

For $\epsilon_- = 0.25$ there is a positive Ehrlich-Schwoebel barrier for all step orientations and the steady-state branch reaches a maximum $\tilde{\lambda}$. The resulting coarsening dynamics does not differ qualitatively from the one that we have discussed in the previous section. For slightly larger ϵ_- we have $\tilde{\lambda} > \lambda_\mathrm{m}$ and there is interrupted coarsening.

In the case of $\epsilon = 0.5$ the Ehrlich-Schwoebel barrier vanishes for step orientations along $\theta = \pm\pi/4$ and the steady-state branch diverges at the corresponding finite slope $m_{0,\mathrm{S}}$.

For $\epsilon = 0.75$ there are step orientations for which the Ehrlich-Schwoebel barrier is inverted. The steady-state branch now consists of two parts, which are separated by a band of forbidden maximum slopes.

Fig. 4.11 gives results of a simulation with partially inverted Ehrlich-Schwoebel effect. The meander closely follows the diverging steady-state branch, whereby the maximum slope of the meander is limited by $m_{0,\mathrm{S}}$. Due to the occurrence of an upper bound for the slope, the development of the amplitude and of the wavelength are now coupled. The meander assumes a characteristic triangular shape.

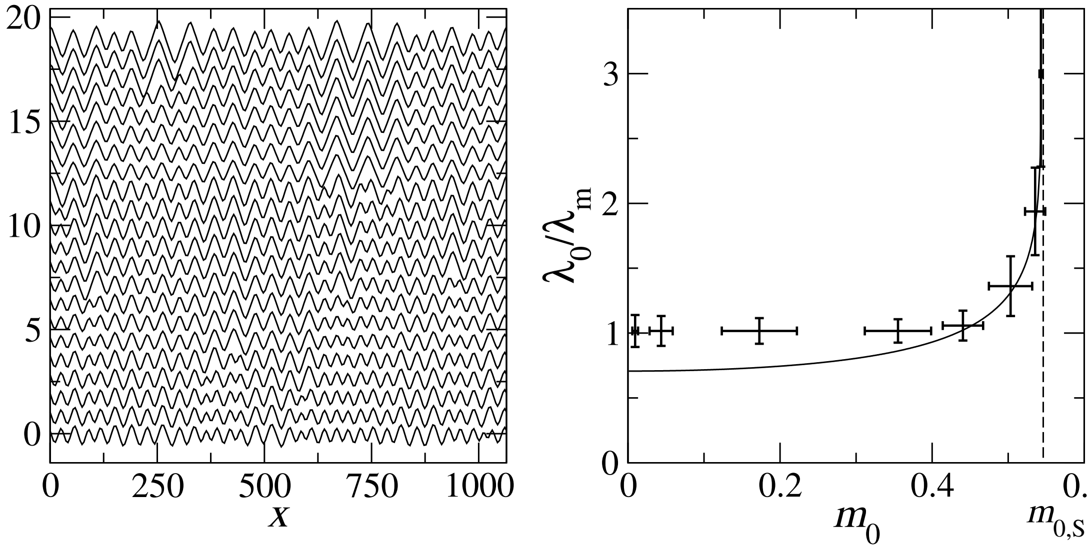

Figure 4.11.: Logarithmic coarsening in a system where the Ehrlich-Schwoebel barrier is partially inverted. The left panel shows the meander at different time, the right panel shows the steady-state branch (solid line) and the dynamics of the meander (crosses). Parameters are as follows: $\tilde{d}_+ = 1$, $\tilde{d}_- = 1.4$, $\epsilon_+ = 0$, and $\epsilon_- = 0.43$.

If we plot the slope $m = \partial_x\zeta/[1 + (\partial_x\zeta)^2]^{1/2}$ instead of the meander $\zeta(x, t)$, we obtain a graph, in which one can distinguish two domains: one where the curve is close to $m_{0,\mathrm{S}}$ and another where it is close to $-m_{0,\mathrm{S}}$. These domains are separated by domain walls, or kinks and anti-kinks (Fig. 4.12). In this picture, coarsening is related to the annihilation of kinks and anti-kinks.

Our problem is thus akin to the well-studied problem of phase separation, as described by the one-dimensional Cahn-Hilliard equation. In dimensionless units it can be written as

$$\partial_t p = \partial_{xx}\left[W'(p) - \partial_{xx}p\right], \tag{4.41}$$

where $p(x, t)$ is the order parameter and $W(p) = -p^2/2+p^4/4$ a symmetric double-well potential with minima at $p = \pm 1$, corresponding to the values of the order parameter for the pure phases [2].

Starting from a homogeneous state $p \equiv 0$, first a structure is formed that consists of small domains where the order parameter is 1 or -1. This structure undergoes a coarsening process, in which the typical domain size develops logarithmically with time [2, 59]. Coarsening occurs through the mutual attraction of kinks and anti-kinks, whose coupling decays exponentially with their distance.

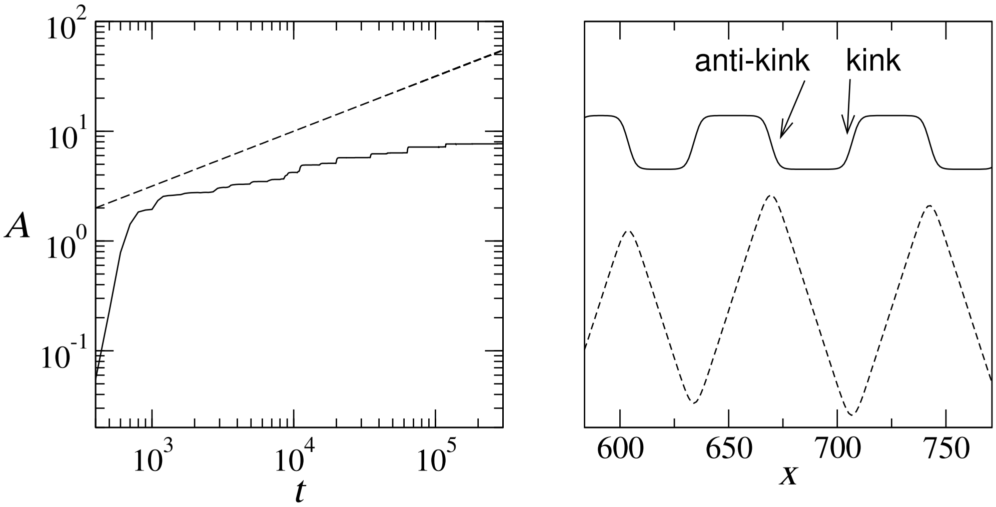

Figure 4.12.: Amplitude and meander in the scenario of logarithmic coarsening. The left panel shows the development of the amplitude (solid line). Its temporal evolution differs clearly from $t^{1/2}$ (dashed line). The right panel shows part of the meander (dashed line) and the corresponding slope (solid line). In the slope curve, two domains can be distinguished, which are separated by kinks and anti-kinks. Simulation parameters as in Fig. 4.11.

The Cahn-Hilliard equation (4.41) is variational since it can be written in the form

$$\partial_t p = \partial_{xx} \frac{\delta F[p]}{\delta p}, \tag{4.42}$$

where

$$F[p] = \int \mathrm{d}x \left[-\frac{p^2}{2} + \frac{p^4}{4} + \frac{(\partial_x p)^2}{2} \right] \tag{4.43}$$

is a Lyapunov functional. The evolution equation for the slope $h(x,t) \equiv \partial_x \zeta(x,t)$ of the step meander has the form

$$\partial_t h = \partial_{xx} \left[A(h) - B(h)\, \partial_{xx} m(h) \right]. \tag{4.44}$$

It is similar to the Cahn-Hilliard equation (4.41), but it introduces a non-constant mobility $B(h)$ in the stabilizing term. In general, it cannot be reduced to Eq. (4.41) and it is not variational. Nevertheless, for partially inverted Ehrlich-Schwoebel effect, our potential

$$V(m) = \int_{m_0}^{m} \frac{A(m')}{B(m')}\, \mathrm{d}m' \tag{4.45}$$

meets the requirements for the potential W in the Cahn-Hilliard equation: V is a symmetric double-well potential with minima at $m = \pm m_{0,\mathrm{S}}$, which also describes kink solutions with exponential coupling.

It is likely that the coarsening dynamics depends only on the set of steady states and not on the variational character of the equation. We can thus speculate that the dynamics of the step evolution equation is similar to the Cahn-Hilliard equation and that the exponential coupling of kinks and anti-kinks results in a coarsening process, where the average wavelength increases like $\ln t$.

We do not want to investigate this question more deeply, since logarithmic coarsening is a rather academic case. Logarithmic coarsening is known to break down in the presence of noise, where the kink positions undergo random fluctuations. Then, coarsening obeys a power-law behaviour [30].

Our numerical simulation (Fig. 4.12) cannot prove the occurrence of logarithmic coarsening, but it clearly shows that the growth of the meander amplitude is slower than $t^{1/2}$.

4.3. Terrace diffusion

In the first parts of this chapter we were concerned with the meandering dynamics of crystal steps under the influence of anisotropic step properties, such as anisotropic stiffness $\Gamma(\theta)$. It was found that for certain step orientations and strong enough anisotropy the dynamical scenario is changed: Instead of a fixed meandering wavelength, interrupted coarsening is observed. We now turn to the case where diffusion on the terraces is anisotropic. This is often due to surface reconstructions and dimer row formation, which gives rise to slow and fast diffusion along different directions (Fig. 4.13).

4.3.1. Modelling anisotropic terraces

On anisotropic terraces the diffusion law (2.2), $\mathbf{j} = -D\,\nabla c$, retains its form, but D is now a tensorial quantity. To make this difference clear, we now write

$$\mathbf{j} = -\underline{\underline{D}}\,\nabla c, \tag{4.46}$$

where the diffusion tensor is defined by

$$\underline{\underline{D}} = \begin{pmatrix} D_{11} & D_{12} \\ D_{12} & D_{22} \end{pmatrix}. \tag{4.47}$$

This tensor is symmetric and can thus be diagonalized: In its eigensystem (which is rotated by an angle ϕ_D with respect to our standard system), the tensor

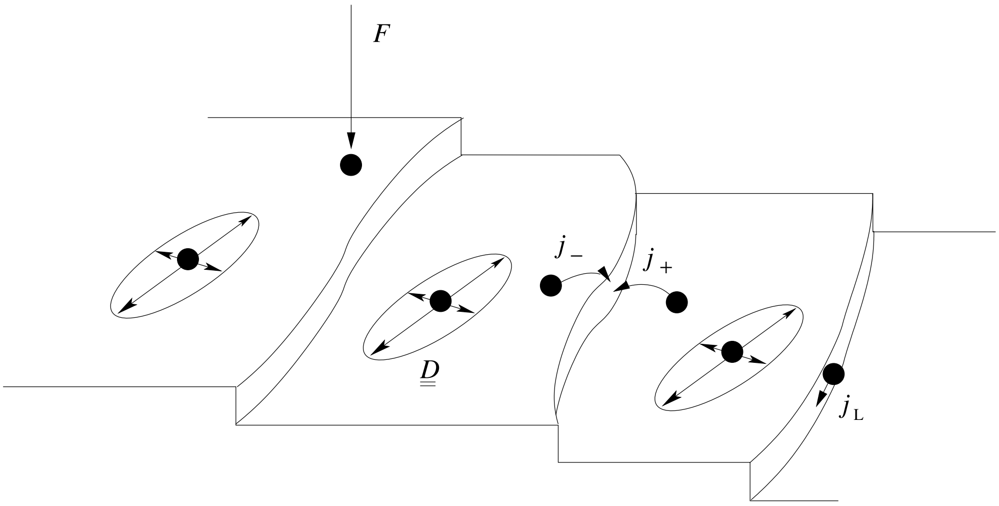

Figure 4.13.: Sketch of a vicinal surface with anisotropic terrace diffusion. The diffusion ellipsoid indicates the slow and fast directions of surface diffusion. For an explanation of the other processes, see Fig. 2.2.

reads

$$\underline{\underline{D}}' = D_0 \begin{pmatrix} \alpha^{1/2} & 0 \\ 0 & \alpha^{-1/2} \end{pmatrix} . \tag{4.48}$$

For convenience we have introduced $D_0 = [D_{11}\, D_{22} - D_{12}^2]^{1/2}$. The parameter α measures the ratio of the diffusion coefficients along the eigendirections.

4.3.2. Geometrical mapping

In principle it is now possible to adapt the calculation from Sect. 3.2 to obtain the step evolution equation for anisotropic terrace diffusion. There is a different approach, however, that saves us from re-doing a lengthy calculation and that may also be applicable to other problems.

In App. D we show that step meandering on anisotropic terraces can be mapped to a problem where diffusion is isotropic, if one writes the problem in suitable coordinates and performs a change of the metrics. The only side-effect is a modification of the step properties Γ, D_{L}, and $\nu_\pm$ along with some other model parameters. But the equations assume their original form with scalar D so that we can directly apply the analysis from the previous sections.

So far we have used Cartesian coordinates (x, y). The new coordinates $(\bar{x}, \bar{y})$, which are not to be confused with the eigensystem of the diffusion tensor, are given by the affine transformation

$$\bar{x} = x - \frac{D_{12}}{D_{22}}\, y, \tag{4.49}$$

$$\bar{y} = \frac{D_0}{D_{22}}\, y. \tag{4.50}$$

We also introduce the new metrics $\bar{\mathbf{e}}_i \cdot \bar{\mathbf{e}}_j = \delta_{ij}$. This is necessary in order to obtain the desired formal equivalence of the transformed model with the isotropic model.

In the transformed system, the diffusion equation takes the form

$$\partial_t c = \bar{D}_0\, \bar{\nabla}^2 c + F \tag{4.51}$$

with $\bar{D}_0 = D_0^2 / D_{22}$ and the gradient operator $\bar{\nabla} \equiv \bar{\mathbf{e}}_{\bar{x}}\, \partial_{\bar{x}} + \bar{\mathbf{e}}_{\bar{y}}\, \partial_{\bar{y}}$.

The boundary conditions read

$$\bar{D}_0\, \bar{\mathbf{n}} \cdot \bar{\nabla} c|_+ = \bar{\nu}_+\, (c - c_{\mathrm{eq}})|_+, \tag{4.52}$$

$$-\bar{D}_0\, \bar{\mathbf{n}} \cdot \bar{\nabla} c|_- = \bar{\nu}_-\, (c - c_{\mathrm{eq}})|_-, \tag{4.53}$$

where $\bar{\mathbf{n}}$ is the unit normal to the step in the transformed system.

The step properties of the transformed model are anisotropic even if the corresponding physical quantities do not depend on the step orientation. After introducing the local angle along the transformed step,

$$\bar{\theta} = \arctan\left(\frac{D_0\, \tan\theta}{D_{22} - D_{12}\, \tan\theta} \right), \tag{4.54}$$

we can write the new step properties as

$$\bar{\Gamma}(\bar{\theta}) = \frac{D_{22}}{D_0}\, f(\bar{\theta})^3\, \Gamma, \tag{4.55}$$

$$\bar{D}_{\mathrm{L}}(\bar{\theta}) = \frac{D_0}{D_{22}}\, f(\bar{\theta})\, D_{\mathrm{L}}, \tag{4.56}$$

$$\bar{\nu}_\pm(\bar{\theta}) = \frac{D_0}{D_{22}} \frac{1}{f(\bar{\theta})}\, \nu_\pm \tag{4.57}$$

with the common function

$$f(\bar{\theta}) = D_0 [(D_0\, \cos\bar{\theta} + D_{12}\, \sin\bar{\theta})^2 + D_{22}^2\, \sin^2\bar{\theta}]^{-1/2}. \tag{4.58}$$

In Fig. 4.14, we show the resulting effective anisotropies $\bar{\Gamma}(\bar{\theta})$ and $\bar{D}_{\mathrm{L}}(\bar{\theta})$ for steps with constant Γ and D_{L}. It can be seen that these anisotropies have a twofold symmetry instead of the fourfold symmetry that we assumed for most of our discussion on anisotropic steps.

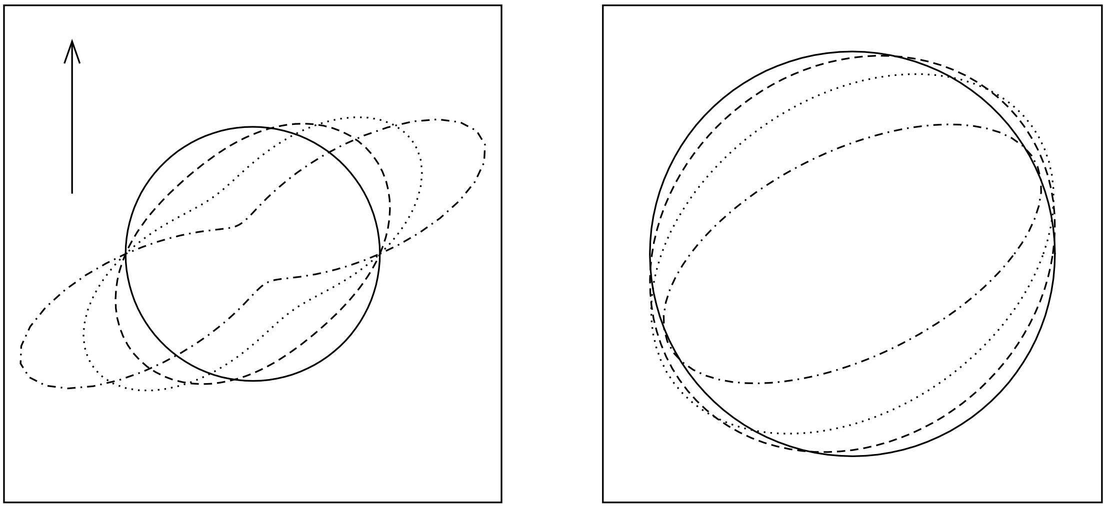

Figure 4.14.: Polar plot of the effective anisotropies $\bar{\Gamma}(\bar{\theta})$ (left panel) and $\bar{D}_{\mathrm{L}}(\bar{\theta})$ (right panel) for $\phi_{\mathrm{D}} = \pi/4$. The strengths of the anisotropies are as follows: $\alpha = 1$ (solid line), $\alpha = 0.75$ (dashed line), $\alpha = 0.5$ (dotted line), and $\alpha = 0.25$ (dot and dash line). The arrow points in the direction of the step train.

If the original quantities Γ, D_{L}, and $\nu_{\pm}$ are themselves anisotropic, they have to be evaluated at the angle θ corresponding to $\bar{\theta}$ via Eq. (4.54). The effective anisotropies then have a more complicated form, as they mix the influence of different physical anisotropies.

With the given transformation (4.55) of the line stiffness, the Gibbs-Thomson law retains its form and the equilibrium concentration can be written as

$$c_{\mathrm{eq}} = c_{\mathrm{eq}}^{0}[1 + \bar{\Gamma}(\bar{\theta})\,\bar{\kappa}], \tag{4.59}$$

where $\bar{\kappa}$ is the curvature in the transformed system.

Finally, the transformed normal velocity of the steps is given by

$$\bar{v}_n = \Omega \bar{D}_0[\bar{\mathbf{n}} \cdot \bar{\nabla} c|_+ - \bar{\mathbf{n}} \cdot \bar{\nabla} c|_-] + a\,\partial_{\bar{s}}[\bar{D}_{\mathrm{L}}\,\partial_{\bar{s}}(\bar{\Gamma}\bar{\kappa})], \tag{4.60}$$

where $\bar{s}$ is the arc length in the transformed system.

The moving boundary problem is now fully specified. In principle all one has to do now is to plug the transformed model parameters into the solutions that have been obtained for isotropic diffusion and to map the results back to Cartesian coordinates.

4.3.3. Linear instability

First we have to review the linear stability problem. For the one-sided model, the dispersion relation takes the form:

$$\begin{aligned}\mathrm{Re}(\mathrm{i}\omega) &= \frac{\Omega F}{\cosh q\bar{\ell}}\left[q\bar{\ell}\sinh q\bar{\ell} - \cosh q\bar{\ell} + \cos\bar{\phi}\right] \\ &\quad - \frac{\bar{\Gamma}(0)\,q^2}{\cosh q\bar{\ell}}\left[q\bar{D}_\mathrm{S}\sinh q\bar{\ell} + q^2 a\bar{D}_\mathrm{L}(0)\cosh q\bar{\ell}\right], \qquad (4.61)\\ \mathrm{Im}(\mathrm{i}\omega) &= \frac{\Omega F}{\cosh q\bar{\ell}}\sin\bar{\phi}. \qquad (4.62)\end{aligned}$$

Here, $\bar{\phi}$ is the phase shift between neighbouring steps in the transformed system, $\bar{\ell} = D_0/D_{22}\,\ell$ is the effective interstep distance, and $\bar{D}_\mathrm{S} = c^0_\mathrm{eq}\Omega\bar{D}_0$.

The maximum growth rate is obtained for $\bar{\phi} = 0$, i. e., for the in-phase mode in the transformed system. This corresponds to a phase shift in the Cartesian system if the diffusion tensor is not diagonal:

$$\phi = \bar{\phi} - \frac{D_{12}}{D_{22}}q\ell. \qquad (4.63)$$

This is the first important difference as compared to isotropic terrace diffusion, where steps usually meander in phase. An out-of-phase meander gives rise to tilted meandering ripples. The ripples then form an angle of

$$\phi_\mathrm{R} = \arctan(D_{12}/D_{22}) \qquad (4.64)$$

with respect to the step train (Fig. 4.15).

Another important result concerns the wavelength of the most unstable mode. In the long-wave limit it can be written as

$$\lambda_\mathrm{m} = 4\pi\left[\frac{\Gamma(D_\mathrm{S}\bar{\ell} + D_\mathrm{L}a)}{\Omega F\bar{\ell}^2}\right]^{1/2}. \qquad (4.65)$$

Comparing this result to the wavelength on an isotropic terrace [Eq. (3.8)], one realizes that at this point the anisotropy of terrace diffusion only enters into the interstep distance. If diffusion along the y axis is faster, then according to $\bar{\ell} = D_0/D_{22}\,\ell$, the effective interstep distance is smaller than the physical distance, otherwise it is larger.

Furthermore, we can conclude that the ripple wavelength λ_m is larger as compared to an isotropic system with the same mean diffusion coefficient D_0 if the angle between the fastest direction and the step train direction is smaller than a critical angle θ_c. For small anisotropy, $\theta_\mathrm{c} = \pi/4$; as the anisotropy gets larger, $\theta_\mathrm{c} \to \pi/2$. Strong anisotropy has a stabilizing effect, almost regardless of its orientation.

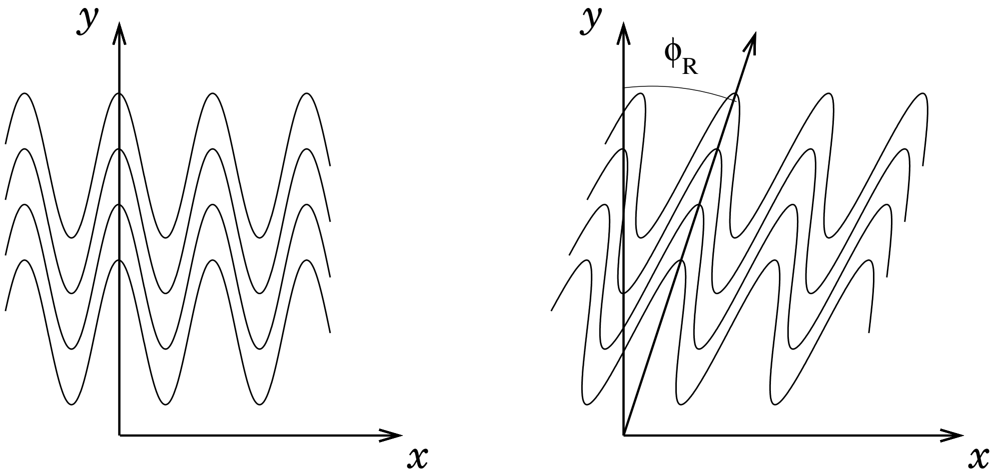

Figure 4.15.: Meandering on a vicinal surface. Left panel: isotropic terrace diffusion; right panel: anisotropic terrace diffusion. Anisotropic terrace diffusion may lead to tilted meandering ripples, where the ripple forms an angle ϕ_R with respect to the step train.

In an experiment one might be less interested in the wavelength λ_m and more in the ripple width λ_R, which is observed directly. These quantities differ if the ripple is tilted:

$$\lambda_\mathrm{R} = \lambda_\mathrm{m} \cos\phi_\mathrm{R}. \tag{4.66}$$

Here we have assumed, of course, that the final pattern width is set by linear instability. As we already know, the pattern width can change through coarsening. Nevertheless, in Fig. 4.16 we show the ripple width according to the linear stability analysis as a function of the orientation of the anisotropy.

4.3.4. Interrupted coarsening

The evolution equation for the transformed step meander $\zeta(\bar{x}, t)$ becomes:

$$\begin{aligned}\partial_t \zeta = -\partial_{\bar{x}} \Bigg[& \frac{\Omega F \bar{\ell}^2}{2} \frac{\partial_{\bar{x}}\zeta}{1 + (\partial_{\bar{x}}\zeta)^2} \\ & - \left(\frac{\bar{D}_\mathrm{S} \bar{\ell}}{1 + (\partial_{\bar{x}}\zeta)^2} + \frac{\bar{D}_\mathrm{L}(\bar{\theta})\, a}{[1 + (\partial_{\bar{x}}\zeta)^2]^{1/2}} \right) \partial_{\bar{x}} [\bar{\Gamma}(\bar{\theta})\, \bar{\kappa}] \Bigg].\end{aligned} \tag{4.67}$$

It is equivalent to the equation for the isotropic meander, except for the substitution of the transformed model parameters and effective anisotropies.

At this point we want to assume isotropic steps and concentrate on the effect of anisotropic terrace diffusion. Now our analysis will proceed along the same

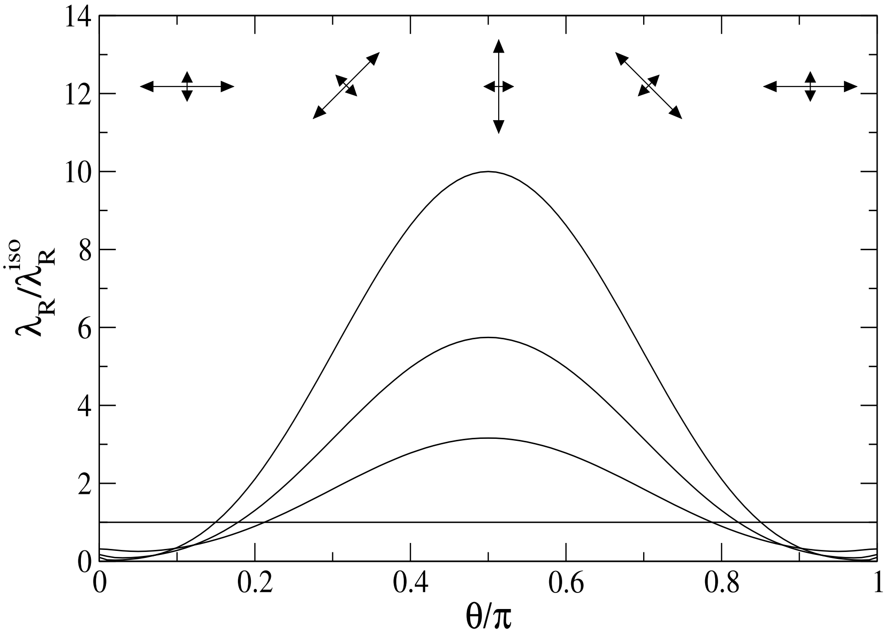

Figure 4.16.: The width of meandering ripples corresponding to the most unstable mode as a function of the orientation of the anisotropy for $\alpha = 1$, 10, 30, and 100 (from lower to upper curve).

lines as the one for anisotropic step properties. We shall first discuss the steady-state branches for the effective anisotropies $\bar{\Gamma}(\bar{\theta})$, $\bar{D}_{\mathrm{L}}(\bar{\theta})$ to predict the coarsening scenario and then use numerical simulations of the evolution equation to check our prediction.

For simplicity we concentrate on cases where the principal axes of the diffusion tensor are aligned with the average step direction and the direction of the step train. Then, the diffusion tensor reads:

$$\underline{\underline{D}} = D_0 \begin{pmatrix} \alpha^{1/2} & 0 \\ 0 & \alpha^{-1/2} \end{pmatrix} . \tag{4.68}$$

If $\alpha < 1$, that is, diffusion is faster in the y direction, we do not find steady-state solutions with wavelength $\lambda_0 > \lambda_{\mathrm{c}}$. According to our previous argument, coarsening should not take place. This is indeed confirmed by numerical simulations. These simulations also confirm that the known asymptotic behaviour, where the amplitude of the meander behaves like $t^{1/2}$, is not affected by terrace anisotropy.

For the case $\alpha > 1$, where diffusion is faster in the x direction, we find stationary solutions above λ_{c}, *if* there is line diffusion along the steps.

Fig. 4.17 shows the steady-state branch of the evolution equation and the corresponding development of the meander according to a numerical simulation. Terrace diffusion anisotropy gives rise to a steady-state branch which reaches its

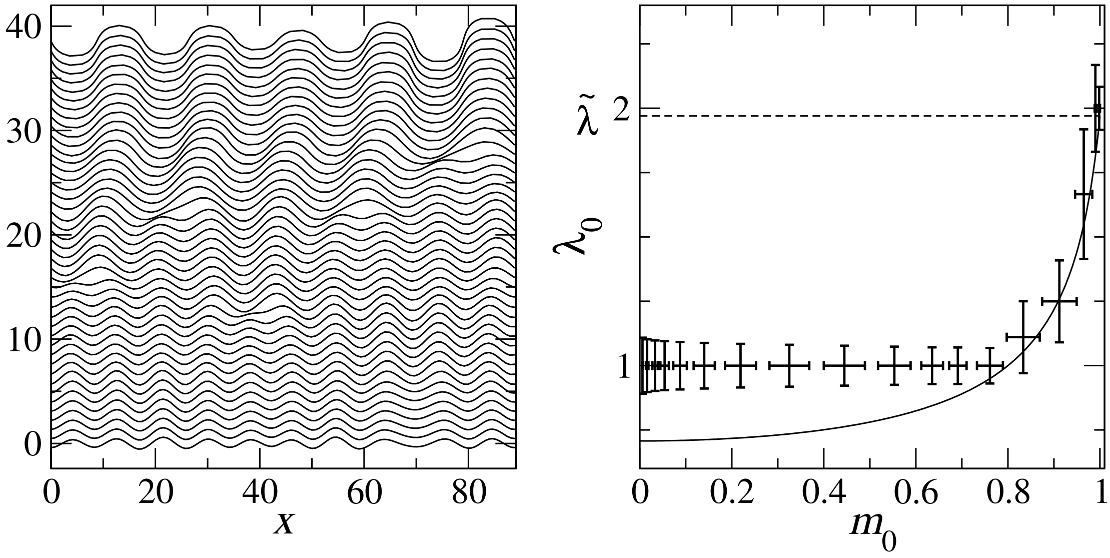

Figure 4.17.: Interrupted coarsening in the presence of terrace anisotropy. The left panel shows snapshots of the meander at different times. The right panel displays the dynamics of the system in the λ_0-m_0 plane. The solid line depicts the steady-state branch of the evolution equation; the crosses refer to the evolution of the meander in the numerical simulation. Error bars indicate the standard deviation of λ_0 and m_0. Parameters are $\alpha = 11$ and $D_\mathrm{S} = 0$ (line diffusion limit).

maximum $\tilde{\lambda}$ at the interval boundary $m_0 = 1$. In principle, coarsening might now take infinite time as $m_0 = 1$ corresponds to infinite amplitude. But practically, the scenario of interrupted coarsening does not change in finite systems. Correspondingly, in the numerical simulation, coarsening stops when the meander wavelength is larger than $\tilde{\lambda}$. As expected from the analysis of the similar problem of Γ, D_L anisotropy, the amplitude keeps to develop and increases asymptotically like $t^{1/2}$.

It is interesting to see how $\tilde{\lambda}$ behaves with the anisotropy strength α. An asymptotic analysis of the λ_0 integral (4.11) for $\alpha \gg 1$ and $D_\mathrm{S} = 0$ (line diffusion limit) provides us with

$$\frac{\tilde{\lambda}}{\lambda_\mathrm{c}} \sim \alpha^{1/2}. \tag{4.69}$$

4.3.5. Discussion

Surface diffusion can be highly anisotropic. On Si(001), for example, diffusion along dimer rows may be 1,000 times faster than diffusion across dimer rows [35]. As in the case of Si(001), high terrace diffusion anisotropy is mostly due to surface reconstructions, and for many crystals, the direction of dimer rows alternates between terraces, so that two types of terraces (A and B) must be distinguished.

A generalization of the geometrical mapping to tackle problems with alternating terraces seems to be of little benefit. One would have to deal not only with two types of steps but also with two new coordinate systems, and a link with existing theories might be hard to establish. There are, however, situations where the geometrical mapping can be applied directly. On reconstructed Si(100) surfaces at growth temperatures around 775 K, biatomic steps are formed, so that one type of terrace predominates [58]. Furthermore, pure step flow growth due to the movement of the biatomic steps has been observed [58].

Apart from step meandering there are other interesting questions, where the mapping can be employed directly. One concerns submonolayer epitaxy and the formation of denuded zones.

In submonolayer epitaxy only a small amount of matter is deposited on a (singular) surface. This leads to the formation of small islands and large denuded zones, where the substrate is not covered. The areal densities of islands and also the linear densities along fast and slow directions have been measured experimentally [35]. From these results one can compute the aspect ratio $W_{\text{fast}}/W_{\text{slow}}$ (typical width in the fast diffusion direction vs. width in the slow direction) of denuded zones.

There is some disagreement between recent computer simulations, which yield a fixed aspect ratio $(D_{\text{fast}}/D_{\text{slow}})^{1/2}$ and some older dimensional arguments, which predict exponents ranging from 1/6 to 1/4, depending on the strength of the anisotropy [16].

Starting from our geometrical mapping, we can easily derive an argument in favour of the more recent study. In the transformed system, diffusion is isotropic and the denuded zones should have an aspect ratio of 1/1 if we assume that the islands are sufficiently small. Going back to the physical frame, we obtain an aspect ratio of $(D_{\text{fast}}/D_{\text{slow}})^{1/2}$, which is in agreement with the results from Ref. [16].

Another application of the mapping might be the study of step fluctuations, which is useful for the experimental determination of step properties [25]. With the help of the geometrical mapping it is straightforward to incorporate the effects of anisotropic terrace diffusion into existing models.

5. Conclusion

We have described a new dynamical scenario for meandering crystal steps. On surfaces where step meandering is due to the Ehrlich-Schwoebel effect, the wavelength of the meandering pattern may not correspond to the most unstable mode from linear instability. Instead, the nonlinear dynamics is characterized by a process of *interrupted coarsening*, which selects a wavelength that is determined by the precise form and orientation of relevant crystalline anisotropies.

This wavelength selection mechanism must be taken into account when confronting a step-flow model with experimental data. We have proven the scenario of interrupted coarsening by numerically integrating a step evolution equation, whose correctness has been assessed in the long-wave limit. Furthermore, we have established a link between the coarsening dynamics and the steady-state solutions of the step evolution equation. From this starting point we have derived formulas that can be used to determine the final pattern wavelength from the actual form of the anisotropies.

In summary, there are three dynamical scenarios: (i) No coarsening; the pattern wavelength is set by linear instability and corresponds to the wavelength of the most unstable mode. (ii) Interrupted coarsening; the wavelength is fixed at a later stage of the instability and depends on crystal anisotropy. (iii) Endless coarsening, where the pattern wavelength increases indefinitely.

Our method deals with anisotropic step properties (stiffness, line diffusion, and attachment kinetics). With the help of a geometrical mapping, a model with anisotropic terrace diffusion can be reduced to a model with isotropic diffusion and modified step properties. Terrace diffusion anisotropy can thus be treated within the same framework. In addition to that, the geometrical mapping is useful in other contexts, where terrace diffusion anisotropy is to be incorporated into existing models.

A. Linear stability analysis

On a perfect vicinal surface the steps are straight and the interstep distance ℓ is constant. In ideal step flow growth, the steps remain straight and their distance does not change. Thus, all steps move at the same velocity, which by mass conservation is found to be $V_0 = \Omega F \ell$.

In this appendix we perform the linear stability analysis of a step train during growth with respect to step meandering.

A.1. Ideal step flow

We first seek the full solution of the model equations for the unperturbed growth of equidistant straight steps. The dynamics of the surface is described by the quasistatic diffusion equation

$$0 = D\,\nabla^2 c + F \tag{A.1}$$

with the boundary conditions

$$D\,\partial_n c|_+ = \nu_+\,[c - c_{\mathrm{eq}}]|_+, \tag{A.2}$$

$$-D\,\partial_n c|_- = \nu_-\,[c - c_{\mathrm{eq}}]|_- \tag{A.3}$$

and the step normal velocity

$$v_n = \Omega D\,[\partial_n c|_+ - \partial_n c|_-] + a\,\partial_s[D_{\mathrm{L}}\,\partial_s(\Gamma\kappa)]. \tag{A.4}$$

The equilibrium concentration at the steps is given by

$$c_{\mathrm{eq}} = c^0_{\mathrm{eq}}\,(1 + \Gamma\kappa). \tag{A.5}$$

As the adatom concentration is usually discontinuous at the steps, we introduce new functions $c_m(x, y, t)$ which are valid on the mth terrace only and write the global concentration field as

$$c(x, y, t) = \sum_{m=-\infty}^{+\infty} c_m(x, y, t)\,\Theta(y - y_m(x, t))\,\Theta(y_{m+1}(x, t) - y), \tag{A.6}$$

where $\Theta(y)$ is the Heaviside function and $y_m(x, t)$ the position of the mth step. In a uniform step train, the position of the mth step is given by $y_m(x, t) = y^0_m(t)$

with $y^0_m(t) = m\ell + V_0\, t$, which we shall use later on to refer to the position of the unperturbed steps.

In ideal step flow the adatom concentration is uniform in the x direction and the diffusion equation on the mth terrace reduces to

$$D\,\partial_{yy} c^0_m + F = 0. \tag{A.7}$$

It has the general solution

$$c^0_m = -\frac{F}{2D}(y - y^0_m)^2 + A^0_m\,(y - y^0_m) + B^0_m \tag{A.8}$$

with the integration constants A^0_m and B^0_m. The boundary conditions dictate

$$A^0_m\, D = \nu_+\,(B^0_m - c^0_{\text{eq}}), \tag{A.9}$$

$$F\ell - A^0_m\, D = \nu_-\,(-F\ell^2/2D + A^0_m\ell + B^0_m - c^0_{\text{eq}}), \tag{A.10}$$

whereby the integration constants are obtained as

$$A^0_m = \frac{\nu_+ F\ell + \nu_+\nu_- F\ell^2/2D}{(\nu_+ + \nu_-)\,D + \nu_+\nu_-\ell}, \tag{A.11}$$

$$B^0_m = c^0_{\text{eq}} + \frac{DF\ell + \nu_- F\ell^2/2}{(\nu_+ + \nu_-)\,D + \nu_+\nu_-\ell}. \tag{A.12}$$

The equation for the normal velocity v_n gives the expected velocity of the uniform step train: $V_0 = \Omega F\ell$.

A.2. Linear perturbation

We now perturb the steps with a small-amplitude meander $\varepsilon\,\zeta_m$, so that the position of the mth step is given by

$$y_m(x,t) = y^0_m(t) + \varepsilon\,\zeta_m(x,t). \tag{A.13}$$

The meander $\zeta_m(x,t)$ is written in the form of a Fourier mode:

$$\zeta_m = e^{i(m\phi + qx + \omega t)}, \tag{A.14}$$

where ϕ is the phase shift between neighbouring steps, q the wave number, and $i\omega$ the complex growth rate of the perturbation [19].

As the step properties depend on the local orientation of the step, we have to expand them about the orientation $\theta = 0$ of the unperturbed step. The linearized stiffness, for example, reads

$$\Gamma(\theta_m) = \Gamma(0) + \varepsilon\,\zeta_m\,\Gamma'(0). \tag{A.15}$$

There are analogous expressions for the line diffusion coefficient D_{L} and for the kinetic coefficients ν_+ and ν_-.

The step perturbation results in a perturbed concentration field, which takes the form [19]:

$$c_m(x, y, t) = c_m^0(y) + \varepsilon\, \zeta_m(x, t)\, c_m^1(y). \tag{A.16}$$

Inserting the ansatz (A.16) for the perturbed concentration field into the diffusion equation, we obtain

$$0 = \underbrace{D\, \nabla^2 c_m^0(y) + F}_{=0} + \varepsilon\, D\, \nabla^2[\zeta_m(x, t)\, c_m^1(y)]. \tag{A.17}$$

With $\partial_{xx}\zeta_m = -q^2\, \zeta_m$ we find the equation for $c_m^1(y)$,

$$\partial_{yy} c_m^1(y) - q^2\, c_m^1(y) = 0, \tag{A.18}$$

which has the general solution

$$c_m^1(y) = A_m^1\, e^{q\,(y - y_m^0)} + B_m^1\, e^{-q\,(y - y_m^0)}. \tag{A.19}$$

In order to determine A_m^1 and B_m^1 we have to evaluate the kinetic conditions at the perturbed steps. At the ascending step we have

$$D\, \partial_n c_m|_{y=y_m} = \nu_+\, (c_m - c_{\mathrm{eq},m})|_{y=y_m}. \tag{A.20}$$

To linear order the normal derivative on the left-hand side of Eq. (A.20) can be expressed as

$$\partial_n c_m = (\partial_y - \varepsilon\, \partial_x\zeta_m\, \partial_x)\, c_m. \tag{A.21}$$

With the linearized curvature $\kappa_m = -\partial_{xx}\zeta_m$ we find the expansion of the equilibrium concentration on the right-hand side of Eq. (A.20):

$$c_{\mathrm{eq},m} = c_{\mathrm{eq}}^0\, (1 - \varepsilon\, \Gamma\, \partial_{xx}\zeta_m). \tag{A.22}$$

Finally, we expand the concentration field about y_m^0,

$$c_m|_{y=y_m} = c_m^0(y_m^0) + \varepsilon\, \zeta_m\, \partial_y c_m^0(y_m^0) + \varepsilon\, \zeta_m\, c_m^1(y_m^0) + O(\varepsilon^2), \tag{A.23}$$

which is also inserted into Eq. (A.20). As expected, we find that the boundary condition is satisfied at $O(1)$. At $O(\varepsilon)$ we get the following relation:

$$\partial_y C_m(y_m^0) = k_+(0)\, \left[C_m(y_m^0) - c_{\mathrm{eq}}^0\, \Gamma\, q^2\right] + iq\, k_+'(0)\, \left[c_m^0(y_m^0) - c_{\mathrm{eq}}^0\right]. \tag{A.24}$$

Here we have used the abbreviations $C_m = \partial_y c_m^0 + c_m^1$ and $k_+ = \nu_+/D$. Inserting the general solutions of the concentration field at zeroth and first order, we find the first condition for A_m^1 and B_m^1:

$$[q - k_+(0)]\, A_m^1 - [q + k_+(0)]\, B_m^1 = \alpha \tag{A.25}$$

with

$$\alpha = \frac{F}{D} + k_+(0)\left[A_m^0 - c_{\mathrm{eq}}^0 \Gamma q^2\right] + iq\, k_+'(0)\left[B_m^0 - c_{\mathrm{eq}}^0\right]. \tag{A.26}$$

The kinetic condition at the descending step reads:

$$-D\,\partial_n c_m|_{y=y_{m+1}} = \nu_-\left(c_m - c_{\mathrm{eq},m+1}\right)|_{y=y_{m+1}}. \tag{A.27}$$

Expanding this equation about y_{m+1}^0, we obtain at $O(\epsilon)$:

$$\begin{aligned}\partial_y C_m^*(y_{m+1}^0) = -k_-(0)\, &\left[C_m^*(y_{m+1}^0) - c_{\mathrm{eq}}^0\, \Gamma\, q^2\, e^{i\phi}\right] \\ &- iq\, k_-'(0)\, e^{i\phi}\, \left[c_m^0(y_{m+1}^0) - c_{\mathrm{eq}}^0\right]\end{aligned} \tag{A.28}$$

with $C_m^* = e^{i\phi}\,\partial_y c_m^0 + c_m^1$ and $k_- = \nu_-/D$. Inserting the general solutions of the diffusion equation, we find the second condition for A_m^1 and B_m^1:

$$[q + k_-(0)]\, e^{q\ell}\, A_m^1 - [q - k_-(0)]\, e^{-q\ell}\, B_m^1 = e^{i\phi}\beta \tag{A.29}$$

with

$$\begin{aligned}\beta = \frac{F}{D} &- k_-(0)\left[A_m^0 - F\ell/D - c_{\mathrm{eq}}^0 \Gamma q^2\right] \\ &- iq\, k_-'(0)\left[-F\ell^2/2D + A_m^0 \ell + B_m^0 - c_{\mathrm{eq}}^0\right].\end{aligned} \tag{A.30}$$

The solution of the linear system (A.25, A.29) gives the sought-after integration constants:

$$A_m^1 = \frac{1}{Q}\left\{[q + k_+(0)]\, e^{i\phi}\, \beta - [q - k_-(0)]\, e^{-q\ell}\, \alpha\right\}, \tag{A.31}$$

$$B_m^1 = \frac{1}{Q}\left\{[q - k_+(0)]\, e^{i\phi}\, \beta - [q + k_-(0)]\, e^{q\ell}\, \alpha\right\} \tag{A.32}$$

with

$$Q = 2\left[q^2 + k_+(0)\, k_-(0)\right]\sinh q\ell + 2q\left[k_+(0) + k_-(0)\right]\cosh q\ell. \tag{A.33}$$

A.3. Dispersion relation

Now that we have obtained the perturbed concentration field, we can use the mass balance at the steps to calculate the dispersion relation.

At $O(\epsilon)$, the contributions to the step normal velocity are as follows. The current from the lower terrace is

$$j_+^1 = D\left[-F/D + q\,A_m^1 - q\,B_m^1\right]\zeta_m \tag{A.34}$$

and the current from the upper terrace is

$$j_-^1 = -D\left[-F/D + q\,e^{-i\phi}\,e^{q\ell}\,A_m^1 - q\,e^{-i\phi}\,e^{-q\ell}\,B_m^1\right]\zeta_m. \tag{A.35}$$

We also have the divergence of the current along the step, which is given by

$$\partial_s j_{\mathrm{L}} = \varepsilon\,q^4\,\Gamma(0)\,D_L(0)\,\zeta_m. \tag{A.36}$$

Summing up the three contributions to the step normal velocity and observing that $\varepsilon\,\partial_t\zeta_m = \varepsilon\,i\omega\zeta_m = v_n - V_0$ at linear order, we first get

$$i\omega = \Omega D\left[(A^1 - B^1) - e^{-i\phi}\left(e^{q\ell}A^1 - e^{-q\ell}B^1\right)\right]q - a\,D_{\mathrm{L}}(0)\,\Gamma(0)\,q^4. \tag{A.37}$$

Plugging in the coefficients and simplifying, we finally obtain

$$\begin{aligned}\mathrm{Re}(i\omega) = \Omega F\frac{q}{\mathcal{D}}\frac{d_- - d_+}{\ell + d_+ + d_-}\Big[&(d_- + d_+)(q\ell\,\sinh q\ell - \cosh q\ell + \cos\phi)\\ &+ \frac{\ell}{2}q\ell\,\left(\sinh q\ell + \mathcal{S}_0\sin\phi\right)\Big]\\ &- \Gamma q^2\Big[D_{\mathrm{S}}\frac{q}{\mathcal{D}}\{2(\cosh q\ell - \cos\phi)\\ &+ q\,(d_+ + d_-)\,\sinh q\ell\} + aD_{\mathrm{L}}\,q^2\Big],\end{aligned} \tag{A.38}$$

$$\begin{aligned}\mathrm{Im}(i\omega) = \Omega F\frac{q}{\mathcal{D}}\Big[&(\ell + d_+ + d_-)\,\sin\phi\\ &+ \frac{1}{2}q\ell\,\{\mathcal{S}_1\,(\cos\phi - \cosh q\ell) - \mathcal{S}_2\,q\ell\,\sinh q\ell\}\Big].\end{aligned} \tag{A.39}$$

Here we have introduced the abbreviations

$$\mathcal{D} = (d_+ + d_-)\,q\,\cosh q\ell + \left(d_+d_-q^2 + 1\right)\,\sinh q\ell \tag{A.40}$$

and

$$\mathcal{S}_0 = \frac{(d'_+ - d'_-)\,\ell + 2\,(d'_+d_- - d'_-d_+)}{(d_- - d_+)\,\ell}, \tag{A.41}$$

$$\mathcal{S}_1 = \frac{d'_+\,(\ell + 2d_-) + d'_-\,(\ell + 2d_+)}{\ell + d_+ + d_-}, \tag{A.42}$$

$$\mathcal{S}_2 = \frac{d'_+d_-\,(1 + 2d_-/\ell) + d'_-d_+\,(1 + 2d_+/\ell)}{\ell + d_+ + d_-}. \tag{A.43}$$

For brevity we have dropped the arguments of the model parameters. All of them have to be evaluated at the orientation of the unperturbed step ($\theta = 0$).

As compared to the dispersion relation of the isotropic model, the anisotropic relationship has some new terms, which are due to attachment anisotropy. They are recognized by the prefactors $\mathcal{S}_0$, $\mathcal{S}_1$, and $\mathcal{S}_2$. Attachment anisotropy is the only anisotropy that contributes new terms to the dispersion relation. The emergence of these new terms is discussed in Sect. 4.2.1.

B. Multiscale analysis

In this appendix we derive the evolution equation for steps which meander in phase. Our calculation closely follows Ref. [20], but we take special care that anisotropy effects are taken into account.

B.1. Asymptotic expansion

The first step is the identification of a small parameter. We use

$$\epsilon = 2(q_c \ell)^2, \tag{B.1}$$

which is small in comparison to one, since the linear stability analysis showed that under relevant MBE conditions $\lambda_c \gg \ell$.

The linear stability analysis also provides us with information on the typical length and time scales. They behave like

$$x \sim \epsilon^{-1/2}, \quad t \sim \epsilon^{-2} \tag{B.2}$$

with the deposition flux. Following Ref. [45], we adopt the following scaling for the meander ζ and the reduced concentration field $u \equiv (c - c_{\mathrm{eq}}^0)\,\Omega$:

$$\zeta \sim \epsilon^{-1/2}, \quad u \sim \epsilon^{1/2}. \tag{B.3}$$

We now perform a coordinate transformation,

$$X = \epsilon^{1/2}\, x/\ell, \tag{B.4}$$

$$Y = (y - V_0 t - \zeta)/\ell, \tag{B.5}$$

$$T = \epsilon^2\, D/\ell^2 \cdot t, \tag{B.6}$$

such that the new variables X, Y, and T remain of order 1. Furthermore, we introduce

$$H(X,T) = \epsilon^{1/2}\, \zeta(x,t), \tag{B.7}$$

$$U(X,Y,T) = \epsilon^{-1/2}\, u(x,y,t) \tag{B.8}$$

to take the known scaling of the meander and of the concentration field into account.

In new coordinates the diffusion equation becomes

$$\rho^2\,\partial_{YY}U + \epsilon^{1/2}\,[\eta - \partial_{XX}H\,\partial_Y U - 2\,\partial_X H\,\partial_{XY}U] + \epsilon\,\partial_{XX}U = 0, \tag{B.9}$$

where we have introduced

$$\eta = \frac{\Omega F \ell^2}{\epsilon\, D}, \quad \rho = \sqrt{1 + (\partial_X H)^2}. \tag{B.10}$$

The boundary conditions read

$$\tilde{d}_+ \left[\rho^2\,\partial_Y U - \epsilon^{1/2}\,\partial_X H\,\partial_X U\right]\Big|_{Y=0} = \rho\,[U + \bar{\gamma}K]|_{Y=0}\,, \tag{B.11}$$

$$-\tilde{d}_- \left[\rho^2\,\partial_Y U - \epsilon^{1/2}\,\partial_X H\,\partial_X U\right]\Big|_{Y=1} = \rho\,[U + \bar{\gamma}K]|_{Y=1} \tag{B.12}$$

with the dimensionless attachment lengths

$$\tilde{d}_\pm(\theta) = \frac{d_\pm(\theta)}{\ell}, \tag{B.13}$$

the dimensionless stiffness

$$\bar{\gamma}(\theta) = \frac{c^0_{\mathrm{eq}}\Omega}{\ell}\Gamma(\theta), \tag{B.14}$$

and the dimensionless (negative) curvature:

$$K = \frac{\partial_{XX}H}{\rho^3}. \tag{B.15}$$

Finally, we rewrite the mass balance at the steps in the form

$$\begin{aligned}\epsilon^{1/2}\,\eta + \epsilon\,\partial_T H = &\left(\rho^2\,\partial_Y U - \epsilon^{1/2}\,\partial_X H\,\partial_X U\right)\Big|_{Y=0} \\ &- \left(\rho^2\,\partial_Y U - \epsilon^{1/2}\,\partial_X H\,\partial_X U\right)\Big|_{Y=1} \\ &- \epsilon\,\partial_X\left[\bar{\beta}(\theta)\,\frac{1}{\rho}\partial_X\left\{\bar{\gamma}(\theta)\,K\right\}\right]\end{aligned} \tag{B.16}$$

with the dimensionless line diffusion coefficient

$$\bar{\beta}(\theta) = \frac{D_{\mathrm{L}}(\theta)\,a}{D_{\mathrm{S}}\,\ell}. \tag{B.17}$$

We now expand H and U in power series of $\epsilon^{1/2}$:

$$H = H^{(0)} + \epsilon^{1/2}\,H^{(1/2)} + \epsilon\,H^{(1)} + \ldots, \tag{B.18}$$

$$U = U^{(0)} + \epsilon^{1/2}\,U^{(1/2)} + \epsilon\,U^{(1)} + \ldots. \tag{B.19}$$

For consistency we also expand all anisotropic model parameters:

$$\bar{\gamma}(\theta) = \bar{\gamma}(\theta^{(0)}) + \epsilon^{1/2}\,\bar{\gamma}'(\theta^{(0)})\,\partial_X H^{(1)}/(\rho^{(0)})^2 + \dots, \tag{B.20}$$

$$\bar{\beta}(\theta) = \bar{\beta}(\theta^{(0)}) + \epsilon^{1/2}\,\bar{\beta}'(\theta^{(0)})\,\partial_X H^{(1)}/(\rho^{(0)})^2 + \dots, \tag{B.21}$$

$$\tilde{d}_\pm(\theta) = \tilde{d}_\pm(\theta^{(0)}) + \epsilon^{1/2}\,\tilde{d}'_\pm(\theta^{(0)})\,\partial_X H^{(1)}/(\rho^{(0)})^2 + \dots, \tag{B.22}$$

where $\theta = \arctan(\partial_X H)$, $\theta^{(0)} = \arctan(\partial_X H^{(0)})$, and the prime denotes differentiation with respect to the angle.

We are now able to solve the system of dynamical equations for successive orders of $\epsilon^{1/2}$.

B.2. Solution at order 0

At $O(1)$ the diffusion equation reads

$$\partial_{YY} U^{(0)} = 0. \tag{B.23}$$

It has the general solution

$$U^{(0)} = A^{(0)}\,Y + B^{(0)}. \tag{B.24}$$

The boundary conditions at this order require

$$A^{(0)} = 0, \quad B^{(0)} = -\bar{\gamma} K^{(0)}. \tag{B.25}$$

Mass conservation at the steps is automatically fulfilled, since no $O(1)$ terms remain in Eq. (B.16).

B.3. Solution at order 1/2

At $O(\epsilon^{1/2})$ the diffusion equation becomes

$$\partial_{YY} U^{(1/2)} = -\frac{\eta}{(\rho^{(0)})^2}. \tag{B.26}$$

The general solution can be written as

$$U^{(1/2)} = -\frac{\eta}{2(\rho^{(0)})^2}\,Y^2 + A^{(1/2)}\,Y + B^{(1/2)}, \tag{B.27}$$

and the integration constants are determined by the boundary conditions at this order:

$$
\begin{aligned}
A^{(1/2)} &= \frac{\eta + 2\rho^{(0)}\left[\tilde{d}_-\eta - (\tilde{d}_+ + \tilde{d}_-)\,\partial_X(\bar{\gamma}K^{(0)})\,\partial_X H^{(0)}\right]}{2(\rho^{(0)})^2\left[(\tilde{d}_+ + \tilde{d}_-)\,\rho^{(0)} + 1\right]}, && \text{(B.28)}\\
B^{(1/2)} &= \frac{1}{2\rho^{(0)}\left[(\tilde{d}_+ + \tilde{d}_-)\,\rho^{(0)} + 1\right]}\times\\
&\quad \Big[\eta\,\tilde{d}_+ + 2\tilde{d}_+\,\partial_X H^{(0)}\,\partial_X(\bar{\gamma}K^{(0)})\\
&\quad + 2\,(\tilde{d}_+\tilde{d}_-\,\eta - \bar{\gamma}K^{(1)})\,\rho^{(0)} - 2\,(\tilde{d}_+ + \tilde{d}_-)\,\bar{\gamma}K^{(1)}\,(\rho^{(0)})^2\Big]. && \text{(B.29)}
\end{aligned}
$$

Once again, mass conservation at the steps is automatically fulfilled. At this order, the total flux at the steps does not depend on X and is compatible with the average step velocity V_0.

B.4. Solution at order 1

At $O(\epsilon)$ the diffusion equation reads

$$
\begin{aligned}
\partial_{YY}U^{(1)} = \frac{1}{(\rho^{(0)})^2}\Big[&\partial_{XX}H^{(0)}\,\partial_Y U^{(1/2)} + 2\,\partial_X H^{(0)}\,\partial_{XY}U^{(1/2)}\\
&- (\rho^{(1/2)})^2\,\partial_{YY}U^{(1/2)} - \partial_{XX}U^{(0)}\Big]. \qquad \text{(B.30)}
\end{aligned}
$$

Its solution takes the form

$$
U^{(1)} = C_3^{(1)}\,Y^3 + C_2^{(1)}\,Y^2 + A^{(1)}\,Y + B^{(1)}, \qquad \text{(B.31)}
$$

where $C_3^{(1)}$ and $C_2^{(1)}$ are determined by the diffusion equation and $A^{(1)}$ and $B^{(1)}$ by the boundary conditions.

At this order the mass balance at the steps gives a solvability condition in the form of a closed partial differential equation for H_0:

$$
\begin{aligned}
\partial_T H^{(0)} = -\partial_X\Bigg[&\frac{\eta}{2}\,\frac{\tilde{d}_- - \tilde{d}_+}{[(\tilde{d}_+ + \tilde{d}_-)\,\rho^{(0)} + 1]\,\rho^{(0)}}\,\partial_X H^{(0)}\\
&+ \left(\bar{\beta} + \frac{\tilde{d}_+ + \tilde{d}_- + \rho^{(0)}}{(\tilde{d}_+ + \tilde{d}_-)\,\rho^{(0)} + 1}\right)\frac{\partial_X\left(\bar{\gamma}K^{(0)}\right)}{\rho^{(0)}}\Bigg]. \qquad \text{(B.32)}
\end{aligned}
$$

This equation does not differ from the evolution equation which was derived for the isotropic model [20]. At this point, anisotropy is introduced by simply evaluating $\bar{\gamma}$, $\bar{\beta}$, and $\tilde{d}_\pm$ at the orientation $\theta^{(0)} \equiv \arctan(\partial_X H^{(0)})$.

Expressing the evolution equation in physical units, we obtain

$$\begin{aligned}\partial_t\zeta = -\partial_x\biggl[&\frac{\Omega F\ell^2}{2}\left(\frac{d_- - d_+}{d_+ + d_- + \ell_\perp}\right)\frac{\partial_x\zeta}{1+(\partial_x\zeta)^2}\\ &- \left(D_{\mathrm{L}}a + D_{\mathrm{S}}\,\frac{(d_+ + d_-)\,\ell_\perp + \ell^2}{d_+ + d_- + \ell_\perp}\right)\frac{\partial_x(\Gamma\kappa)}{[1+(\partial_x\zeta)^2]^{1/2}}\biggr],\end{aligned} \tag{B.33}$$

where we have introduced the effective interstep distance $\ell_\perp = \ell/[1+(\partial_x\zeta)^2]^{1/2}$.

B.5. Solution at order 3/2

At $O(\epsilon^{3/2})$ the diffusion equation reads:

$$\begin{aligned}\partial_{YY}U^{(3/2)} = \frac{1}{(\rho^{(0)})^2}\Bigl[&\partial_{XX}H^{(1/2)}\,\partial_Y U^{(1/2)} + \partial_{XX}H^{(0)}\,\partial_Y U^{(1)}\\ &+ 2\,\partial_X H^{(1/2)}\,\partial_{XY}U^{(1/2)} + 2\,\partial_X H^{(0)}\,\partial_{XY}U^{(1)}\\ &- (\rho^{(1)})^2\,\partial_{YY}U^{(1/2)} - (\rho^{(1/2)})^2\,\partial_{YY}U^{(1)} - \partial_{XX}U^{(1/2)}\Bigr].\end{aligned} \tag{B.34}$$

Its solution takes the form

$$U^{(3/2)} = C_4^{(3/2)}\,Y^4 + C_3^{(3/2)}\,Y^3 + C_2^{(3/2)}\,Y^2 + A^{(3/2)}\,Y + B^{(3/2)}, \tag{B.35}$$

where $C_4^{(3/2)}$, $C_3^{(3/2)}$, and $C_2^{(3/2)}$ are determined by the diffusion equation and $A^{(3/2)}$ and $B^{(3/2)}$ by the boundary conditions at this order.

For simplicity, we now restrict ourselves to the one-sided model where $d_+ = 0$ and $d_- \to \infty$. Then, at this order, mass conservation at the steps provides the following differential equation for $H^{(1/2)}$:

$$\begin{aligned}\partial_T H^{(1/2)} = -\partial_X\biggl[&\frac{\eta}{2}\frac{\partial_X H^{(1/2)}}{(\rho^{(0)})^2} + \frac{\eta}{(\rho^{(0)})^2}\left(\frac{1}{(\rho^{(0)})^2} - 1\right)\partial_X H^{(1/2)}\\ &+ \frac{\partial_X(\bar\gamma K)^{(1/2)}}{(\rho^{(0)})^2} - \frac{2}{(\rho^{(0)})^4}\,\partial_X H^{(0)}\,\partial_X H^{(1/2)}\,\partial_X\left(\bar\gamma K^{(0)}\right)\\ &+ \frac{\bar\beta}{\rho^{(0)}}\,\partial_X\,(\bar\gamma K)^{(1/2)} + \left(\frac{\bar\beta'\,\partial_X H^{(1/2)}}{(\rho^{(0)})^3} - \frac{\bar\beta\,\rho^{(1/2)}}{(\rho^{(0)})^2}\right)\partial_X\left(\bar\gamma K^{(0)}\right)\\ &+ \frac{1}{2(\rho^{(0)})^4}\,\partial_{XX}H^{(0)}\,\partial_X\left(\bar\gamma K^{(0)}\right)\\ &+ \frac{\eta}{3(\rho^{(0)})^6}\,\partial_X H^{(0)}\,\partial_{XX}H^{(0)} + \frac{\eta}{6(\rho^{(0)})^4}\,\partial_X H^{(0)}\,\partial_{XX}H^{(0)}\biggr].\end{aligned} \tag{B.36}$$

Here we have used the abbreviation

$$(\bar\gamma K)^{(1/2)} = \bar\gamma K^{(1/2)} + \bar\gamma'\,\frac{\partial_X H^{(1/2)}}{(\rho^{(0)})^2}\,K^{(0)} \tag{B.37}$$

for the $O(\epsilon^{1/2})$ coefficient in the ϵ expansion of $\bar{\gamma}K$.

By introducing

$$\tilde{H} = H^{(0)} + \epsilon^{1/2}\, H^{(1/2)}, \tag{B.38}$$

$$\tilde{K} = K^{(0)} + \epsilon^{1/2}\, K^{(1/2)}, \tag{B.39}$$

$$\tilde{\rho} = \rho^{(0)} + \epsilon^{1/2}\, \rho^{(1/2)}, \tag{B.40}$$

we can rewrite the equations for $H^{(0)}$ and $H^{(1/2)}$ as a single equation for $\tilde{H}$:

$$\begin{aligned} \partial_T \tilde{H} = -\partial_X \Bigg\{ & \frac{\eta}{2} \frac{\partial_X \tilde{H}}{\tilde{\rho}^2} \left[1 + \epsilon^{1/2} \frac{\partial_{XX} \tilde{H}}{3\tilde{\rho}^3} \left(\tilde{\rho} + \frac{2}{\tilde{\rho}} \right) \right] \\ & + \left[\frac{1}{\tilde{\rho}^2} + \frac{\tilde{\beta}}{\tilde{\rho}} + \epsilon^{1/2} \frac{\partial_{XX} \tilde{H}}{2\tilde{\rho}^4} \right] \partial_X (\widetilde{\gamma K}) \Bigg\}. \end{aligned} \tag{B.41}$$

Here $\tilde{\beta}$ and $(\widetilde{\gamma K})$ denote expansions of $\bar{\beta}$ and $\bar{\gamma}K$ that are truncated at $O(\epsilon^{1/2})$.

In physical units the evolution equation (B.41) becomes:

$$\begin{aligned} \partial_t \zeta = -\partial_x \Bigg\{ & \frac{\Omega F \ell^2}{2} \frac{\partial_x \zeta}{1 + (\partial_x \zeta)^2} \left[1 - \frac{\kappa \ell}{3} \frac{3 + (\partial_x \zeta)^2}{[1 + (\partial_x \zeta)^2]^{1/2}} \right] \\ & - \left[\left(\frac{D_\mathrm{S} \ell}{[1 + (\partial_x \zeta)^2]^{1/2}} + D_\mathrm{L}(\theta)\, a \right) - \frac{D_\mathrm{S} \ell^2 \kappa}{2} \right] \frac{\partial_x [\Gamma(\theta)\, \kappa]}{[1 + (\partial_x \zeta)^2]^{1/2}} \Bigg\}. \end{aligned} \tag{B.42}$$

This equation is equivalent to the one obtained for the isotropic model [20], that is to say, there are no additional terms due to Γ and D_L anisotropy at this order.

C. Drift velocity

In this appendix we derive a scaling law for the drift velocity of steady-state solutions that travel in the x direction.

If one takes the first subdominant contribution into account, the evolution equation for the step meander $\zeta(x,t)$ becomes

$$\begin{aligned}\partial_t \zeta = -\partial_x \Bigg\{ & \frac{\Omega F \ell^2}{2} \, \frac{\partial_x \zeta}{1+(\partial_x\zeta)^2} \left[1 - \frac{\kappa \ell}{3} \frac{3+(\partial_x\zeta)^2}{[1+(\partial_x\zeta)^2]^{1/2}} \right] \\ & - \left[\left(\frac{D_\mathrm{S} \ell}{[1+(\partial_x\zeta)^2]^{1/2}} + D_\mathrm{L}(\theta)\, a \right) - \frac{D_\mathrm{S} \ell^2 \kappa}{2} \right] \frac{\partial_x [\Gamma(\theta)\, \kappa]}{[1+(\partial_x\zeta)^2]^{1/2}} \Bigg\}. \end{aligned} \tag{C.1}$$

In our context it is useful to have the dimensionless equation as well (see App. B), which makes the ϵ dependence explicit:

$$\begin{aligned}\partial_T \tilde{H} = -\partial_X \Bigg\{ & \frac{\eta}{2} \frac{\partial_X \tilde{H}}{\tilde{\rho}^2} \left[1 + \epsilon^{1/2} \, \frac{\partial_{XX} \tilde{H}}{3\tilde{\rho}^3} \left(\tilde{\rho} + \frac{2}{\tilde{\rho}} \right) \right] \\ & + \left[\frac{1}{\tilde{\rho}^2} + \frac{\tilde{\beta}}{\tilde{\rho}} + \epsilon^{1/2} \, \frac{\partial_{XX} \tilde{H}}{2\tilde{\rho}^4} \right] \partial_X (\widetilde{\gamma K}) \Bigg\}. \end{aligned} \tag{C.2}$$

These equations have solutions that drift sideways at a constant velocity v_d. In order to find them we consider the function $h(x) = \zeta(x - v_\mathrm{d} t, t)$, which is a steady-state solution in the co-moving frame. This function $h(x)$ satisfies the equation

$$\partial_t h = \partial_x \left[A + B\, \partial_x \left(\frac{\delta \mathcal{F}}{\delta h} \right) \right] + v_\mathrm{d}\, \partial_x h = 0, \tag{C.3}$$

where A and B are abbreviations for complicated functions in Eqs. (C.1, C.2), which depend on $\partial_x h$ and higher derivatives. $\mathcal{F}$ is the step free energy; the variational derivative of $\mathcal{F}$ with respect to h gives rise to the Gibbs-Thomson correction term.

Integrating Eq. (C.3) with respect to x, we obtain:

$$A + B\, \partial_x \left(\frac{\delta \mathcal{F}}{\delta h} \right) = -J - v_\mathrm{d}\, h, \tag{C.4}$$

where J is an integration constant that describes a constant current along the step.

Our task is now to find J and v_d as a function of the steady-state solution $h(x)$. To this end we first point out that

$$\int_{x_0}^{x_1} \mathrm{d}x\, \partial_x \left(\frac{\delta \mathcal{F}}{\delta h} \right) = 0, \tag{C.5}$$

$$\int_{x_0}^{x_1} \mathrm{d}x\, h(x)\, \partial_x \left(\frac{\delta \mathcal{F}}{\delta h} \right) = 0, \tag{C.6}$$

where $x_1 - x_0 \equiv \lambda_0$ is the wavelength of the steady-state solution. The first integral (C.5) vanishes because $\delta\mathcal{F}/\delta h$ is a periodic function. The second integral (C.6) vanishes because it can be written (after repeated integration by parts) as an integral over the derivative of a periodic function.

Integrating over one period both (C.4) and the equation that is obtained by multiplying (C.4) with $h(x)$, we obtain the following linear system for J and v_d:

$$J \int_{x_0}^{x_1} \frac{\mathrm{d}x}{B} + v_\mathrm{d} \int_{x_0}^{x_1} \mathrm{d}x\, \frac{h}{B} = -\int_{x_0}^{x_1} \mathrm{d}x\, \frac{A}{B}, \tag{C.7}$$

$$J \int_{x_0}^{x_1} \mathrm{d}x\, \frac{h}{B} + v_\mathrm{d} \int_{x_0}^{x_1} \mathrm{d}x\, \frac{h^2}{B} = -\int_{x_0}^{x_1} \mathrm{d}x\, \frac{A\, h}{B}. \tag{C.8}$$

Eq. (C.2) shows that A and B can be decomposed in the following way:

$$A = A_0 + \epsilon^{1/2}\, A_1, \tag{C.9}$$

$$B = B_0 + \epsilon^{1/2}\, B_1. \tag{C.10}$$

The same holds for $h(x) = h_0(x) + \epsilon^{1/2}\, h_1(x)$, which was just the definition of $\tilde{H}$ in App. B.

If we now expand the linear system (C.7, C.8) with respect to ϵ, we find that there is no contribution to the drift velocity at zeroth order. To leading order the drift velocity v_d is thus written as:

$$v_\mathrm{d} = \epsilon^{1/2}\, f(A_0, A_1, B_0, B_1, h_0, h_1). \tag{C.11}$$

Going back to physical units, we find:

$$v_\mathrm{d} = \frac{\Omega^2 F^2 \ell^5}{\Gamma(0)\, [D_\mathrm{S}\ell + D_\mathrm{L}(0)\, a]}\, g(\tilde{\beta}, A_\Gamma, A_\mathrm{L}, \lambda_0). \tag{C.12}$$

The functions f and g are not easy to obtain. In particular, they depend on the precise form of the anisotropies and on the wavelength λ_0 of the steady-state solution. This dependence can be found in numerical simulations, as shown in Fig. 4.8. In the same figure we present numerical results that confirm the relation $v_\mathrm{d} \sim \epsilon^{1/2}$.

D. Geometrical mapping

Here we give a detailed description of the geometrical mapping that we have used to reduce terrace diffusion anisotropy to anisotropic step properties. The first section is mathematical and deals with geometrical aspects of the transformation, the second section explains the application to the BCF model.

D.1. Coordinate transformation

Transformation equations

We consider the affine transformation

$$\bar{x} = x - \frac{d_{12}}{d_{22}} y, \tag{D.1}$$

$$\bar{y} = \frac{1}{d_{22}} y \tag{D.2}$$

with its inverse

$$x = \bar{x} + d_{12}\,\bar{y}, \tag{D.3}$$

$$y = d_{22}\,\bar{y}. \tag{D.4}$$

This transformation maps the curve $\mathbf{r} = x\,\mathbf{e}_x + y\,\mathbf{e}_y$ to the curve $\bar{\mathbf{r}} = \bar{x}\,\bar{\mathbf{e}}_{\bar{x}} + \bar{y}\,\bar{\mathbf{e}}_{\bar{y}}$. Using matrix notation, we can also write $\bar{\mathbf{r}} = A\mathbf{r}$.

Along with the coordinate transformation we perform a change of the metrics by requiring that $\bar{\mathbf{e}}_i \cdot \bar{\mathbf{e}}_j = \delta_{ij}$. Without changing the metrics, $\bar{\mathbf{e}}_{\bar{x}} \cdot \bar{\mathbf{e}}_{\bar{y}} = d_{12}$. In order to make this difference clear we shall now write $(\cdot,\cdot)$ for the scalar product if it is evaluated in the Cartesian metrics and $(\cdot,\cdot)'$ if the scalar product is evaluated in the redefined metrics.

Angles

We define the angle of a line element $\mathrm{d}\mathbf{r} = (\mathrm{d}x, \mathrm{d}y)$ or $\mathrm{d}\bar{\mathrm{r}} = (\mathrm{d}\bar{x}, \mathrm{d}\bar{y})$ with respect to the x or $\bar{x}$ axis via

$$\tan\theta = \frac{\mathrm{d}y}{\mathrm{d}x}, \quad \tan\bar{\theta} = \frac{\mathrm{d}\bar{y}}{\mathrm{d}\bar{x}}. \tag{D.5}$$

Using these equations and the coordinate transformation (D.1, D.2), we find the relationship between the angles θ and $\bar{\theta}$:

$$\tan\bar{\theta} = \frac{1}{d_{22}} \frac{\mathrm{d}y}{\mathrm{d}x - d_{12}/d_{22}\,\mathrm{d}y} = \frac{\tan\theta}{d_{22} - d_{12}\tan\theta}. \tag{D.6}$$

Arc length

For an element of the arc length we have the simple relation $\mathrm{d}s = \sqrt{\mathrm{d}x^2 + \mathrm{d}y^2}$. Due to the redefinition of the metrics, the analogous relation holds in the transformed system: $\mathrm{d}\bar{s} = \sqrt{\mathrm{d}\bar{x}^2 + \mathrm{d}\bar{y}^2}$.

The arc lengths s and $\bar{s}$ are related via $\alpha = \mathrm{d}s/\mathrm{d}\bar{s}$, which can be expressed in terms of θ,

$$\begin{aligned}\frac{1}{\alpha} = \frac{\mathrm{d}\bar{s}}{\mathrm{d}s} &= \frac{\sqrt{\mathrm{d}\bar{x}^2 + \mathrm{d}\bar{y}^2}}{\sqrt{\mathrm{d}x^2 + \mathrm{d}y^2}} && \text{(D.7)}\\ &= \frac{1}{d_{22}}\sqrt{(d_{22}\,\cos\theta - d_{12}\,\sin\theta)^2 + \sin^2\theta}, && \text{(D.8)}\end{aligned}$$

or in terms of $\bar{\theta}$,

$$\begin{aligned}\alpha = \frac{\mathrm{d}s}{\mathrm{d}\bar{s}} &= \frac{\sqrt{\mathrm{d}x^2 + \mathrm{d}y^2}}{\sqrt{\mathrm{d}\bar{x}^2 + \mathrm{d}\bar{y}^2}} && \text{(D.9)}\\ &= \sqrt{(\cos\bar{\theta} + d_{12}\,\sin\bar{\theta})^2 + d_{22}^2\,\sin^2\bar{\theta}}. && \text{(D.10)}\end{aligned}$$

Normals and tangents

The Cartesian tangent is $\mathbf{t} = t_x\,\mathbf{e}_x + t_y\,\mathbf{e}_y$. Using the transformation equations (D.1, D.2), we obtain the unit tangent in the transformed system:

$$\begin{aligned}t_{\bar{x}} &= \alpha\left(t_x - \frac{d_{12}}{d_{22}}\,t_y\right), && \text{(D.11)}\\ t_{\bar{y}} &= \frac{\alpha}{d_{22}}t_y. && \text{(D.12)}\end{aligned}$$

The prefactor $\alpha \equiv \mathrm{d}s/\mathrm{d}\bar{s}$ stems from the normalization of the tangent vector.

From the redefined metrics we find the following normal:

$$\begin{aligned}n_{\bar{x}} &= -\frac{\alpha}{d_{22}}t_y = \frac{\alpha}{d_{22}}n_x && \text{(D.13)}\\ n_{\bar{y}} &= \alpha\left(t_x - \frac{d_{12}}{d_{22}}\,t_y\right) = \alpha\left(\frac{d_{12}}{d_{22}}n_x + n_y\right). && \text{(D.14)}\end{aligned}$$

Curvature

In both coordinate systems we can find the curvature from the derivative of the unit tangent with respect to the arc length:

$$\frac{\mathrm{d}\mathbf{t}}{\mathrm{d}s} = \kappa\,\mathbf{n}, \quad \frac{\mathrm{d}\bar{\mathbf{t}}}{\mathrm{d}\bar{s}} = \bar{\kappa}\,\bar{\mathbf{n}}. \tag{D.15}$$

We now insert the transformation of the tangent into the second equation and apply the chain rule for differentiation with respect to the arc length:

$$\bar{\kappa}\,\bar{\mathbf{n}} = \frac{\mathrm{d}\bar{\mathbf{t}}}{\mathrm{d}\bar{s}} = \frac{\mathrm{d}s}{\mathrm{d}\bar{s}}\frac{\mathrm{d}}{\mathrm{d}s}(\alpha A\mathbf{t}) = \alpha A\mathbf{t}\frac{\mathrm{d}\alpha}{\mathrm{d}s} + \alpha^2 A\frac{\mathrm{d}\mathbf{t}}{\mathrm{d}s}. \tag{D.16}$$

With $\bar{\mathbf{t}} = \alpha A\mathbf{t}$ and $\mathrm{d}\mathbf{t}/\mathrm{d}s = \kappa\,\mathbf{n}$, this result can also be written as

$$\bar{\kappa}\,\bar{\mathbf{n}} = \bar{\mathbf{t}}\,\frac{\mathrm{d}\alpha}{\mathrm{d}s} + \alpha^2\kappa\,A\mathbf{n}. \tag{D.17}$$

If we now multiply this equation with $\bar{\mathbf{n}}$, we obtain the formula that gives the transformed curvature as a function of the Cartesian curvature:

$$\bar{\kappa} = \alpha^2(\bar{\mathbf{n}}, A\mathbf{n})\,\kappa = \frac{\alpha^3}{d_{22}}\kappa. \tag{D.18}$$

Partial derivatives

In the following we often need the transformation of the partial derivatives:

$$\partial_x = \partial_{\bar{x}}, \tag{D.19}$$

$$\partial_y = \frac{1}{d_{22}}\partial_{\bar{y}} - \frac{d_{12}}{d_{22}}\,\partial_{\bar{x}}, \tag{D.20}$$

$$\partial_x^2 = \partial_{\bar{x}}^2, \tag{D.21}$$

$$\partial_y^2 = \frac{1}{d_{22}^2}\partial_{\bar{y}}^2 - \frac{2d_{12}}{d_{22}^2}\partial_{\bar{x}\bar{y}} + \frac{d_{12}^2}{d_{22}^2}\partial_{\bar{x}}^2, \tag{D.22}$$

$$\partial_{xy} = \frac{1}{d_{22}}\partial_{\bar{x}\bar{y}} - \frac{d_{12}}{d_{22}}\,\partial_{\bar{x}}^2. \tag{D.23}$$

D.2. Application to the BCF model

On an anisotropic terrace, the diffusion equation takes the form

$$\nabla\cdot\underline{\underline{D}}\nabla c + F = 0, \tag{D.24}$$

where

$$\underline{\underline{D}} = \begin{pmatrix} D_{11} & D_{12} \\ D_{12} & D_{22} \end{pmatrix} = D_0\begin{pmatrix} d_{11} & d_{12} \\ d_{12} & d_{22} \end{pmatrix} \tag{D.25}$$

is the symmetric diffusion tensor. D_0 is given by $D_0 = [D_{11}D_{22} - D_{12}^2]^{1/2}$ and d_{11}, d_{22}, d_{12} are consistent with the parameters in the transformation (D.1, D.2).

Evaluating Eq. (D.24), we first obtain

$$D_0\,[d_{11}\,\partial_{xx}c + d_{22}\,\partial_{yy}c + 2d_{12}\,\partial_{xy}c] + F = 0, \tag{D.26}$$

and after expressing the partial derivatives in terms of $\bar{x}$ and $\bar{y}$, we arrive at

$$D_0\left[\frac{1}{d_{22}}\partial_{\bar{x}\bar{x}}c + \frac{1}{d_{22}}\partial_{\bar{y}\bar{y}}c\right] + F = 0. \tag{D.27}$$

In the new coordinate system, terrace diffusion is isotropic. We now set $\bar{D}_0 = D_0/d_{22}$ and write this equation in a more compact form:

$$\bar{D}_0\bar{\nabla}^2 c + F = 0. \tag{D.28}$$

We have chosen the transformation such that the adatom concentration is unchanged in the new system. Due to $c_{\mathrm{eq}} = c_{\mathrm{eq}}^0(1+\Gamma\kappa)$ and the given transformation (D.18) of the curvature κ, the modified step stiffness reads

$$\bar{\Gamma}(\bar{\theta}) = \frac{\kappa}{\bar{\kappa}}\Gamma = \frac{d_{22}}{\alpha^3}\Gamma. \tag{D.29}$$

The boundary conditions at both sides of the step are given by

$$\pm\,(\mathbf{n}, \underline{\underline{D}}\nabla c)|_\pm = \nu_\pm(c - c_{\mathrm{eq}})|_\pm. \tag{D.30}$$

Evaluating the left-hand side of this equation, we first obtain

$$(\mathbf{n}, \underline{\underline{D}}\nabla c) = n_x\,(D_{11}\,\partial_x c + D_{12}\,\partial_y c) + n_y\,(D_{22}\,\partial_y c + D_{12}\,\partial_x c). \tag{D.31}$$

Replacing the partial derivatives according to Eqs. (D.19, D.20), we arrive at

$$(\mathbf{n}, \underline{\underline{D}}\nabla c) = D_0\left[\frac{n_x}{d_{22}}\partial_{\bar{x}}c + \left(\frac{d_{12}}{d_{22}}n_x + n_y\right)\partial_{\bar{y}}c\right]. \tag{D.32}$$

With (D.13, D.14), we can here identify the components of the transformed normal, so that we have the following identity:

$$(\mathbf{n}, \underline{\underline{D}}\nabla c) = \frac{D_0}{\alpha}\left[n_{\bar{x}}\,\partial_{\bar{x}}c + n_{\bar{y}}\,\partial_{\bar{y}}c\right], \tag{D.33}$$

or with the definition of the scalar product in the transformed system:

$$(\mathbf{n}, \underline{\underline{D}}\nabla c) = \frac{D_0}{\alpha}(\bar{\mathbf{n}}, \bar{\nabla}c)'. \tag{D.34}$$

Plugging this relation into (D.30), we finally obtain the correct boundary conditions in the transformed system:

$$\pm\,\bar{D}_0\,(\bar{\mathbf{n}},\bar{\nabla}c)'|_\pm = \bar{\nu}_\pm(c-c_{\mathrm{eq}})|_\pm \tag{D.35}$$

with the modified kinetic coefficients

$$\bar{\nu}_\pm(\bar{\theta}) = \frac{\alpha}{d_{22}}\nu_\pm. \tag{D.36}$$

In order to complete the mathematical description of the moving-boundary problem we need to find the transformation of the step velocity. The Cartesian normal velocity is given by

$$v_n = \Omega\left(\mathbf{n},\underline{\underline{D}}\nabla c|_+ - \underline{\underline{D}}\nabla c|_-\right) + a\,\partial_s\left[D_{\mathrm{L}}\,\partial_s(\Gamma\kappa)\right]. \tag{D.37}$$

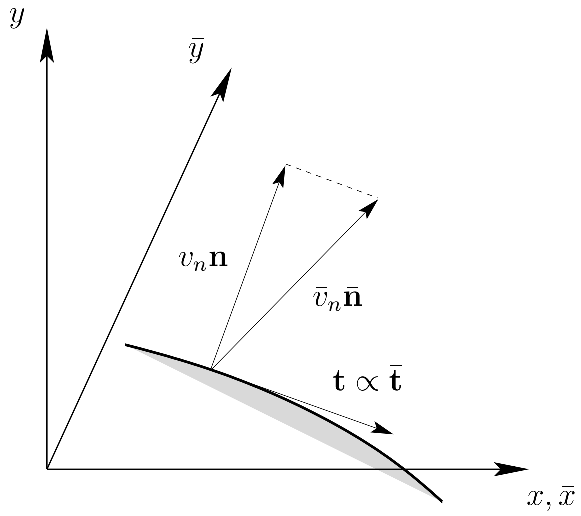

Figure D.1.: Transformation of the normal velocity. A part of the step curve (shaded region) and the axes of the coordinate systems are shown. Due to the redefinition of the metrics in the transformed system, the magnitudes of the tangents $\mathbf{t}$ and $\bar{\mathbf{t}}$ differ in general. The normals $\mathbf{n}$ and $\bar{\mathbf{n}}$ also differ in direction. The dashed line must be parallel to the step tangent, so that both velocities describe the same growth of a (planar) front. It now follows that $v_n = (\mathbf{n},\bar{\mathbf{n}})\,\bar{v}_n$, where the scalar product $(\mathbf{n},\bar{\mathbf{n}})$ is evaluated in the Cartesian metrics.

From the drawing in Fig. D.1 it can be concluded that the normal velocities in the two coordinate systems are related via

$$\bar{v}_n\,(\bar{\mathbf{n}},\mathbf{n}) = v_n, \tag{D.38}$$

where the scalar product $(\bar{\mathbf{n}}, \mathbf{n}) = d_{22}/\alpha$ is evaluated in the Cartesian metrics.

This result is consistent with

$$\bar{v}_n = v_n\, (\mathbf{n}, \bar{\mathbf{n}})', \tag{D.39}$$

where the scalar product $(\mathbf{n}, \bar{\mathbf{n}})' = \alpha/d_{22}$ is evaluated in the metrics of the transformed system.

Combining Eq. (D.37) with Eqs. (D.34,D.38), we find the transformed normal velocity

$$\bar{v}_n = \Omega\, \bar{D}_0\, (\bar{\mathbf{n}}, \bar{\nabla} c|_+ - \bar{\nabla} c|_-)' + a\, \partial_{\bar{s}}[\bar{D}_\mathrm{L}\, \partial_{\bar{s}}(\bar{\Gamma}\bar{\kappa})] \tag{D.40}$$

with the modified line diffusion coefficient

$$\bar{D}_\mathrm{L}(\bar{\theta}) = \frac{D_\mathrm{L}}{d_{22}\, \alpha}. \tag{D.41}$$

Zusammenfassung

Die Molekularstrahlepitaxie (MBE) ist ein verbreitetes Verfahren zur Herstellung von Nanostrukturen auf Kristalloberflächen. Hierbei wird eine Probe im Hochvakuum einem Atom- bzw. Molekülstrahl ausgesetzt, der durch Verdampfung des abzuscheidenden Materials in einer Effusionszelle erzeugt wird. Da das Wachstum des Kristalls vergleichsweise langsam erfolgt, hat man eine sehr gute Kontrolle über die Menge des abgeschiedenen Materials, die man bis auf den Bruchteil einer Monolage genau einstellen kann. Auf diese Weise lassen sich komplexe epitaktische Strukturen erzeugen.

MBE-Wachstum wird häufig an vizinalen Kristalloberflächen durchgeführt. Das sind Oberflächen, die man erhält, wenn man einen Kristall unter einem kleinen Winkel gegenüber einer seiner Netzebenen aufschneidet. Vizinale Oberflächen bestehen daher aus einer Folge etwa gleich großer Terrassen, die durch monoatomare Stufen voneinander getrennt sind.

Eine besondere Wachstumsform an vizinalen Oberflächen ist das Stufenwachstum (*step flow growth*). Durch geeignete Wahl der Wachstumsbedingungen wird erreicht, daß alle an der Oberfläche auftreffenden Atome durch Diffusion an die Stufen gelangen, wo sie sich in den Kristall einbauen. Das heißt, es findet keine Nukleation auf den Terrassen statt; der Kristall wächst geordnet Atomlage für Atomlage durch die Bewegung dieser Stufen.

Für viele Zwecke wäre es günstig, wenn die Oberfläche während des Wachstums ihre perfekte vizinale Geometrie behalten würde. In der Praxis beobachtet man jedoch oft ein Aufrauhen der Oberfläche, das mit der Depositionszeit zunimmt. Mittlerweile sind viele physikalische Mechanismen identifiziert, die zum Aufrauhen der Oberfläche beitragen. Eine herausragende Rolle dabei spielen deterministische Instabilitäten wie die Mäanderinstabilität.

Als Mäandern bezeichnet man die Exkursion der Stufen um ihre mittlere Lage, was zur Bildung von Rippeln in Richtung des Stufenzugs führt. Eine physikalische Ursache der Mäanderinstabilität ist der sogenannte Ehrlich-Schwoebel-Effekt. Dabei handelt es sich um eine Energiebarriere an den Stufen, die den Einbau eines Atoms in den Kristall erschwert, wenn sich das Atom der Stufe von der oberen Terrasse nähert.

Der Mäanderinstabilität wurden in der Vergangenheit eine Reihe von theoretischen Arbeiten gewidmet. Insbesondere wurde aus einer Kontinuumstheorie für das Stufenwachstum, dem Burton-Cabrera-Frank-Modell (BCF), eine Amplitudengleichung abgeleitet, mit deren Hilfe sich die zeitliche Entwicklung des Mäanders beschreiben läßt.

Der Einfluß von Kristallanisotropie auf die Dynamik der mäandernden Stufen wurde in diesem Rahmen bislang nicht untersucht. Das ist Gegenstand der vorliegenden Dissertation.

In den ersten Kapiteln dieser Arbeit wird das BCF-Modell eingeführt, die Stabilität der Stufen beim Wachstum in Hinblick auf das Mäandern untersucht und die Ableitung der Amplitudengleichung nachgezeichnet. Eine numerische Integration des vollen BCF-Modells wird mit den Aussagen der Amplitudengleichung verglichen, wobei sich eine sehr gute quantitative Übereinstimmung ergibt.

Der sich daran anschließende Hauptteil im Kapitel 4 ist der Untersuchung der Mäanderinstabilität unter Berücksichtigung von Anisotropie gewidmet. Aufgrund ihrer Fernordnung weisen Kristalle einen hohen Grad an Anisotropie auf. Alle Größen, die in die Kontinuumstheorie eingehen, sind mehr oder weniger anisotrop: die Linienspannung Γ der Stufen, der Liniendiffusionskoeffizient D_L, die kinetischen Koeffizienten ν_+ und ν_- sowie der Terrassendiffusionskoeffizient D. In drei Unterabschnitten werden nun die Folgen dieser Anisotropien untersucht.

Dabei zeigt sich zunächst im einseitigen Modell (unendlich starker Ehrlich-Schwoebel-Effekt), daß eine Anisotropie von Γ oder D_L ein neues Vergröberungsszenario zur Folge hat: die unterbrochene Vergröberung (*interrupted coarsening*). In Abhängigkeit von der Gestalt und Orientierung der Anisotropie kommt es zu einer Vergröberung der Rippelstruktur, die jedoch endet, sobald eine kritische Wellenlänge erreicht ist. Die experimentell beobachtete Wellenlänge ist also nicht allein durch die lineare Instabilität bestimmt und daher nicht mit der Wellenlänge der instabilsten Mode identisch. Dieser Effekt muß berücksichtigt werden, wenn man ein Modell für Stufenwachstum mit experimentellen Ergebnissen vergleichen möchte.

In der Arbeit wird gezeigt, daß diese Vergröberung im wesentlichen dann auftritt, wenn Γ oder D_L für die Orientierung der ungestörten Stufe (oder in einer gewissen Umgebung) ein Minimum annimmt. Darüber hinaus werden Formeln abgeleitet, die die Berechnung der zu erwartenden Wellenlänge erlauben. Dazu wird ein Zusammenhang zwischen der Vergröberungsdynamik und den möglichen Wellenlängen stationärer Lösungen der Amplitudengleichung hergestellt. In diesem Kontext gehen wir auch auf das Zusammenspiel von Kristallanisotropie und elastischer Stufenwechselwirkung ein. Es ist bekannt, daß elastische Wechselwirkungen zwischen den Stufen zu endloser Vergröberung führen. In der vorliegenden Arbeit wird gezeigt, daß eine vorhandene elastische Stufenwechselwirkung die asymptotische Entwicklung dominiert und damit das Vergröberungsverhalten bestimmt.

Der folgende Abschnitt ist dem zweiseitigen Modell gewidmet, mit dem die Auswirkungen einer Anisotropie des Ehrlich-Schwoebel-Effektes untersucht werden können. Hier ist zunächst hervorzuheben, daß sich die Anisotropie der kinetischen Koeffizienten bereits in der linearen Dispersionsrelation widerspiegelt. Für Anisotropien, die nicht die Rechts-links-Spiegelsymmetrie aufweisen, ergeben sich nach der linearen Theorie Lösungen, die driften. Des weiteren stellt sich zwischen den Mäandern benachbarter Stufen ein Phasenunterschied ein.

Die nichtlinearen Untersuchungen beschränken sich auf den Fall mit besagter Spiegelsymmetrie. Hier kann gezeigt werden, daß das Szenario der unterbrochenen Vergröberung auch als Folge einer Anisotropie des Ehrlich-Schwoebel-Effekts auftritt, und zwar dann, wenn der Ehrlich-Schwoebel-Effekt in Richtung der ungestörten Stufe maximal ist. Darüber hinaus gibt es ein weiteres Szenario in Fällen, wo der Ehrlich-Schwoebel-Effekt für bestimmte Stufenorientierungen das Vorzeichen wechselt. Dann findet eine endlose Vergröberung statt, allerdings auf einer sehr langsamen Zeitskala (logarithmische Vergröberung in Analogie zur Cahn-Hilliard-Dynamik).

Der letzte Abschnitt des Hauptteils beschäftigt sich mit den Folgen anisotroper Diffusion auf den Terrassen. Hierzu wird zunächst eine geometrische Abbildung vorgestellt, die es gestattet, das Problem mit anisotropen Terrassen auf ein Problem mit isotropen Terrassen zurückzuführen. Dabei bleibt die Struktur der Grundgleichungen erhalten. Die Anisotropie der Terrassendiffusion erscheint jetzt als Modifikation der Anisotropien der Stufeneigenschaften. Der wesentliche Vorteil dieses Ansatzes besteht darin, daß die zuvor benutzten Techniken auch in diesem Fall anwendbar sind. Mit Hilfe der geometrischen Abbildung ist es darüber hinaus möglich, anisotrope Terrassendiffusion in andere Modelle einzubauen, in denen bislang nur die Anisotropie der Stufeneigenschaften berücksichtigt wurde.

Auch Terrassenanisotropie kann zu unterbrochener Vergröberung führen. Dazu muß die Diffusion senkrecht zu den ungestörten Stufen langsamer sein als in Richtung dieser Stufen. Eine mögliche Besonderheit, die im Gegensatz zu Γ- und D_{L}-Anisotropie auftreten kann, sind Rippel, die gegenüber der Wachstumsrichtung geneigt sind. Das ist dann der Fall, wenn die Eigenrichtungen des Diffusionstensors nicht mit der Richtung des Stufenzuges bzw. mit der Richtung der ungestörten Stufen zusammenfallen.

Bibliography

[1] T. Ala-Nissila, R. Ferrando, and S. C. Ying, *Collective and single particle diffusion on surfaces*, Advances in Physics **51** (2002), 949–1078.

[2] M. Argentina, M. G. Clerc, R. Rojas, and E. Tirapegui, *Coarsening dynamics of the one-dimensional Cahn-Hilliard model*, Phys. Rev. E **71** (2005), no. 4, 046210.

[3] G. S. Bales and A. Zangwill, *Morphological instability of a terrace edge during step flow growth*, Phys. Rev. B **41** (1990), 5500.

[4] A.-L. Barabási and H. E. Stanley, *Fractal concepts in surface growth*, Cambridge Univ. Press, 1995.

[5] I. Bena, C. Misbah, and A. Valance, *Nonlinear evolution of a terrace edge during step-flow growth*, Phys. Rev. B **47** (1993), 7408–7419.

[6] I. N. Bronstein, K. A. Semendjajew, G. Musiol, and H. Mühling, *Taschenbuch der Mathematik*, Verlag Harri Deutsch, 1993.

[7] P. N. Brown, A. C. Hindmarsh, and L. R. Petzold, *Using Krylov methods in the solution of large-scale differential-algebraic systems*, SIAM J. Sci. Comp. (1994), 1467–1488.

[8] W. K. Burton, N. Cabrera, and F. C. Frank, *The growth of crystals and the equilibrium structure of their surfaces*, Phil. Trans. Roy. Soc. London **243** (1951), 299.

[9] D. J. Chadi, *Stabilities of single-layer and bilayer steps on Si(001) surfaces*, Phys. Rev. Lett. **59** (1987), 1691–1694.

[10] Scott D. Cohen and Alan C. Hindmarsh, *CVODE user guide*, Tech. Report UCRL-MA-118618, LLNL, September 1994.

[11] M. C. Cross and P. C. Hohenberg, *Pattern formation outside of equilibrium*, Rev. Mod. Phys. **65** (1993), 851–1112.

[12] Z. Csahók, C. Misbah, and A. Valance, *A class of nonlinear front evolution equations derived from geometry and conservation*, Physica D **128** (1999), 87.

[13] G. Danker, O. Pierre-Louis, K. Kassner, and C. Misbah, *Interrupted coarsening of anisotropic step meander*, Phys. Rev. E **68** (2003), 020601(R).

[14] ______, *Peculiar effects of anisotropic diffusion on dynamics of vicinal surfaces*, Phys. Rev. Lett. **93** (2004), 185504.

[15] S. Dieluweit, H. Ibach, M. Giesen, and T. L. Einstein, *Orientation dependence of the Cu(001) surface step stiffness: Failure of solid-on-solid and Ising models to describe experimental data*, Phys. Rev. B **67** (2003), 121410.

[16] C. Ebner, K.-B. Park, J.-F. Nielsen, and J. P. Pelz, *Simulations of denuded-zone formation during growth on surfaces with anisotropic diffusion*, Phys. Rev. B **68** (2003), 245404.

[17] M. Galassi et al., *GNU scientific library*, 1.5 ed., July 2004.

[18] M. Giesen, *Step and island dynamics at solid/vacuum and solid/liquid interfaces*, Prog. Surf. Sci. **68** (2001).

[19] F. Gillet, *Dynamique non linéaire de surfaces vicinales hors de l'équilibre*, Ph.D. thesis, Université Joseph Fourier, Grenoble, 2000.

[20] F. Gillet, O. Pierre-Louis, and C. Misbah, *Non-linear evolution of step meander during growth of a vicinal surface with no desorption*, Eur. Phys. J. B **18** (2000), 519–534.

[21] Gilad Goren, Itamar Procaccia, Steffen Rasenat, and Victor Steinberg, *Interactions and dynamics of topological defects: Theory and experiments near the onset of weak turbulence*, Phys. Rev. Lett. **63** (1989), 1237–1240.

[22] M. A. Herman, W. Richter, and H. Sitter, *Epitaxy: physical principles and technical implementation*, Springer-Verlag, Berlin, 2004.

[23] H. Hibino, Y. Homma, M. Uwaha, and T. Ogino, *Step wandering induced by homoepitaxy on Si(111) during "1×1"–7×7 phase transition*, Surf. Sci. Lett. **527** (2003), L222–L228.

[24] A. J. Hoeven, J. M. Lenssinck, D. Dijkkamp, E. J. van Loenen, and J. Dieleman, *Scanning-tunneling-microscopy study of single-domain Si(001) surfaces grown by molecular-beam epitaxy*, Phys. Rev. Lett. **63** (1989), 1830–1832.

[25] T. Ihle, C. Misbah, and O. Pierre-Louis, *Equilibrium step dynamics on vicinal surfaces revisited*, Phys. Rev. B **58** (1998), 2289–2309.

[26] J. Kallunki and J. Krug, *Breakdown of step flow growth in unstable homoepitaxy*, Europhys. Lett. **66** (2004), 749–755.

[27] Jouni Kallunki, *Growth instabilities of vicinal crystal surfaces during molecular beam epitaxy*, Ph.D. thesis, Universität Duisburg-Essen, 2003.

[28] Jouni Kallunki and Joachim Krug, *Asymptotic step profiles from a nonlinear growth equation for vicinal surfaces*, Phys. Rev. E **62** (2000), 6229.

[29] R. Kato, M. Uwaha, Y. Saito, and H. Hibino, *Step wandering due to the gap in diffusion coefficient on the upper and the lower terraces*, Surf. Sci. **522** (2003), 64–74.

[30] Toshihiro Kawakatsu and Toyonori Munakata, *Kink dynamics in a one-dimensional conserved TDGL system*, Prog. Theor. Phys. **74** (1985), no. 1, 11.

[31] Joachim Krug, *Introduction to step dynamics and step instabilities*, cond-mat/0405066 (2004).

[32] U. Kürpick and T. S. Rahman, *Diffusion processes relevant to homoepitaxial growth on Ag(100)*, Phys. Rev. B **57** (1998), 2482.

[33] A. Lindner, *Grundkurs Theoretische Physik*, 2nd ed., B. G. Teubner, Stuttgart, 1997.

[34] D.-J. Liu and J. W. Evans, *Sintering of 2d nanoclusters in metal(100) homoepitaxial systems: Comparison of atomistic and continuum modeling*, Phys. Rev. B **65** (2002).

[35] Y. W. Mo, J. Kleiner, M. B. Webb, and M. G. Lagally, *Activation energy for surface diffusion of Si on Si(001): A scanning-tunneling-microscopy study*, Phys. Rev. Lett. **66** (1991), no. 15, 1998.

[36] *NAG Fortran library routine document D03PHF/D03PHA*.

[37] A. Natori and R. W. Godby, *Surface diffusion on a stepped surface*, Phys. Rev. B **47** (1993), 15816.

[38] N. Néel, T. Maroutian, L. Douillard, and H.-J. Ernst, *From meandering to faceting, is step flow growth ever stable*, Phys. Rev. Lett. **91** (2003), no. 22, 226103.

[39] S. Paulin, F. Gillet, O. Pierre-Louis, and C. Misbah, *Unstable step meandering with elastic interactions*, Phys. Rev. Lett. **86** (2001), 5538–5541.

[40] O. Pierre-Louis, *Instabilité, dynamique non linéaire et fluctuations des surfaces vicinales hors de l'équilibre*, Ph.D. thesis, Université Joseph Fourier, Grenoble, 1997.

[41] ______, *Phase field models for step flow*, Phys. Rev. E **68** (2003), 021604.

[42] O. Pierre-Louis, G. Danker, J. Chang, K. Kassner, and C. Misbah, *Nonlinear dynamics of vicinal surfaces*, J. Crystal Growth **275** (2005), 56–64.

[43] O. Pierre-Louis and C. Misbah, *Out-of-equilibrium step meandering on a vicinal surface*, Phys. Rev. Lett. **76** (1996), 4761–4764.

[44] ______, *Dynamics and fluctuations during MBE on vicinal surfaces. I. Formalism and results of linear theory*, Phys. Rev. B **58** (1998).

[45] O. Pierre-Louis, C. Misbah, Y. Saito, J. Krug, and P. Politi, *New nonlinear evolution equation for steps during molecular beam epitaxy on vicinal surfaces*, Phys. Rev. Lett. **80** (1998), 4221–4224.

[46] A. Pimpinelli and J. Villain, *Physics of crystal growth*, Cambridge Univ. Press, 1998.

[47] M. Poensgen, J. F. Wolf, J. Frohn, M. Giesen, and H. Ibach, *Step dynamics on Ag (111) and Cu (100) surfaces*, Surf. Sci. **274** (1992), 430–440.

[48] P. Politi, G. Grenet, A. Marty, A. Ponchet, and J. Villain, *Instabilities in crystal growth by atomic or molecular beams*, Phys. Rep. **324** (2000), 271–405.

[49] P. Politi and C. Misbah, *When does coarsening occur in the dynamics of one-dimensional fronts*, Phys. Rev. Lett. **92** (2004), 090601.

[50] K. Radhakrishnan and A. C. Hindmarsh, *Description and use of LSODE, the Livermore solver for ordinary differential equations*, Tech. Report UCRL-ID-113855, LLNL, December 1993.

[51] C. Rottman and M. Wortis, *Exact equilibrium crystal shapes at nonzero temperature in two dimensions*, Phys. Rev. B **24** (1981), 6274–6277.

[52] M. Sato, M. Uwaha, Y. Saito, and Y. Hirose, *Repulsion-mediated step wandering on a Si(001) vicinal face*, Phys. Rev. B **67** (2003), 125408.

[53] W. Selke, *Dynamische Stufen auf Kristalloberflächen*, Physik Journal (2004).

[54] H. Stöcker (ed.), *Taschenbuch der Physik*, Verlag Harri Deutsch, 1994.

[55] R. Stumpf and M. Scheffler, *Ab initio calculations of energies and self-diffusion on flat and stepped surfaces of Al and their implications on crystal growth*, Phys. Rev. B **53** (1996), 4958–4973.

[56] Alessandro Torcini and Paolo Politi, *Coarsening process in one-dimensional surface growth models*, Eur. Phys. J. B **25** (2002), 519–529.

[57] Charles W. Tu, *Electronic materials growth: A retrospective and look forward*, J. Vac. Sci. Technol. A **21** (2003), S160.

[58] Bert Voigtländer, Thomas Weber, Pavel Ŝmilauer, and Dietrich E. Wolf, *Transition from island growth to step-flow growth for Si/Si(100) epitaxy*, Phys. Rev. Lett. **78** (1997), no. 11, 2164.

[59] Stephen J. Watson, Felix Otto, Boris Y. Rubinstein, and Stephen H. Davis, *Coarsening dynamics of the convective Cahn-Hilliard equation*, Physica D **178** (2003), 127–148.

[60] Wenguang Zhu, Francesco Buatier de Mongeot, U. Valbusa, E. G. Wang, and Zhenyu Zhang, *Adatom ascending at step edges and faceting on fcc metal (110) surfaces*, Phys. Rev. Lett. **92** (2004), no. 10, 106102.

Curriculum vitae

Name	Gerrit Danker
Geburtsdatum	23. Oktober 1975
Geburtsort	Magdeburg
Staatsangehörigkeit	deutsch
Familienstand	ledig

1982–1990	Heinrich-Germer-Oberschule, Magdeburg
1990–1994	Spezialschule mathematisch-naturwissenschaftlich-technischer Richtung, Magdeburg (seit 1993 Werner-von-Siemens-Gymnasium)
1994–1999	Studium der Physik an der Otto-von-Guericke-Universität Magdeburg
	Diplomarbeit über Oberflächenwellen auf magnetischen Flüssigkeiten
seit 2000	Wissenschaftlicher Mitarbeiter am Institut für Theoretische Physik der Otto-von-Guericke-Universität Magdeburg